



PONTIFICIA UNIVERSIDAD CATOLICA DE CHILE
SCHOOL OF ENGINEERING

QUANTIFICATION OF HEPATIC STEATOSIS USING MAGNETIC RESONANCE IMAGING

DANIEL FERNANDO AGUIRRE REYES

Thesis submitted to the Office of Graduate Studies
in partial fulfillment of the requirements for the degree of
Doctor in Engineering Sciences

Advisors:

PABLO IRARRÁZAVAL

MARCELO ANDÍA

Santiago de Chile, January 2016

© MMXVI, DANIEL FERNANDO AGUIRRE REYES



PONTIFICIA UNIVERSIDAD CATOLICA DE CHILE
SCHOOL OF ENGINEERING

QUANTIFICATION OF HEPATIC STEATOSIS USING MAGNETIC RESONANCE IMAGING

DANIEL FERNANDO AGUIRRE REYES

Members of the Committee:

PABLO IRARRÁZAVAL

MARCELO ANDÍA

JORGE VASQUEZ

CRISTIAN TEJOS

STÉREN CHABERT

MARCELO GUARINI

DIEGO HERNANDO

Thesis submitted to the Office of Graduate Studies
in partial fulfillment of the requirements for the degree of
Doctor in Engineering Sciences

Santiago de Chile, January 2016

© MMXVI, DANIEL FERNANDO AGUIRRE REYES

*Gratefully to my family: my parents
Patricio and María Augusta, my
brother Santiago, my sister María
Patricia, my beloved wife Carolina,
and mi daughter Amanda*

ACKNOWLEDGEMENTS

I would like to thank the following people:

To my beloved wife Carolina and mi little daughter Amanda, a very special thanks for all the support, the sacrifice to be far away from our city and country, the caring and the love given to me while we were achieving another objective in our lives living in Chile.

To my supervisors professors Pablo Irrarrázaval and Marcelo Andía for all the help, support, taught in my understanding of magnetic resonance phenomena and human physiology that they has given me to reach this goal.

To Cristian Tejos and Sergio Uribe for their tips and advice during this research.

To Flavia Zacconi for her help and support in the chemistry area to understand spectroscopy and the structure of fatty acids.

To Superior Educational National Secretary in Science and Technology (SENESCYT) Science and Technology (SENESCYT) 2012 convocatory from the Government of Ecuador, for the scholarship.

To the National Commission for Scientific Technological Research CONICYT - PCHA / Doctorado Nacional / 2015-21150021 from the Government of Chile, for the scholarship.

And finally I would like to acknowledge the Biomedical Imaging Center's members for their support and pleasant work atmosphere.

TABLE OF CONTENTS

ACKNOWLEDGEMENTS	iv
LIST OF TABLES	vii
LIST OF FIGURES	ix
ABSTRACT	xiii
RESUMEN	xv
1. INTRODUCTION	1
1.1. Outline of the Thesis Document	3
2. PERFUSION	4
2.1. Abstract	4
2.2. Introduction	5
2.3. Materials and methods	7
2.3.1. Study Data and Subjects	7
2.3.2. MRI Protocol	7
2.3.3. Image Analysis	9
2.3.4. Statistical Analysis	10
2.4. Results	10
2.5. Discussion	16
2.6. Conclusion	17
2.7. Acknowledgements:	17
2.8. Future Work:	17
3. SPECTROSCOPY	19
3.1. Abstract	19
3.2. Introduction	19
3.3. Materials and methods	22
3.3.1. Fatty acid estimation	22

3.3.2. Sensitivity Analysis	24
3.3.3. Phantom validation	25
3.3.4. Sample Labeling	27
3.4. Results	28
3.5. Conclusion	32
3.6. Acknowledgements:	34
3.7. Future Work:	35
4. METABOLIC IMAGES	36
4.1. Abstract	36
4.2. Introduction	37
4.3. Materials and methods	40
4.3.1. Phantom simulation	41
4.3.2. Metabolite estimation	43
4.3.3. FA estimation	47
4.4. Results	48
4.5. Discussion	49
4.6. Conclusion	52
4.7. Acknowledgements:	55
4.8. Future work:	55
5. FINAL CONCLUSION	56
References	57

LIST OF TABLES

2.1	Demographic information and clinical diagnosis of CLD patients include in this study. PBC: Primary Biliary Cirrhosis, NASH: Non alcoholic Steatohepatitis, ALD: Alcoholic Liver Disease	8
2.2	Heart frequency and inversion times (TI1 and TI2) for the one and two cardiac cycle MR protocols in Healthy volunteers and PH patients	12
2.3	Liver volume, spleen volume and IHPVBV for 1RR and 2RR protocols, for healthy volunteers (n=10) and patients with portal hypertension (n=10). IHPVBV: intrahepatic portal vein blood volume, LV: liver volume, SV: spleen volume, 1RR: one heart cycle, 2RR: two heart cycles.	13
3.1	Protonic matrix of the eight FA used in this work. The protonic matrix indicates the number of proton for each metabolite characterized by its spectral frequency in Hz and its chemical shift in ppm.	24
3.2	Reduced protonic matrix, without linear dependency.	24
3.3	Weights (g/100g FA), standard deviation in grams (D) from FA found by Araya at al. 2004, and weights used for the simulated and physical phantom (mg/100mg FA) of the FA used present in the liver in three conditions: healthy, steatosis, and steatohepatitis normalized for the eight FA used.	26
3.4	FA physiological composition constrains in g/100g FA used in the optimization algorithm for the three constrains (LB: lower bound, UB: upper bound).	26
3.5	FA composition estimated by the optimization method (x_{Est}) compared with Table 3.3 data in the three fat liver phantoms: healthy (x_{CN}), with steatosis (x_{ST}), and with steatohepatitis (x_{SH}). $ EAbs $ is the absolute value of the FA estimation error.	31
3.6	Percentage of precision for classification in three liver groups using the three constrains. Sens: sensitivity; Spec: specificity; np : percentage Gaussian added noise	34
4.1	FA percentual presence in edible oils by GC. C: carbon chain length; ndb: number of double bounds.	41

4.2	Protonic matrix A	41
4.3	Phantom metabolic presence for sunflower (G), corn (C), water (W), olive (O) and soybean (S) from GC	43
4.4	Different α and β values used	44
4.5	Constraints used for the FA estimation with one standard deviation. LB: lower bound. UB: upper bound	48
4.6	Metabolic percentage estimation (test 5 with an inhomogeneity field of [30 -30] Hz corrected). Est: estimated. Eabs: absolute error from the theoretical values	50
4.7	FA percentage estimation from corrected phase. Est: estimated. Eabs: absolute error. .	50

LIST OF FIGURES

2.1	(A) Schematic representation of the portal vein flow (Q), the liver resistance (R_{Liver}) and the portal pressure gradient (PPG) between the portal vein and the inferior vena cava. (B-C) Expected portal vein blood volume that flows into the intrahepatic volume (IHPVBV) in a certain number of cardiac cycles in a healthy volunteer and a patient with portal hypertension. It is expected that in healthy volunteers the hepatic vascular resistance is low, resulting in larger IHPVBV compared with PH patients.	7
2.2	TIR-ASL sequence for two cardiac cycles: non-selective inversion pulse (nsIR), selective inversion recovery pulse (sIR), respiratory navigator restoration (NR), respiratory navigator (N), inversion time 1 (TI1), inversion time 2 (TI2), trigger delay (TD), acquisition (AQ). The portal vein blood is labeled during the systole of the first cardiac cycle, and the image is acquired in the late diastole of the second cardiac cycle. The static tissue is almost completely suppressed by the two non-selective inversion pulses, while the portal vein blood keep its signal due the use of the selective inversion pulse. The total labeling time of the portal vein blood is TI1+TI2.	9
2.3	(A) Scan planning to obtain the intrahepatic portal vein venogram. Box “A” shows the volume of labeled blood over the portal vein main sources. The dotted line represents the acquired liver volume. (B) 3D Maximum Intensity Projections (MIP) reconstruction of an intrahepatic portal vein for one (1RR) and two (2RR) cardiac cycles in a representative healthy volunteer and PH patient.	10
2.4	Automatic subject-dependent threshold selection for the intrahepatic portal vein blood volume quantification from the TIR-ASL acquisition. The Otsu method was used to identify the optimum threshold between the high signal from the portal vein blood that flowed into the intrahepatic space, and the almost completely suppressed signal from the static tissues. LDO: liver distal object.	11
2.5	(A) Liver segmentation and volume quantification from the 3D Inversion Recovery MR acquisition. (B) Spleen segmentation and volume quantification from the 3D SSFP Balanced acquisition. H: head, F: foot, R: right, L: left, A: anterior, P: posterior. . . .	11

2.6	Healthy volunteers and PH patients median and interquartile (IQ) range of the (A) liver volume (LV) (no statistically significant difference), (B) spleen volume (SV) ($P = 0.023$), and (C) liver to spleen volume ratio ($P = 0.023$).	14
2.7	3D reconstruction of IHPVBV in one and two cardiac cycles from the TIR-ASL acquisitions. The images show larger IHPVBV in healthy volunteers (A) than PH patients (B) for both protocols. H: head, F: foot, R: right, L: left, A: anterior, P: posterior.	15
2.8	Healthy volunteers and PH patients median and interquartile (IQ) range for the intrahepatic portal vein volume adjusted by liver volume in (A) one cardiac cycle ($P < 0.001$) and (B) two cardiac cycles ($P < 0.001$).	15
2.9	Intrahepatic portal vein volume adjusted by liver volume measured in the two cardiac cycles protocol and liver-to-spleen volume ratio for healthy volunteer and PH patients. The combination of both parameters identified the PH patients with a sensitivity of 90% and specificity of 100%.	16
3.1	Example of fat spectrum showing the metabolites at 9.4T. In this work we are not considering the glycerol peaks.	23
3.2	Protonic distribution of linoleic FA C18:2; H: proton; TH: total protons; O: oxygen; C: carbon; α_c : alpha carboxyl; β_c : beta carboxyl; a: allyl; o: olefinic; d: dyallil; m: methyl; mb: bulk methylene.	25
3.3	FA concentration distribution in the three liver stages: healthy (CN), steatosis (ST) and steatohepatitis (SH). Mi: myristic, Ml: myristoleic, Pa: palmitic, Pl: palmitoleic, Es: stearic, Ol: oleic, Li: linoleic, Ln: linolenic.	29
3.4	MR spectrum of the three liver phantoms acquired at 9.4 T and the AUC calculated for each metabolite. Note that the spectra are quite similar but they have little differences. The differences can be seen in AUC from control (Z_{CN}), steatosis (Z_{ST}) and steatohepatitis (Z_{SH}) spectra.	30
3.5	L2 norm of the error between the actual FA composition and the estimated by the proposed methodology for the simulated spectrum (A) and for the acquired liver spectrum (B).	30

3.6	Relation between the actual FA composition in each phantoms and the estimated composition using the proposed method.	31
3.7	Bland-Altman plot for the differences between the estimated and the literature data from the three liver phantoms: (A) healthy, (B) with steatosis and (C) with steatohepatitis. .	32
3.8	Relation between the magnitude of the Gaussian error added to the simulated MR spectrum (\vec{z}) and the L2 norm of the error between the simulated and the actual values of \vec{x} for the 3 clinical conditions normal (CN), steatosis (ST) and steatohepatitis (SH). .	32
3.9	Distribution of the difference between the estimated FA composition (\vec{x}_{Est}) and the simulated FA composition (\vec{x}) from Table 3.3 for myristic FA. In the rows are the Gaussian error added (ns) and in the columns the liver samples: healthy (CN), with steatosis (ST) and with steatohepatitis (SH).	33
3.10	Sensitivity and specificity of the proposed method to differentiate between normal and diseased liver (A) and between ST and SH (B) form simulated spectrum with five different magnitude of added Gaussian noise (np). Sens: sensitivity; Spec: specificity. .	35
4.1	Simulated digital image phantom for a $TE = 18.4ms$ with magnetic field inhomogeneities [30 -30] Hz. (A) Absolute value. (B) Real value. (C) Imaginary value. (D) Sample correspondence: G sunflower, C corn, W water, O olive, Y soybean	44
4.2	(A) Field inhomogeneity estimated from digital phantom created with an inhomogeneity field of [30 -30] Hz without phase correction, and (B) with phase correction	48
4.3	Comparison between the metabolic estimation and original values for each oil and water sample (test 5 with an inhomogeneity field of [30 -30] Hz).	49
4.4	Metabolites estimation for each oil and water sample (test 5 with an inhomogeneity field of [30 -30] Hz corrected). The gray scale shows the percentage of presence.	51
4.5	Comparison between FA estimation and original values for each oil (test 5 with an inhomogeneity field of [30 -30] Hz)	52
4.6	FA estimation from the simulated phantom for the edible oils corrected. The gray scale means the percentage presence.	52
4.7	Absolute errors between original and estimated data for metabolites. In the right is the estimated field map correction of the simulated phantom which shows the inhomogeneity	

	field added to vertical and horizontal axis. (A) [0 0] Hz. (B) [30 -30] Hz. (C) corrected [30 -30] Hz. (D) [60 -60] Hz. (E) corrected [60 -60] Hz.	53
4.8	Absolute errors between original and estimated data for FA. (A) [0 0] Hz. (B) [30 -30] Hz. (C) corrected [30 -30] Hz. (D) [60 -60] Hz. (E) corrected [60 -60] Hz.	54

ABSTRACT

Among others, the liver's main functions are: the synthesis of plasma proteins, perform a detoxifying function, the glycogen storage, and the secretion of bilirubin and cholesterol, among others. It is responsible for neutralizing and eliminating blood substances that may be harmful to the body. Excessive consumption of alcohol, carbohydrates and fats are behaviors that alter the integrity of liver cells. A hallmark of this damage is the intracellular accumulation of fat microvesicles. This fat accumulation is called hepatic steatosis that, persisting over time, can lead to steatohepatitis or cirrhosis.

The gold standard for diagnosis of hepatic steatosis is biopsy in which a sample of liver tissue is removed and the content of intracellular fat is quantified. This is an invasive and risky procedure, with sampling problems since it only takes a 0.05% of the total organ. Therefore, a non-invasive method to quantify fat is highly desirable. A liver with steatosis can progress to cirrhosis or chronic liver disease (CLD) and portal hypertension (PH) is a frequent condition in this patients which is characterized by an increased liver resistance to blood flow.

Not all the accumulated fat tissue has the same chemical and biological characteristics. Besides, fat accumulated in one patient does not necessarily have the same characteristics as the fat accumulated in other patients. Therefore it is not only necessary to look for a better methods for quantification of total fat, but also improve its non-invasive characterization.

In this work we propose ways to measure liver fat content and the liver integrity using new non-invasive MR methods, such as intrahepatic portal hypertension, and MRS to characterize the presence of fatty acids in a voxel. The final idea is to extrapolate this voxel characterization as an image, using MRI. The aim is to characterize the fat through its metabolites and quantify the fat considering all its spectrum. In addition, through an optimization algorithm, we can estimate the type of fatty acids present, in order to model the state of the fat and also classify it as normal, hepatic steatosis or steatohepatitis.

Results from perfusion work show that it can be possible to classify patients with portal hypertension from healthy volunteers, and it suggest that is possible to establish a scale of steatosis degree using the intrahepatic portal vein blood volume. In the spectroscopy work, results show that

is possible to estimate the fatty acid presence in a voxel using 9.4T MRS. Finally, in the metabolic images work, results show that is possible to extract the fat and water metabolite information from images and therefore estimate the fatty acid presence using 1.5T MRI.

Keywords: Fat quantification, magnetic resonance imaging, magnetic resonance spectroscopy.

RESUMEN

Entre otras, el hígado tiene como funciones principales la síntesis de proteínas plasmáticas, una función desintoxicante, almacenaje de glucógeno, secreción de bilirrubina y colesterol. Es el responsable de neutralizar y eliminar de la sangre sustancias que puedan resultar nocivas para el organismo. El consumo excesivo de alcohol y grasas son comportamientos que alteran la integridad de las células hepáticas. Un signo característico es la acumulación intracelular de microvesículas de grasa. A esta acumulación de grasa se le denomina esteatosis hepática, que si persiste en el tiempo puede producir esteatohepatitis y finalmente cirrosis.

El principal método de diagnóstico de la esteatosis hepática es la biopsia, que extrae una muestra del tejido hepático y cuantifica el contenido de grasa intracelular en el laboratorio. Este es un procedimiento invasivo y riesgoso, con problemas de muestreo ya que solo toma un 0.05% del total del órgano. Por esta razón, es necesario un método de cuantificación no invasivo y global. Un hígado con esteatosis puede progresar hasta cirrosis o enfermedad crónica hepática (CLD) y la hipertensión portal (PH) es una condición frecuente en estos pacientes que se caracterizan por un incremento en la resistencia del hígado al flujo de sangre.

No toda la grasa acumulada en los tejidos tiene las mismas características químicas ni biológicas. Además, la grasa acumulada por un paciente no necesariamente tiene las mismas características que la grasa acumulada por otros pacientes. Por lo tanto no solo es necesario avanzar en una mejor cuantificación de la grasa total, sino que también en su caracterización no-invasiva. En este trabajo se proponen algunas formas de medir la cantidad de grasa en el hígado utilizando métodos indirectos, como la hipertensión portal intrahepática, y la espectroscopía para caracterizar la presencia de ácidos grasos en un voxel, con el objetivo de extrapolar este trabajo a una imagen. El objetivo es caracterizar la grasa por medio de sus metabolitos. Además, por medio de un algoritmo de optimización, se puede estimar qué tipo de ácidos grasos la conforman, con el objetivo de modelar el estado de la grasa y también clasificarlo como normal, esteatosis hepática o esteatohepatitis.

Los resultados del trabajo de perfusión muestran que es posible clasificar pacientes con hipertensión portal de voluntarios sanos, y sugiere que es posible establecer una escala del grado de

esteatosis presente utilizando el volumen de sangre en la vena portal intrahepática. En el trabajo de espectroscopía, los resultados muestran que es posible estimar la presencia de ácidos grasos en un voxel utilizando MRS de 9.4T. Finalmente, en el trabajo de imágenes metabólicas, los resultados muestran que es posible extraer la información metabólica de agua y grasa desde las imágenes y por tanto estimar la presencia de ácidos grasos utilizando MRI de 1.5T.

Palabras Claves: Cuantificación de grasa, imágenes de resonancia magnética, espectroscopía de resonancia magnética.

1. INTRODUCTION

Non alcoholic Fatty liver disease (NAFLD) is characterized by excessive and abnormal fat accumulation in liver cells. Currently the best way to evaluate the amount of liver fat is through a biopsy but it has some problems. It is invasive and it has sampling and monitoring problems. For this reason it is not a suitable diagnostic method (Peterson & Mansson, 2013). From a pathology point of view, fatty liver disease is evaluated in hepatocytes that contained microvesicles of fat using a visual scale of 0 for less than 5 %, 1 for 5% to 33%, 2 for 33% to 66%, and 3 for more than 66% (Tang et al., 2013).

Hepatic steatosis causes that hepatocytes accumulate an excess of fat with the risk of reaching an inflammatory state and then cirrhosis. The chronic injury of fat accumulation leads to the activation of the inflammation cascade, Kupffer cell activation, apoptosis and collagen deposits (Kumar V., Abbas K., & Fausto N., 2005). Historically, only the total fat has been quantified. The gold standard for this quantification is the biopsy. Some patients evolve to cirrhosis which first sign is portal hypertension. The gold standard to diagnose portal hypertension is the invasive measurement of the gradient pressure between the cava and portal vein (Armonis, Patch, & Burroughs, 1997; Bosch, Abraldes, Berzigotti, & Garcia-Pagan, 2009; Chelliah et al., 2011; Merkel & Montagnese, 2011; Berzigotti, Seijo, Reverter, & Bosch, 2013).

Magnetic resonance is a non-invasive technique that allows to quantify tissue differences, flow and chemical shift in the body. Magnetic Resonance Imaging (MRI) is a technique to acquire high resolution images. It is somewhat non dependent on the skill of the operator, as it is ultrasound, and the acquired signal can be decomposed in different chemical species such as water and fat. More importantly, it does not use ionizing radiation such as the X-ray computed tomography (Kumar V. et al., 2005). Magnetic Resonance Spectroscopy (MRS) is a technique which allows to measure fat as spectra. With MRI it is possible to measure the fraction of fat signal, defined as the fraction of the acquired corrected signal that corresponds to fat in the liver. This signal can be altered by various technical factors such as variation in relaxation times T1 (Brunt, Janney, Di Bisceglie, Neuschwander-Tetri, & Bacon, 1999), T1 effects and the bias noise (Fazel et al., 2009), magnetic field inhomogeneities or T2* (C.-Y. Liu, McKenzie, Yu, Brittain, & Reeder, 2007), the spectral complexity fat (Yu et al., 2008), J coupling or intrinsic behavior of all peaks in the spectrum of fat (Bydder, Yokoo, et al., 2008), and eddy currents or disturbance in the phase information (Yu et al.,

2007), which can show unreliable results of the lipid content. The most advanced techniques in MRI measures the proton density fat fractions (PDFF), which is a fundamental property of tissue defined as the fraction of protons attributed to liver fat and a direct measure of the amount of fat in the liver (Hamilton et al., 2009).

There are some methods to quantify fat in the liver using MRI like PDFF (Yokoo et al., 2011; Tang et al., 2013; Zand et al., 2015), multipeak fat spectral with iterative decomposition of water and fat with echo asymmetry and least-squares estimation (MP-IDEAL) (Meisamy et al., 2011a), compressed sensing with parallel imaging (Mann et al., 2015), PDFF with chemical shift encode (Motosugi et al., 2015), enhanced images with ferumoxytol (Smits et al., 2015), but they provide results with only the principal components of fat and generally only considering a slice. MR Elastography quantify in a noninvasively way the stiffness of the liver which increment with the fibrosis stage but is not reliable method (Faria et al., 2009). Diffusion Weighted Imaging (DWI) is a functional MRI method that provides a noninvasive quantification of microcapillary-blood perfusion but its mechanism with chronic liver disease is not clearly understood (Taouli, Ehman, & Reeder, 2009a). Other methods use magnetic resonance spectroscopy (MRS), such that the frequency spectrum of a sample permits the differentiation of groups of peaks or metabolites with some spectral resolution, including fat; its disadvantage is the low spectral resolution and sampling, it does not allow an image and it general is single voxel (volume element) with same limitations as biopsy.

MRS offers a unique advantage to quantify and characterize the liver fat presence when the spectrum is analyzed. This spectrum is characterized by eleven zones or peaks where seven of them correspond to fat signal and the others to glycerols. The fat is composed of triglycerides and it is formed by a glycerol and three fatty acids. These fatty acids can be described by the hydrogen (H) presence in each metabolite, so a spectrum is a linear combination of many fatty acids. Using gas chromatography (GC) is possible to measure the presence of fatty acids in liver samples (Araya et al., 2004a) and in recent years there are studies that apply MRS to characterize saturated, monosaturated and polysaturated fatty acids in oils (Guillen & Ruiz, 2003a) (Vlahov, 1999b) using the relationship between the areas of peaks. However, this is not a method to estimate the specific fatty acids presence in a sample but a group of them.

A liver with steatosis can progress to cirrhosis or chronic liver disease (CLD) and portal hypertension (PH) is a frequent condition in these patients which is characterized by an increased liver resistance to blood flow. MRI use to estimate portal hypertension has been described as 4D flow technique (Roldan-Alzate et al., 2013) that fundamentally do not employ contrast media, and with contrast media (Bahl et al., 2012; Cao et al., 2013; Peeters, Annet, Hermoye, & Van Beers, 2004; N. K. Lee et al., 2012) that paradoxically is not recommended for patients with hepatic disease. There are techniques that do not use contrast media such as Arterial Spin Labeling (ASL) (Gach H. M., Li T., Lopez-Talavera J. C., & Kam A. W., 2002; Kanematsu et al., 2012; Katada et al., 2012). In this work we use the technique TIRASL (Andia & Botnar, 2012) to calculate the required amount of blood present in the intrahepatic vein. We consider possible cases where there is a bypass from the portal vein to the superior cave vein, to avoid passing through the liver due to its high resistance.

In this work we propose to advance in the development of MR techniques for the early detection and quantification of portal hypertension and fatty liver characterization. To achieve this quantitative image techniques should satisfy certain properties. One of these properties is precision which can be reached acquiring images from a same volunteer in different times and comparing the results of each acquisition; while these results are similar there will be a high precision measurement. Another property is the inter-reader reproducibility which can be reached evaluating the obtained and classified image results by some experts in the field. A final property is the accuracy which can be reached making a correlation with an accepted standard and then measure its sensitivity and specificity.

1.1. Outline of the Thesis Document

This work has three aims:

The first objective is to develop and validate an MRI technique to improve the early diagnosis of portal hypertension as a surrogate marker of liver fibrosis, and to differentiate between healthy subjects and patients. This objective will be explained in detail in Chapter 2.

The second objective is to characterize the hepatic fat in a liver voxel using MRS for establishing a reference model from the liver spectra and the relative presence of the principal fatty acids. This objective will be explained in detail in Chapter 3.

Finally, the third objective is to quantify and characterize the fatty acids from a simulated digital phantom with edible oils and water information. The aim is to characterize hepatic steatosis by MRI in order to obtain an image of the fatty acids distribution as a future work. This objective will be explained in detail in Chapter 4.

2. PERFUSION

This chapter explains the developments to meet the first objective, to detect the first signs of portal hypertension as a result of chronic liver damage due to other causes, fat accumulation in the liver. We classify our results as normals or abnormal.

2.1. Abstract

Purpose: To investigate the feasibility of estimating the portal vein blood volume that flows into the intrahepatic volume (IHPVBV) in each cardiac cycle using non-contrast MR venography technique as a surrogate marker of portal hypertension (PH). **Materials and Methods:** Ten patients with chronic liver disease and clinical symptoms of PH (40% males, median age:54.0, range:44-73y.o.) and ten healthy volunteers (80% males, median age:54.0, range:44-66y.o.) were included in this study. A non-contrast Triple-Inversion-Recovery Arterial-Spin-Labeling (TIR-ASL) technique was used to quantify the IHPVBV in one and two cardiac cycles. Liver (LV) and spleen volume (SV) were measured by manual segmentation from anatomical MR images as morphological markers of PH. All images were acquired in a 1.5T Philips Achieva MR scanner. **Results:** PH patients had larger SV ($P=0.02$) and lower liver-to-spleen ratio ($P=0.02$) compared with healthy volunteers. The median IHPVBV in healthy volunteers was 13.5 cm^3 and 26.5 cm^3 for one and two cardiac cycles respectively, whereas in PH patients a median volume of 3.1 cm^3 and 9.0 cm^3 was observed. When correcting by LV, the IHPVBV was significantly higher in healthy volunteers than PH patients for one and two cardiac cycles. The combination of morphological information (liver-to-spleen ratio) and functional information (IHPVBV/LV) can accurately identify the PH patients with a sensitivity of 90% and specificity of 100%. **Conclusion:** Results show that the portal vein blood volume that flows into the intrahepatic volume in one and two cardiac cycles is significantly lower in PH patients than in healthy volunteers and can be quantified with non-contrast MRI techniques.

Keywords: portal hypertension, intrahepatic portal vein, Arterial Spin Labeling, cirrhosis, non-contrast MRI.

2.2. Introduction

Portal hypertension (PH) is a frequent condition in patients with chronic liver diseases (CLD) which is characterized by an increased liver resistance to blood flow. The portal vein is a low pressure system, so this increased resistance induces a rise in the portal pressure gradient (PPG) (Fig. 2.1 A), leading to marked hepatic hemodynamic changes characterized by a decrease in the contribution of portal vein to liver perfusion (Kapoor & Sarin, 2002). The clinical relevance of PH derives from the frequency and severity of its complications, which represent the first cause of hospital admission, death and liver transplantation in patients with cirrhosis (Abraldes et al., 2003).

It has been suggested that the severity of PH should be evaluated in all CLD patients as a surrogate measure of the severity of the liver chronic damage and mortality risk, as well as to evaluate the response to treatments (Armonis et al., 1997). The gold-standard method to measure the portal venous pressure involves an invasive catheterization of the cava and hepatic veins, and the measurement of the hepatic venous pressure gradient (HVPG) (Armonis et al., 1997) (Bosch et al., 2009) (Chelliah et al., 2011) (Merkel & Montagnese, 2011) (Berzigotti et al., 2013). This method is invasive, use ionizing radiation, and the need of sedative agents could modify the hemodynamic response. Some non-invasive methods to indirectly estimate the HVPG have also been proposed. The arterial enhancement fraction technique (AEF) uses X-ray images to assess the hemodynamic changes associated with diffuse liver disease (Kang et al., 2011) (Ou et al., 2013), assuming that the AEF indirectly reflects the relationship between arterial perfusion and total (arterial and venous) perfusion (Kim et al., 2009). However, this technique requires ionizing radiation and a iodinated contrast agent, making it unsuitable for high-risk patients. A variety of methods based on magnetic resonance imaging (MRI) have also been proposed. Arterial Spin Labeling (ASL) has been applied to evaluate the liver perfusion in (Gach H. M. et al., 2002; Kanematsu et al., 2012; Katada et al., 2012). Classical ASL requires a long scanning time when imaging the whole liver due to subject breathing (Katada et al., 2012), it is sensitive to motion due to the subtraction step required to suppress the static background, and has low signal-to-noise ratio, producing low-quality images that are not appropriate for quantification. A different approach to estimate the portal vein flow based on MRI Phase Contrast (PC) technique has also been used (Hoad C. et al., 2011; Burkart, Johnson, Morton, Wolf, & Ehman, 1993; Vermeulen et al., 2012; Yzet, Bouzerar, Baledent, et al.,

2010; Annet et al., 2003; Yzet, Bouzerar, Allart, et al., 2010). Two-dimensional (2D)-PC portal vein flow measurement may not take into account the porto-systemic shunt upstream of the level of measurement (Almadi M. A., Almessabi A., Wong P., Ghali P., & Barkun A., 2011; Akhter & Haskal, 2012; Landgraf et al., 2014), and could lead to an overestimation of the portal vein blood volume that effectively flows into the liver. Additionally, both the magnetic field inhomogeneities in the abdominal cavity and the need for an accurate definition of the vessels' geometry make it difficult to obtain reliable data using 2D-PC technique. Four-dimensional (4D)-PC portal vein flow technique could take into account the porto-systemic shunt both with (Roldan-Alzate et al., 2013) and without (Stankovic et al., 2014) external contrast agents, but this technique has not been applied to PH patients. Alternatively, Time of Flight (TOF) technique has been used to visualize the portal system (Taylor & McCauley, 1992) with the aim of studying liver perfusion. The main drawback of this technique, when imaging PH patients, is that slow flow does not produce enough signal. Contrast-enhanced MRI has also been used for hepatic fibrosis grading and staging (Bahl et al., 2012) and for evaluating the portal vein contribution to liver perfusion (Cao et al., 2013) (Peeters et al., 2004). The radiological signal called "delayed hyperintense portal vein sign" in Gd-EOB-DTPA-enhanced MRI has been proposed as an indirect marker of PH that could reflect the hepatobiliary disease (N. K. Lee et al., 2012). Two hypotheses have been proposed to explain this sign: one related with the integrity of hepatocytes and the other one related with the delay in reaching the intrahepatic space of the contrast agent due to the increased PPG. However, this technique is not routinely used in CLD patients because it requires an intravenous contrast agent. Previously described techniques have not been incorporated into the clinical routine, and PH is still evaluated using morphological changes in the liver and spleen (such as splenomegaly and cirrhosis), and portal vein abnormalities (such as porto-systemic collaterals) (Thabut, Moreau, & Lebrech, 2011) (P. Liu, Li, He, & Zhao, 2009) (Murata et al., 2008). In this work a new non-contrast MRI technique is used with the aim of improving PH diagnosis by estimating its effect in the portal vein hemodynamics. We estimate the portal vein blood that flows into the intrahepatic volume (IHPVBV) in a certain number of cardiac cycles as a surrogate of the PPG. The rationality of this idea comes from the concept that portal pressure gradient is given by the product of the portal vein flow (Q) and the liver vascular resistance (R_{Liver}) (Kapoor & Sarin, 2002) (Fig. 2.1 A), similarly to any vascular system. In PH patients, the labeled blood will face larger vascular resistance to flow into the intrahepatic space, therefore, the IHPVBV is expected to be lower than in healthy volunteers

(Fig. 2.1 B-C) The measurement of the intrahepatic blood volume that flows in a standardized amount of time (e.g. in one or two cardiac cycles) would provide a good estimation of PPG/ R_{Liver} and indirectly measures the severity of PH. The proposed method is simple to plan and it is robust to magnetic field (B_0) inhomogeneities.

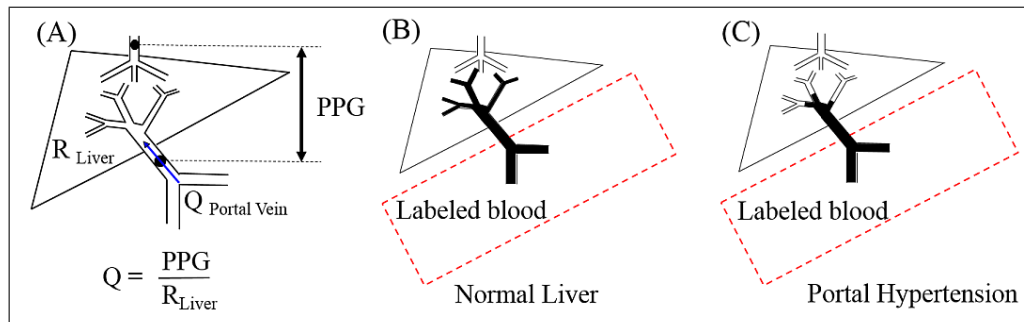


FIGURE 2.1. (A) Schematic representation of the portal vein flow (Q), the liver resistance (R_{Liver}) and the portal pressure gradient (PPG) between the portal vein and the inferior vena cava. (B-C) Expected portal vein blood volume that flows into the intrahepatic volume (IHPVBV) in a certain number of cardiac cycles in a healthy volunteer and a patient with portal hypertension. It is expected that in healthy volunteers the hepatic vascular resistance is low, resulting in larger IHPVBV compared with PH patients.

2.3. Materials and methods

2.3.1. Study Data and Subjects

The proposed technique was tested in ten patients with CLD and clinical diagnosis of PH (40% males, median age of 54.0, range: 44-73 y.o.) and 10 healthy volunteers (80% males, median age of 54.0, range: 44-66 y.o.). The inclusion criteria for PH patients were: confirmed diagnosis of CLD and clinical signs of PH, such as gastrointestinal bleeding from gastroesophageal varices, ascites, and hepatic encephalopathy (Table 2.1). The inclusion criteria for volunteers were no pathology known in liver. Exclusion criteria for patients and volunteers were: claustrophobia and the use of pacemaker. PH patients were referred to our institution after clinical diagnosis. The ethics committee of our institution approved the study and all subjects gave written informed consent.

2.3.2. MRI Protocol

In order to quantify the portal vein blood volume that flows into the intrahepatic space we used a non-contrast MR angiography technique that does not require the subtraction step as classic ASL methods (TIR-ASL (Andia & Botnar, 2012)). We expected that most of the PH patients have a

TABLE 2.1. Demographic information and clinical diagnosis of CLD patients include in this study. PBC: Primary Biliary Cirrhosis, NASH: Non alcoholic Steatohepatitis, ALD: Alcoholic Liver Disease

No.	Age	Sex	CLD Diagnosis	Clinical signs or symptoms of PH
1	44	F	PBC	Ascites, upper gastrointestinal bleeding
2	49	F	NASH	Ascites, upper gastrointestinal bleeding
3	50	F	NASH	Ascites, upper gastrointestinal bleeding
4	51	F	PBC	Ascites, upper gastrointestinal bleeding
5	53	F	Hepatitis C	Ascites, hepatic encephalopathy
6	54	M	ALD	Ascites, upper gastrointestinal bleeding
7	56	M	NASH	Ascites, upper gastrointestinal bleeding
8	61	M	NASH	Ascites, upper gastrointestinal bleeding
9	64	M	ALD	Ascites, upper gastrointestinal bleeding
10	73	F	NASH	Ascites, hepatic encephalopathy

slow portal vein flow, therefore we acquired the images using one (1RR) and two (2RR) cardiac cycles in order to increase the labeling time and to increase the blood volume that flows into the intrahepatic space. TIR-ASL technique uses a Triple Inversion Recovery pre-pulse and exploits the ability of two non-selective Inversion-Recovery pre-pulses to null background signal while maintaining the signal of labeled blood using a regional inversion pulse (Figure 2.2 (Peeters et al., 2004)). With the optimal selection of the inversion times TI1 and TI2 (Andia & Botnar, 2012), it is possible to null the static tissue and keep only the signal of the targeted blood. This sequence can be fitted either in one or two cardiac cycle intervals, obtaining the same effect but increasing the labeling time (TI1+TI2).

TIR-ASL was combined with an ECG triggered 3D-balanced SSFP gradient echo sequence with the following parameters: FOV=400×400×180 mm, acquisition matrix=672× 672 resulting in a 0.6× 0.6 mm in-plane spatial resolution, slice thickness=3 mm, TR/TE= 4.72/2.36 ms, FA=90°. A respiratory navigator with an acceptance window of 15 mm and a fat suppression pre-pulse preceded the imaging sequence. The scan planning to obtain the IHPVBV is showed in Figure 2.3 A, the box “A” indicates the blood volume labeled in the main abdominal venous systems below the liver. Table 2.2 shows the heart frequency and the TI1 and TI2 times used for each patient and healthy volunteer.

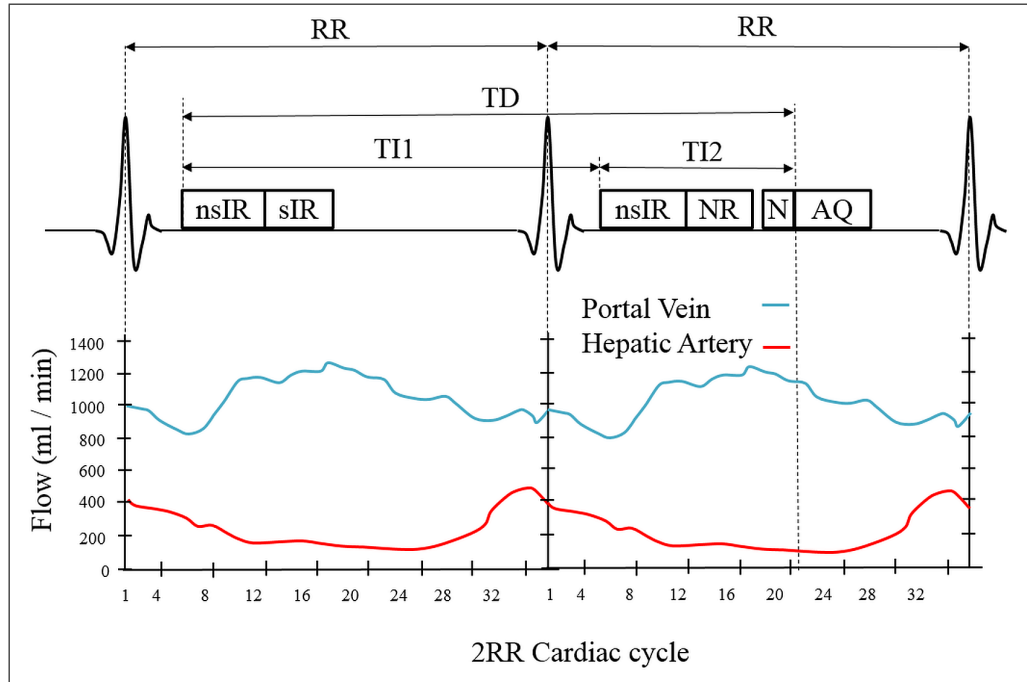


FIGURE 2.2. TIR-ASL sequence for two cardiac cycles: non-selective inversion pulse (nsIR), selective inversion recovery pulse (sIR), respiratory navigator restoration (NR), respiratory navigator (N), inversion time 1 (TI1), inversion time 2 (TI2), trigger delay (TD), acquisition (AQ). The portal vein blood is labeled during the systole of the first cardiac cycle, and the image is acquired in the late diastole of the second cardiac cycle. The static tissue is almost completely suppressed by the two non-selective inversion pulses, while the portal vein blood keep its signal due the use of the selective inversion pulse. The total labeling time of the portal vein blood is $TI1+TI2$.

In order to perform a morphological analysis, the liver and the spleen volumes that are typically used as indirect radiological marker for PH diagnosis (P. Liu et al., 2009) (Murata et al., 2008) were quantified. For the liver volume (LV) estimation a 3D Inversion Recovery sequence was used with the following parameters: FOV=400×400×180 mm, acquisition matrix=672×672 resulting in a 0.6×0.6 mm in-plane spatial resolution, slice thickness=3 mm, TR/TE=4.3/1.34 ms, FA=30° with an inversion time between 500 and 600 ms according to the patient heart frequency. For the spleen volume (SV) estimation a 3D-balanced SSFP gradient echo sequence was used with the following parameters: FOV=400×400×180 mm, acquisition matrix=672×672 resulting in a 0.6×0.6 mm in-plane spatial resolution, slice thickness=3 mm, TR/TE=5.0/2.5 ms, FA=70°. All the images were acquired in a 1.5T Achieva MR scanner (Philips Healthcare, Best, NL) using a four-element body coil, and all subjects had at least 6 hours of fasting before the imaging session.

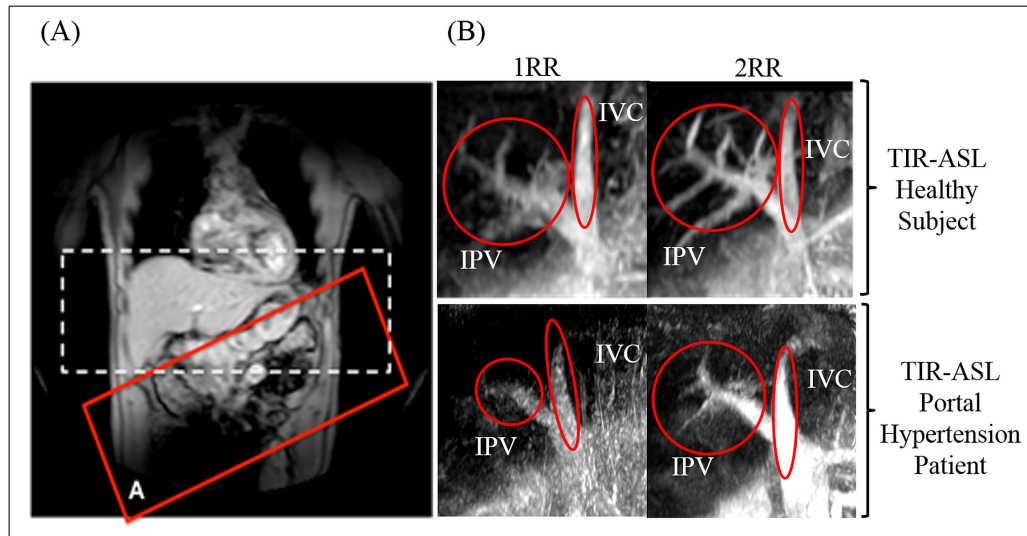


FIGURE 2.3. (A) Scan planning to obtain the intrahepatic portal vein venogram. Box “A” shows the volume of labeled blood over the portal vein main sources. The dotted line represents the acquired liver volume. (B) 3D Maximum Intensity Projections (MIP) reconstruction of an intrahepatic portal vein for one (1RR) and two (2RR) cardiac cycles in a representative healthy volunteer and PH patient.

2.3.3. Image Analysis

In order to calculate the IHPVBV in one and two cardiac cycles, an intensity-based image segmentation algorithm was applied to the intrahepatic portal vein images obtained with TIR-ASL, using an in-house developed MATLAB application (The MathWorks, Natick, MA, USA) (Fig. 2.3 B and Fig. 2.4). In TIR-ASL images blood has high intensity, while the liver and other static structures are almost completely suppressed (Fig. 2.3 B). A subject dependent intensity threshold was defined using the Otsu method (Otsu N., 1979) based on five regions of interest (ROI) (Fig. 2.4). On the other hand, the liver and spleen were manually segmented in a slice-by-slice manner (Fig. 2.5) and their volume was calculated using an in-house developed MATLAB application.

2.3.4. Statistical Analysis

Statistical analysis was performed using Mann-Whitney independent-samples test, and receiver operating characteristic (ROC) analysis, using a SPSS v20.0 package (IBM Software Group, New York, USA).

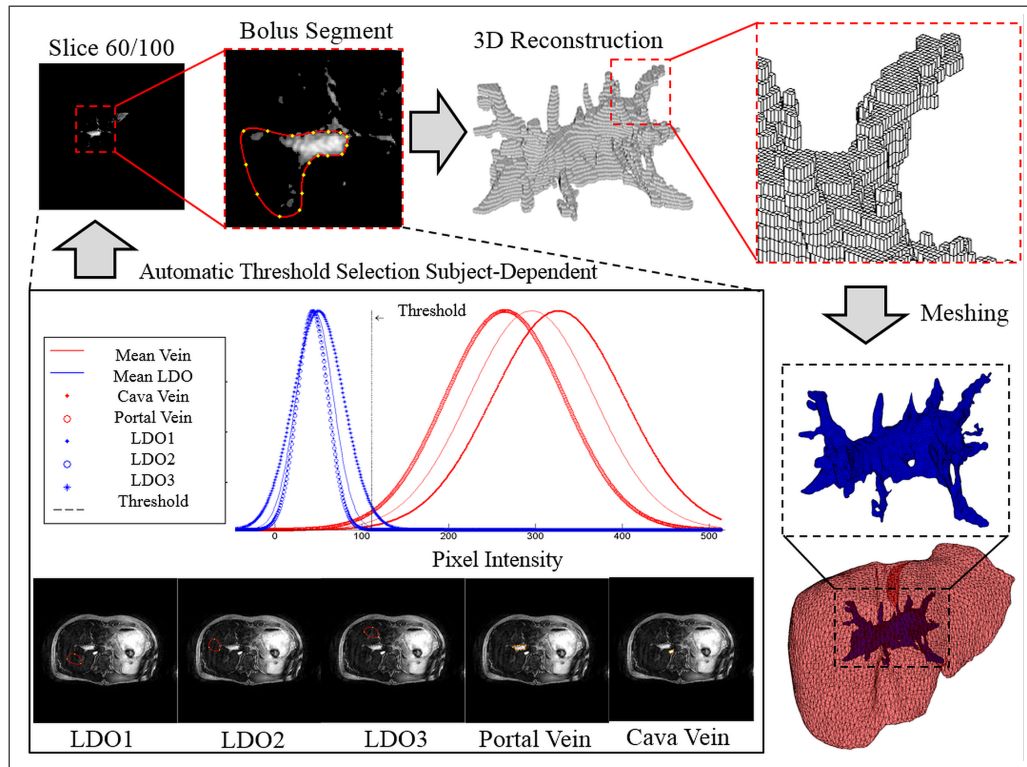


FIGURE 2.4. Automatic subject-dependent threshold selection for the intrahepatic portal vein blood volume quantification from the TIR-ASL acquisition. The Otsu method was used to identify the optimum threshold between the high signal from the portal vein blood that flowed into the intrahepatic space, and the almost completely suppressed signal from the static tissues. LDO: liver distal object.

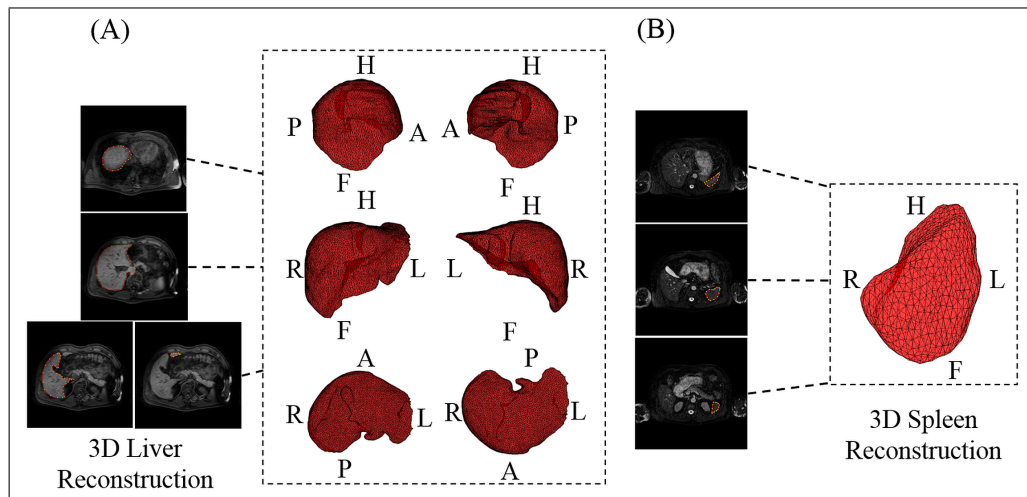


FIGURE 2.5. (A) Liver segmentation and volume quantification from the 3D Inversion Recovery MR acquisition. (B) Spleen segmentation and volume quantification from the 3D SSFP Balanced acquisition. H: head, F: foot, R: right, L: left, A: anterior, P: posterior.

TABLE 2.2. Heart frequency and inversion times (TI1 and TI2) for the one and two cardiac cycle MR protocols in Healthy volunteers and PH patients

No.	Heart Frequency (bpm)	1RR Protocol		2RR Protocol	
		TI1 (ms)	TI2 (ms)	TI1 (ms)	TI2 (ms)
Healthy Volunteers					
1	57	442	169	825	265
2	93	291	122	571	206
3	58	442	169	825	265
4	61	442	169	825	265
5	76	352	142	724	243
6	66	406	158	825	265
7	66	406	158	724	243
8	81	329	135	649	225
9	71	379	150	724	243
10	73	379	150	724	243
PH Patients					
1	91	291	122	649	225
2	76	352	142	724	243
3	69	379	150	825	265
4	60	442	169	825	265
5	65	406	158	825	265
6	62	442	169	825	265
7	70	379	150	724	243
8	54	486	182	939	288
9	68	379	150	724	243
10	60	442	169	825	265

2.4. Results

The LV, SV and IHPVBV were quantified for one and two cardiac-cycles in all volunteers and PH patients (Table 2.3).

From the morphological analysis, no statistically significant differences were found in the LV between healthy volunteers and PH patients, however PH patients presented larger SV ($P=0.023$) and lower liver-to-spleen volume ratio ($P=0.023$) compared with healthy volunteers (Fig. 2.6).

TABLE 2.3. Liver volume, spleen volume and IHPVBV for 1RR and 2RR protocols, for healthy volunteers ($n=10$) and patients with portal hypertension ($n=10$). IHPVBV: intra-hepatic portal vein blood volume, LV: liver volume, SV: spleen volume, 1RR: one heart cycle, 2RR: two heart cycles.

No.	LV (cm ³)	SV (cm ³)	LV/SV	IHPVBV 1RR (cm ³)	IHPVBV 2RR (cm ³)
Healthy Volunteers					
1	2083.0	278.7	7.5	22.9	30.7
2	1505.8	194.9	7.7	6.4	24.7
3	1423.3	132.0	10.8	7.7	19.7
4	1720.4	561.3	3.1	18.9	26.8
5	1435.1	88.8	16.2	18.3	26.1
6	1913.7	122.5	15.6	14.6	33.3
7	1706.5	127.5	13.4	9.0	30.0
8	1795.9	247.4	7.3	12.3	20.6
9	1754.8	144.8	12.1	10.2	18.5
10	1387.7	212.0	6.5	15.1	28.2
PH Patients					
1	1933.8	281.1	6.9	2.0	2.1
2	2114.3	697.6	3.0	8.1	9.8
3	1575.3	224.6	7.0	0.2	2.4
4	1319.6	146.7	9.0	8.3	13.0
5	2439.6	805.4	3.0	0.3	18.3
6	948.2	347.2	2.7	2.8	3.3
7	2525.7	1121.1	2.3	10.9	33.0
8	990.6	312.0	3.2	0.1	0.1
9	1383.7	776.2	1.8	4.5	15.5
10	1046.3	508.0	2.1	3.3	8.2

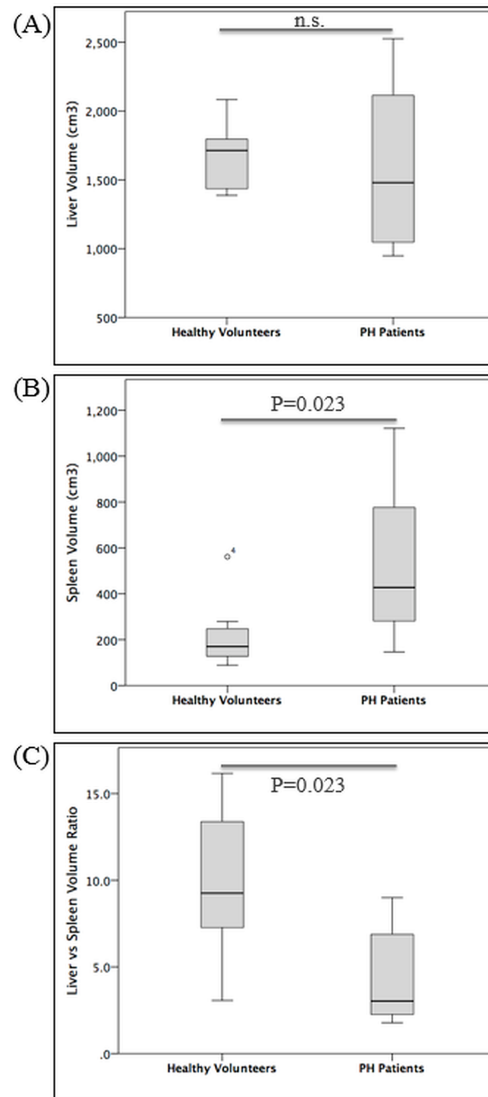


FIGURE 2.6. Healthy volunteers and PH patients median and interquartile (IQ) range of the (A) liver volume (LV) (no statistically significant difference), (B) spleen volume (SV) ($P = 0.023$), and (C) liver to spleen volume ratio ($P = 0.023$).

Larger IHPVBV in healthy volunteers than PH patients, for both acquisition protocols (one and two cardiac cycles) were observed (Fig. 2.7 and Fig. 2.8). The median IHPVBV in healthy volunteers was 13.5 cm^3 and 26.5 cm^3 in one and two cardiac cycles, respectively, whereas in PH patients median volumes of 3.1 cm^3 and 9.0 cm^3 in one and two cardiac cycles were observed. The IHPVBV corrected by the liver volume (IHPVBV/LV) was significantly higher in healthy volunteers than PH patients in both protocols ($P < 0.001$) (Fig. 2.8). The median TIR-ASL acquisition time was 8.9 min and 9.6 min for the 1RR protocol; and 13.7 min and 15.1 min for the 2RR protocol in healthy volunteers and PH patients, respectively.

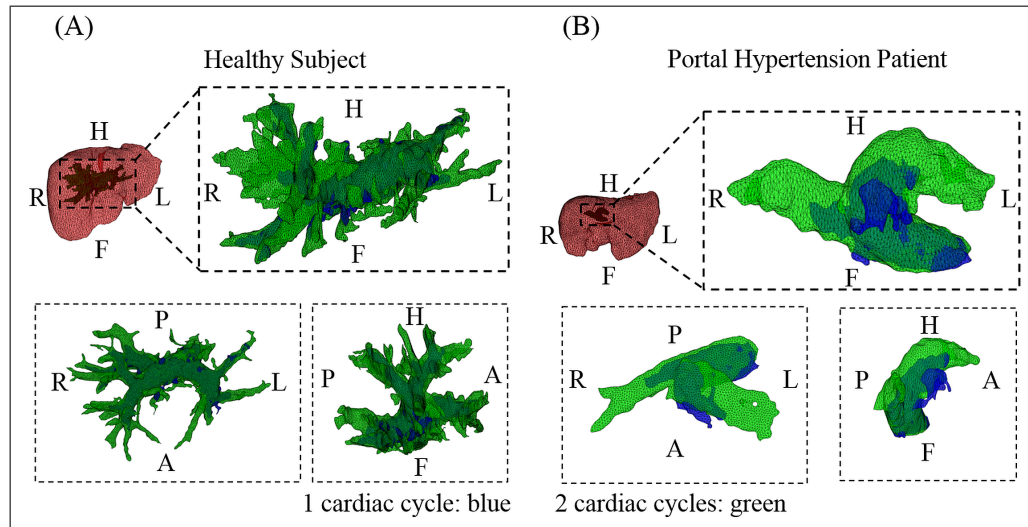


FIGURE 2.7. 3D reconstruction of IHPVBV in one and two cardiac cycles from the TIR-ASL acquisitions. The images show larger IHPVBV in healthy volunteers (A) than PH patients (B) for both protocols. H: head, F: foot, R: right, L: left, A: anterior, P: posterior.

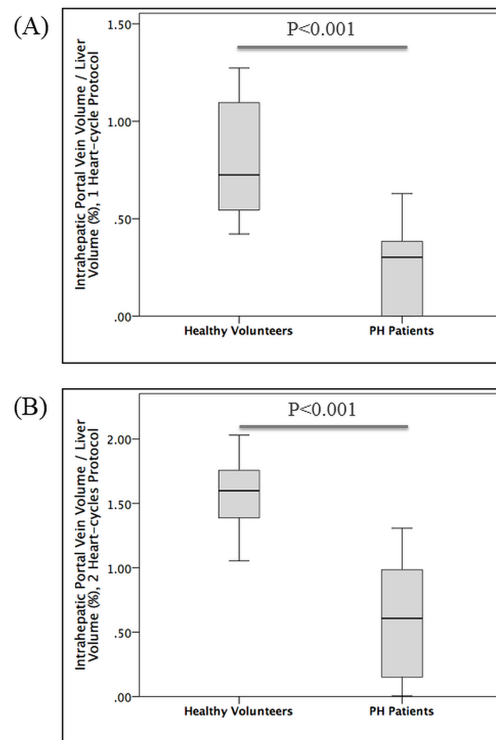


FIGURE 2.8. Healthy volunteers and PH patients median and interquartile (IQ) range for the intrahepatic portal vein volume adjusted by liver volume in (A) one cardiac cycle ($P < 0.001$) and (B) two cardiac cycles ($P < 0.001$).

The ROC analysis demonstrated that the liver-to-spleen volume ratio alone had a sensitivity of 80% and specificity of 90% to differentiate between healthy volunteers and PH patients (AUC:0.90, CI95%:0.77-0.99). Furthermore, the IHPVBV/LV ratio can differentiate between both groups using one cardiac cycle with a sensitivity and specificity of 90% (AUC:0.95, CI95%:0.86-1.00). For the two cardiac cycles acquisition, the sensitivity and specificity of the IHPVBV/LV ratio were 80% and 100% respectively (AUC:0.97, CI95%:0.91-1.00). The combination of morphological information (LV/SV ratio) and functional information (IHPVBV/LV ratio) can accurately differentiate both groups with sensitivity of 90% and specificity of 100% (Fig. 2.9).

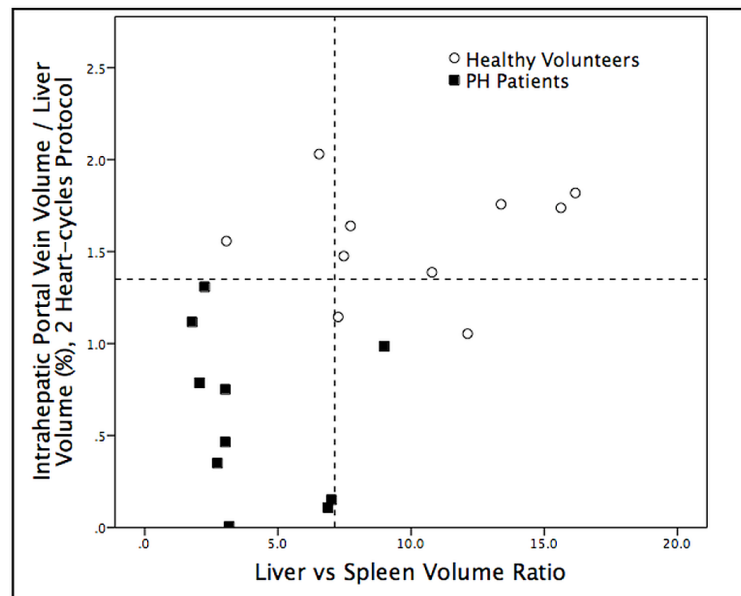


FIGURE 2.9. Intrahepatic portal vein volume adjusted by liver volume measured in the two cardiac cycles protocol and liver-to-spleen volume ratio for healthy volunteer and PH patients. The combination of both parameters identified the PH patients with a sensitivity of 90% and specificity of 100%.

2.5. Discussion

PH is a common complication of chronic liver disease and usually its diagnosis follows its main complications: gastrointestinal bleeding, ascites, and hepatic encephalopathy among others (Bosch et al., 2009)(Andia & Botnar, 2012). The gold standard method for PH diagnosis is an invasive catheterization of the portal vein, which has several limitations to be routinely used in this group of patients. Based in the concept that the portal vein is a low-pressure system, an increase of liver resistance directly affects the volume of portal vein blood that flows into the intrahepatic

space. The feasibility of studying the liver resistance through the quantification of the portal vein blood volume that flows into the intrahepatic space during a cardiac cycle was demonstrated in this study. The quantification of this functional parameter showed a significant difference between healthy volunteers and patients with clinical diagnosis of PH. Our results suggest that TIR-ASL based measurement of functional parameters of the liver could improve the diagnosis of PH, and due to its non-invasive approach, this technique could be used to evaluate the disease progression. The proposed technique does not require the use of intravenous contrast agent; it is insensitive to B_0 inhomogeneities and quantifies only the portal vein blood that flows into the intrahepatic space, avoiding the quantification of blood that could flow through porto-systemic shunts (Bosch & Garcia-Pagan, 2000). Additionally, TIR-ASL technique just needs the acquisition of one image and does not need the subtraction step required by classical ASL methods, therefore the scan acquisition is shorter, signal to noise ratio is higher, and is less sensitive to patient motion (Andia & Botnar, 2012). In this study two TIR-ASL protocols were tested, adapting the sequence for one or two cardiac cycles allowing longer labeling-delays, which is useful to imaging the venous system in CLD patients. As expected, the IHPVBV is larger in the two cardiac cycles protocol, and healthy volunteers had larger IHPVBV than PH patients. The two-cardiac cycle protocol almost doubles the scan time compared to the one cardiac cycle protocol, and the IHPVBV/LV ratio estimated from both protocols showed statistically significant differences between PH patients and healthy volunteers. This result suggests that in a future clinical translation, the one cardiac cycle protocol would be the optimal choice. The main limitation of this work is that all recruited patients have been diagnosed of PH based on their clinical complications, and in none of them an invasive measurement of the actual portal pressure gradient was available. Although the recruited patients had complication only attributable to PH, future studies that correlate the IHPVBV with the invasive portal pressure gradient are needed to further validate the proposed technique.

2.6. Conclusion

The proposed technique allows to improve the non-invasive diagnosis of portal hypertension using morphological quantification and indirect estimations of the liver vascular resistance. This technique has the advantage of not requiring either invasive methods or intravascular contrast agent.

2.7. Acknowledgements:

FONDECYT 1130379 (Chile), SENESCYT Scholarship for PhD students (Ecuador).

2.8. Future Work:

TIR-ASL is a cartesian technique and depends on a respiratory navigator and a cardiac trigger. This means that according to the respiratory cycle from volunteers, the acquisition could take several minutes. The next step is to test sequenced with no cartesian acquisition but with radial phase encoding. In this way we suspect that we can accelerate the acquisition with the same quality data to apply our quantification algorithm. Another step is characterize the proposed technique validating its precision, reproducibility and accuracy in a larger cohort.

3. SPECTROSCOPY

This chapter explains the developments to reach the second objective, to characterize the hepatic fat in a liver voxel using MRS for establish a reference model from the liver spectra and the relative presence of the principal fatty acids. This methodology also provides a clinical diagnosis of normal, steatosis and steatohepatitis disease based on the fatty acid composition in the liver.

3.1. Abstract

Purpose: To quantify the presence of specific fatty acids (FA) within three liver samples using magnetic resonance spectroscopy (MRS). **Materials and Methods:** Three liver samples were built (healthy CN, steatosis ST and steatohepatitis SH) with previous information of their FA composition using the gold standard gas chromatography (GC). Using a 9.4 T spectrometer a MRS spectra was acquired from each sample and the hydrogen (H) presence in each of the eleven metabolites was quantified. The chemical structure of each FA gives information about the H presence known as protonic matrix A . Using an optimization algorithm we solved the problem $A\vec{x} = \vec{z}$ where \vec{z} is the spectra acquired and \vec{x} is the percentage presence of each FA. The main problem is that A is not invertible and there is not a solution for the inverse problem. **Results:** The minimum errors for the FA composition were: 0.5% for healthy liver, negligible for steatosis and 2.9% for steatohepatitis. This method can predict to which category belongs the liver sample 86% of the times. **Conclusion:** This method can predict to which category belongs the liver sample with high precision. These results imply that knowing FA distribution will give us a new approach to understand the development of certain illnesses, by tracking the percentage change in the presence of FA over time.

Keywords: MRS, fatty acid quantification, liver fat-sample, fatty acid estimation.

3.2. Introduction

Non-alcoholic fatty liver disease (NAFLD) is the most common cause of chronic liver disease in both children and adults, increasingly leading to liver transplantation, hepatocellular carcinoma,

and liver-related failure ((Angulo & Lindor, 2002); (Sass, Chang, & Chopra, 2005); (Cohen, Horton, & Hobbs, 2011)). NAFLD represents a range of liver disorders characterized by hepatic steatosis in the absence of excessive alcohol consumption, viral, or drug-related etiologies ((Angulo & Lindor, 2002); (Sass et al., 2005)). In NAFLD patients there are an imbalance of free fatty acids (FA) import and synthesis; leading to a triglyceride accumulation into the hepatocytes ((Cobbold, Patel, & Taylor-Robinson, 2012)).

NAFLD is the first chain in a cascade of liver damage that could lead to liver inflammation, known as non-alcoholic steatohepatitis (NASH), liver fibrosis, cirrhosis, and Hepatocellular Carcinoma (HCC) ((Cobbold et al., 2012); (Paradis et al., 2009)). Patients with NAFLD might have different clinical evolutions, whereas some of them would evolve into cirrhosis and HCC, some others would remain with chronic NAFLD. Risk factors and early biomarkers that explain or predict these evolutions are still unknown ((Bataller & Brenner, 2005)). One key issue in the NAFLD diagnosis is the differentiation between it and its complications: NASH and cirrhosis ((Tilg & Moschen, 2010)). Recent studies have shown that not only the quantity of liver fat but also the kind of FA stored in the liver triglycerides could help to differentiate between NAFLD, NASH and cirrhosis, and would provide relevant information about the diagnosis and prognosis of the liver disease ((Araya et al., 2004a); (Wang, Cao, Fu, Guo, & Zhang, 2011)). It has been proposed that oxidative stress, ethnicity, and diet could modify the liver FA composition, and those changes could lead to different progression of NAFLD ((Vinaixa et al., 2010); (Bray et al., 2002); (Clarke, Gasperikova, Nelson, Lapillonne, & Heird, 2002); (Larque, Garcia-Ruiz, Perez-Llamas, Zamora, & Gil, 2003); (Delas, Popovic, Petrovic, Delas, & Ivankovic, 2008)).

Currently, FA characterization can be obtained from the liver biopsy samples using destructive gas chromatography (GC). This procedure has limitations: it is invasive, it is subject to sampling errors, and it cannot be used for screening, or for evaluating progression and treatment response ((Ratziu et al., 2005)). Additionally, since GC is a destructive analysis, the liver tissue will not be available for histological analysis which is considered the gold standard for the diagnosis, and therefore the liver triglyceride composition is not routinely measured ((Cohen et al., 2011)). Magnetic Resonance has been used to quantify the total liver fat content using chemical shift-based techniques, with two main approaches: spectroscopy (MRS) and imaging (MRI). Fatty liver quantification using MRS considers water and a few peaks of fat from a voxel sample and quantify the

area under them ((Hamilton et al., 2011)). The MR spectrum obtained from fat samples is characterized by eleven peaks formed by metabolites (Figure 3.1) ((Berglund, Ahlström, & Kullberg, 2012)). The frequency of each metabolite peak is known, within a range, and has been derived by many authors ((Guillen & Ruiz, 2003b); (Yeung et al., 2008); (Hamilton et al., 2011); (Ouwerkerk, Pettigrew, & Gharib, 2012); (Berglund et al., 2012); (Vlahov, 1999b); (Skoch et al., 2006); (Ren, Dimitrov, Sherry, & Malloy, 2008); (Strobel, van den Hoff, & Pietzsch, 2008); (Reeder, Cruite, Hamilton, & Sirlin, 2011b); (Peterson & Mansson, 2013); (Qayyum, 2009)). Four of those eleven peaks belong to the glycerol metabolites (ml , g_{m1} , g_{m2} and g_n) and therefore, FAs are characterized only by the other seven metabolites peaks in the MRS.

The estimation of the FA composition in the sample, starting from the MR spectrum cannot be obtained directly since many different combinations of FA can produce the same percentage of metabolites. However, it is possible to characterize some features of the FAs. For example, it is possible to estimate the FA groups (saturated, monosaturated, polysaturated). Miyake et al. ((Miyake, Yokomizo, & Matsuzaki, 1998a)) developed a technique to estimate the polysaturated and monosaturated FA from an oil sample using the relation between the Area Under the Curve (AUC) from the metabolic peaks acquired at 7T. Guillen et al. ((Guillen & Ruiz, 2003a)) used a similar technique and estimated the saturated, linolenic, linoleic, oleic, acyle, bis-allylic FA at 7T; and Yeung et al. ((Yeung et al., 2008)) used the same approach in 11.7T for bone marrow FA characterization. Hamilton et al. ((Hamilton et al., 2011)) characterized the liver spectrum and found a relationship between the principal peaks and chemical properties of the FA as the carbon chain length, the number of double bounds and the number of double bounds interrupted by methylene, using 3T; this has been also done in an iterative fashion ((Berglund et al., 2012); (Peterson & Mansson, 2013)). Lundbom et al. ((Lundbom et al., 2010)) characterized the olefinic and diallylic methylene fat peaks in human fat tissues with long echo times (135, 200ms) and validated them with GC using a PRESS sequence at a 1.5T MRS.

There is an increasing interest in using MRI techniques to obtain more information about the FA composition of different tissues ((Berglund et al., 2012); (Peterson & Mansson, 2013)). Fatty liver quantification using MRI use the bulk methylene metabolite and water to estimate the Fat Fraction (FF) for each voxel ((Leito et al., 2013)). Some of the methods used to separate water from fat are: two-point Dixon ((Coombs, Szumowski, & Coshov, 1997a)), multipoint

Dixon ((Glover, 1991)), IDEAL ((Reeder et al., 2005b)), MP-IDEAL ((Meisamy et al., 2011a)) and FIRST ((Honorato, Parot, Tejos, Uribe, & Irrazaval, 2011)). However, all of them work only with a limited set of fat metabolites.

All the previous works have provided new methodologies to analyze the characteristics of the FA in tissues, however they do not estimate the FA composition. In this work we propose a new methodology to estimate the relative composition of the FA from a fat sample given the seven principal metabolites of the MR spectrum. This is a classical ill-posed mathematical problem with more unknown variables than equations, and therefore has infinite solutions. We propose the use of an optimization method which uses a priori information to specify a few constraints (taken from expected physiological limits). We studied its sensitivity using simulated MR spectrum, and we demonstrated its feasibility using phantoms that simulate the liver FA composition at three clinical stages: healthy, liver with steatosis and with steatohepatitis.

3.3. Materials and methods

3.3.1. Fatty acid estimation

The objective of this section is to obtain the FA composition of a fat sample using the ^1H spectrum obtained by MRS. The MRS acquisition can be described as the system $A\vec{x} = \vec{z}$, where:

- A is the protonic matrix (Table 3.1) which indicates the presence of protons in each metabolite for each FA ((Hamilton et al., 2011)). Matrix A has n rows, equivalent to the number of FA present in the sample ($n=8$ in this study), and c columns equivalent to the number of metabolites present in the FA ($c=7$ in this study). Four columns are linearly dependent (in Table 3.1 columns 3, 5 and 7; and column 4 divided by two plus column 2, with column 1), so the matrix can be reduced as is shown in Table 3.2. Figure 3.2 shows an example of the protonic distribution for the linoleic FA.
- \vec{z} is a vector containing seven metabolites (Figure 3.1). Each metabolite is measured as the normalized AUC of the spectrum. Each metabolite must be normalized by a certain number of protons. Three of the seven metabolites will always have the same number of protons: $m=3$, $\alpha_c=2$ and $\beta_c=2$, so we can reduce \vec{z} and normalize by these seven protons.
- \vec{x} is the unknown percentage of FA in the sample.

Since the matrix A is singular, A^{-1} is not defined, and therefore, this problem is under-determined with infinite solutions. \vec{x} contains the proportion of FA. Typical values of these proportions showed that three and sometimes four of them are in the range of 20 to 30%. This motivated us to restrict as much as possible the energy of this vector. In other words, for the most present acids, no one should have a proportion excessively higher than the others. This is achieved by minimizing the L2 norm of the proportions, thus finding \vec{x} solving the least square problem:

$$\min_{\vec{x}} \frac{1}{2} \|\vec{x}\|_2^2 \quad (3.1)$$

subject to

$$A\vec{x} = \vec{z} \quad (3.2)$$

with three possible a priori information constraints:

$$\min(\vec{x}) \leq \vec{x} \leq \max(\vec{x}) \text{ Tight} \quad (3.3)$$

$$\min(\vec{x}) - \max(\vec{D}) \leq \vec{x} \leq \max(\vec{x}) + \max(\vec{D}) \text{ Medium} \quad (3.4)$$

$$\min(\vec{x}) - 2\max(\vec{D}) \leq \vec{x} \leq \max(\vec{x}) + 2\max(\vec{D}) \text{ Loose} \quad (3.5)$$

where $\max(\vec{x})$ and $\min(\vec{x})$ are vectors of the same size that \vec{x} with the maximum ($\max(\vec{x})$) and minimum ($\min(\vec{x})$) physiological expected FA concentrations considering all liver conditions: healthy, steatosis and steatohepatitis as has been described previously (Araya et al., 2004a). $\max(\vec{D})$ is the largest standard deviation observed in the liver FA composition considering all liver conditions. To solve these optimization problems, we used the linear least-squares methods implemented in MATLAB (The MathWorks, Natick, MA, USA). We used the three possible constraints in order to test the method stability with different size for the searching space.

These constraints do not guarantee a unique solution but they would be different only in the space of solutions given, i.e. the algorithm will adjust a different \vec{x} value according to \vec{D} .

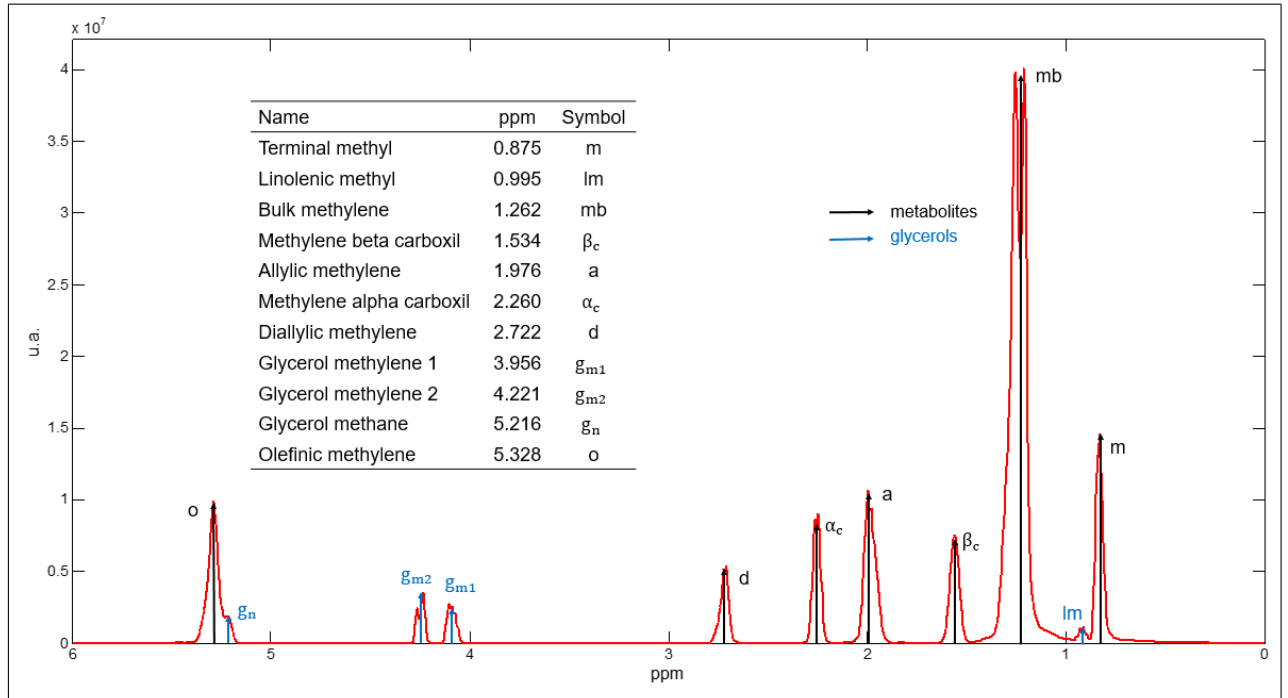


FIGURE 3.1. Example of fat spectrum showing the metabolites at 9.4T. In this work we are not considering the glycerol peaks.

TABLE 3.1. Protonic matrix of the eight FA used in this work. The protonic matrix indicates the number of proton for each metabolite characterized by its spectral frequency in Hz and its chemical shift in ppm.

FA(ppm)	Metabolites						
	5.328	2.722	2.260	1.976	1.534	1.262	0.875
$f_{9.4}$ (Hz)	2122.30	1121.20	880.97	800.88	640.70	520.57	360.40
Myristic (Mi)	0	0	2	0	2	20	3
Myristoleic (MI)	2	0	2	4	2	12	3
Palmitic (Pa)	0	0	2	0	2	24	3
Palmitoleic (PI)	2	0	2	4	2	16	3
Stearic (Es)	0	0	2	0	2	28	3
Oleic (Ol)	2	0	2	4	2	20	3
Linoleic (Li)	4	2	2	4	2	14	3
Linolenic (Ln)	6	4	2	4	2	8	3

TABLE 3.2. Reduced protonic matrix, without linear dependency.

FA	Metabolites reduced			
Myristic (Mi)	0	0	20	7
Myristoleic (Mi)	2	4	12	7
Palmitic (Pa)	0	0	24	7
Palmitoleic (Pl)	2	4	16	7
Stearic (Es)	0	0	28	7
Oleic (Ol)	2	4	20	7
Linoleic (Li)	4	6	14	7
Linolenic (Ln)	6	8	8	7

Metabolite	#	H	TH
o CH=CH	4	1	4
d C=C-CH ₂ -C=C	1	2	2
α_c OC-CH ₂ -CH ₂	1	2	2
a CH ₂ -C=C	2	2	4
β_c OC-CH ₂ -CH ₂	1	2	2
e CH ₂ -	7	2	14
m CH ₃ -	1	3	3

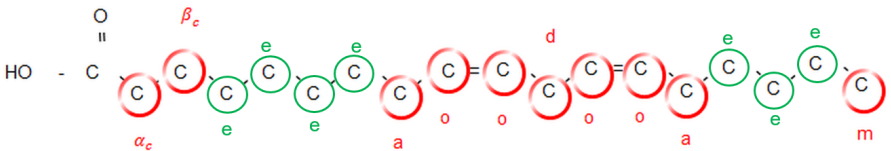


FIGURE 3.2. Protonic distribution of linoleic FA C18:2; H: proton; TH: total protons; O: oxygen; C: carbon; α_c : alpha carboxyl; β_c : beta carboxyl; a: allyl; o: olefinic; d: dyallil; m: methyl; mb: bulk methylene.

3.3.2. Sensitivity Analysis

In order to test the robustness of our algorithm we performed a sensitivity analysis using simulated fat liver spectrum (\vec{z}) with Gaussian noise added to the whole spectrum. We built \vec{z} using the liver FA composition (\vec{x}) reported in the literature for each liver conditions: healthy, with steatosis and with steatohepatitis (Table 3.3). We created the vector \vec{z}_R , which corresponds to vector \vec{z} with added Gaussian noise, after the simulation, using the following formulation:

$$\vec{z}_R = \vec{z} + N(0, ns \cdot \vec{z}) \quad (3.6)$$

where $ns \cdot \vec{z}$ is the standard deviation of the normal distribution of the noise, with ns ranging between 0 and 10%. We estimated the FA composition (\vec{x}_R) from \vec{z}_R by solving the optimization problem for each liver sample, and for each ns value, and repeating it ten thousand times. We calculated the mean and standard deviation of \vec{x}_R for each ns . We calculated the Euclidean distance between \vec{x}_R and the simulated data (\vec{x}) in order to evaluate the robustness of the proposed method. In these simulations we used eight FA (Table 3.3) that represent 83% of the FA present in a healthy human liver, and 96% of the FA present in a NAFLD and NASH human liver.

3.3.3. Phantom validation

In order to validate our methodology we built three physical phantoms with the same FA composition that were found in human liver: healthy, with steatosis, and with steatohepatitis (Table 3.3). Each phantom weighted 500mg in a final volume of 8ml of deuterated chloroform (CDCl_3) to dissolve the FA. Table 3.4 shows the lower and upper bound limits for each FA used to constrain the optimization. These bounds are measured in g/100g FA and was found in literature (Araya et al., 2004a).

TABLE 3.3. Weights (g/100g FA), standard deviation in grams (D) from FA found by Araya at al. 2004, and weights used for the simulated and physical phantom (mg/100mg FA) of the FA used present in the liver in three conditions: healthy, steatosis, and steatohepatitis normalized for the eight FA used.

FA	Healthy			Steatosis			Steatohepatitis		
	g	D	mg	g	D	mg	g	D	mg
Mi (C14:0)	23.14	1.07	115.697	7.51	0.73	37.551	9.53	0.52	47.480
Ml (C14:1)	1.12	0.17	5.606	2.17	0.22	10.848	2.33	0.21	11.583
Pa (C16:0)	21.00	0.48	104.962	35.15	2.09	175.759	34.43	1.77	171.658
Pl (C16:1)	3.25	0.18	16.281	5.61	0.59	28.059	4.92	0.44	24.575
Es (C18:0)	0.11	0.06	0.593	0.66	0.49	3.286	0.64	0.29	3.183
Ol (C18:1)	30.18	0.95	150.883	34.11	1.46	170.543	30.87	2.09	153.918
Li (C18:2)	20.76	1.07	103.769	14.39	1.46	71.972	16.95	1.57	84.525
Ln (C18:3)	0.44	0.10	2.207	0.40	0.04	1.982	0.32	0.06	3.078
TOTAL	100.00		500.000	100.00		500.000	100.00		500.00

The ^1H NMR spectra were obtained in a Bruker Avance spectrometer operating at 9.4 T with a free induction decay (FID) acquisition called Zg30 (30 degrees in z axis). We took 70 μl from each phantom of 8 ml to introduce in the spectrometer. CDCl_3 has a small proportion of tetramethylsilane as an internal reference; this mixture was introduced into a 5 mm diameter tube. The acquisition parameters were: spectral width 8012.820 Hz, relaxation delay 1 s, number of scans 16, acquisition time 2.045 s, flip angle 30 to avoid T1 relaxation effects and total acquisition time 48.72 s (number of scans \times (time between pulses + acquisition time)). The experiment was carried out at 25 $^\circ\text{C}$.

TABLE 3.4. FA physiological composition constrains in g/100g FA used in the optimization algorithm for the three constrains (LB: lower bound, UB: upper bound).

FA	Tight		Medium		Loose	
	LB	UB	LB	UB	LB	UB
Mi	7.51	23.14	6.61	24.04	5.71	24.93
MI	1.12	2.32	0.91	2.53	0.70	2.74
Pa	20.99	35.15	18.99	37.15	16.99	39.15
PI	3.26	5.61	2.69	6.18	2.12	6.75
Es	0.12	0.66	0.00	1.13	0.00	1.60
Ol	30.18	34.11	28.18	36.11	26.18	38.11
Li	14.39	20.75	12.89	22.25	11.39	13.75
Ln	0.40	0.62	0.32	0.70	0.24	0.78

From the FID time curve we obtained a complex signal in the Fourier domain. We corrected its phase using zero (α) and first order (β) corrections ((Keeler, 2010)), such that the corrected signal (\vec{S}_c) is:

$$\vec{S}_c = \vec{S} e^{iu\beta} e^{i\alpha} \quad (3.7)$$

where \vec{S} is the acquired spectral signal and u is the frequency in the Fourier domain. Finally, the frequency axis was shifted using as a reference the highest peak corresponding to the methylene metabolite at 1,262 ppm. We used an in-house program written in MATLAB to correct and quantify the spectrum from the FID time curves. We calculated the normalized AUC for

each metabolite for each of the three liver phantoms: healthy, steatosis and steatohepatitis, and we applied our methodology to estimate the FA composition using \vec{S}_c .

3.3.4. Sample Labeling

Ultimately, the objective is to provide a clinical diagnosis of the liver conditions, similar to the one obtained from a liver biopsy procedure, using the FA composition estimated by our methodology. In order to test the accuracy of our methodology to provide a diagnosis of normal, steatosis or steatohepatitis, we simulated different “livers” with random FA composition using the limits showed in Figure 3.3. With this composition we simulate the MR spectrum and we applied our method in order to test its sensitivity and specificity in order to provide a correct clinical diagnosis. The simulate FA composition (\vec{x}_G) was:

$$\vec{x}_G \sim N(\vec{x}, \vec{D}) \quad (3.8)$$

Where \vec{x} is the mean and \vec{D} the standard deviation for each FA taken from the literature. We calculated the respective MR spectrum for each \vec{x}_G using the formulation: $\vec{z}_G = A\vec{x}_G$; and we added Gaussian noise as follows:

$$\vec{z}_{RG} = \vec{z}_G + N(0, np \cdot \vec{z}_G) \quad (3.9)$$

where np values are 0 to 5 % of the mean value of the \vec{z}_G signals.

Finally we used \vec{z}_{RG} as the input to our optimization method to estimate the FA composition (\vec{x}_{Est}). We categorized it as healthy, with steatosis or with steatohepatitis by choosing the minimum Euclidian distance to the FA composition of the three expected liver conditions: \vec{x}_{CN} (control), \vec{x}_{ST} (steatosis) and \vec{x}_{SH} (steatohepatitis) (Table 3.3):

$$d_{CN} = \|\vec{x}_{Est} - \vec{x}_{CN}\|_2^2 \quad (3.10)$$

$$d_{ST} = \|\vec{x}_{Est} - \vec{x}_{ST}\|_2^2 \quad (3.11)$$

$$d_{SH} = \|\vec{x}_{Est} - \vec{x}_{SH}\|_2^2 \quad (3.12)$$

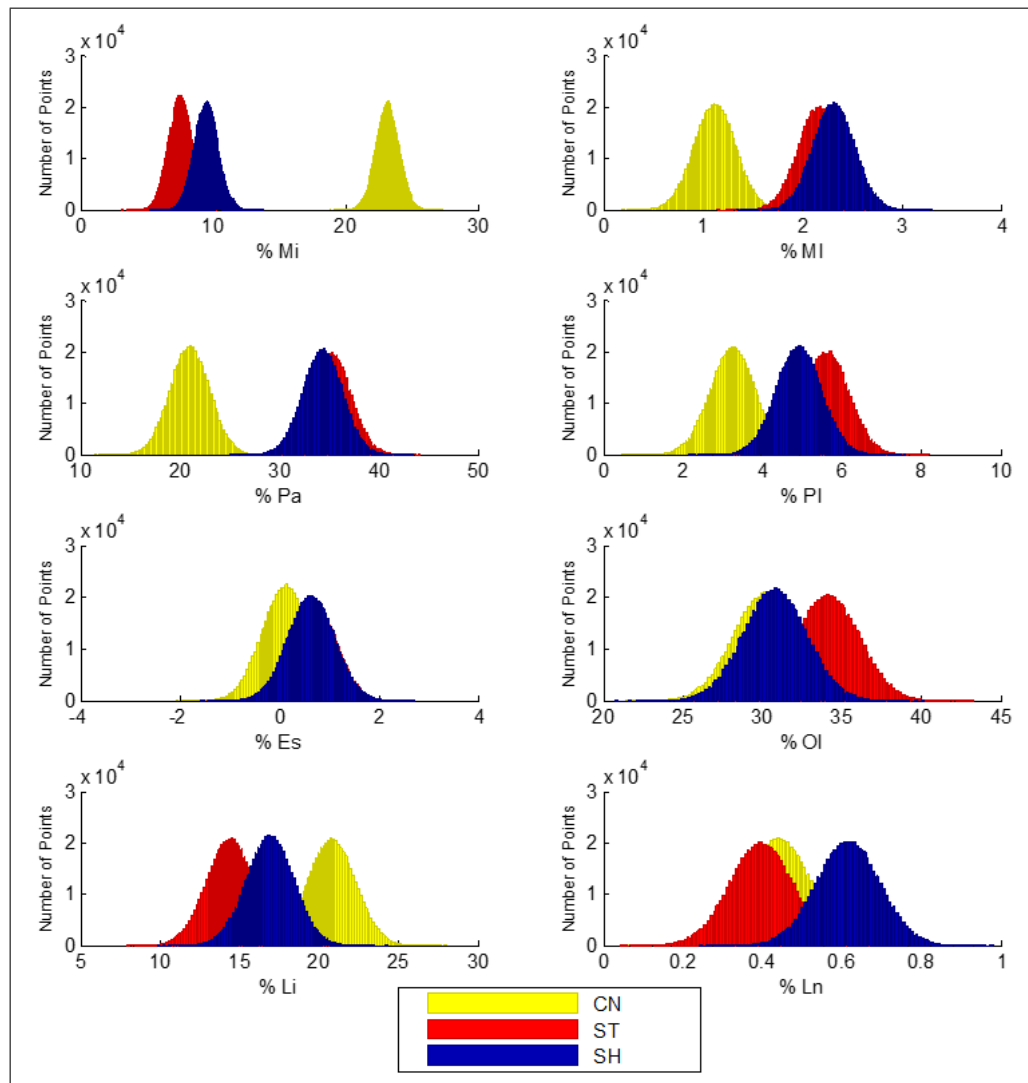


FIGURE 3.3. FA concentration distribution in the three liver stages: healthy (CN), steatosis (ST) and steatohepatitis (SH). Mi: myristic, MI: myristoleic, Pa: palmitic, PI: palmitoleic, Es: stearic, OL: oleic, Li: linoleic, Ln: linolenic.

Finally, we estimated the sensitivity and specificity of our methodology to differentiate between normal (CN) and diseased liver (ST+SH); and to differentiate between steatosis and steatohepatitis plus inflammation (ST versus SH).

3.4. Results

We successfully obtained the MRS spectrum at 9.4 T of the three liver phantoms that resemble healthy tissue (CN), with steatosis (ST) and with steatohepatitis (SH). The estimated AUC of

the 7 metabolites are shown in Figure 3.4. All the metabolites for each of the 3 phantoms were normalized.

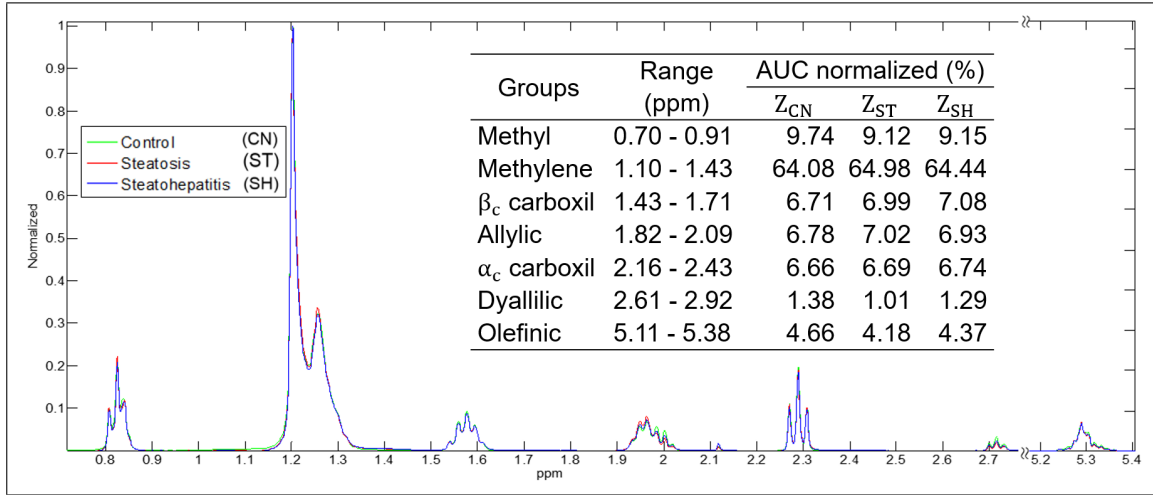


FIGURE 3.4. MR spectrum of the three liver phantoms acquired at 9.4 T and the AUC calculated for each metabolite. Note that the spectra are quite similar but they have little differences. The differences can be seen in AUC from control (Z_{CN}), steatosis (Z_{ST}) and steatohepatitis (Z_{SH}) spectra.

The distance between the FA composition estimated from the simulated data and from the acquired phantoms spectrum are shown in Figure 3.5A and 3.5B, respectively, for the three established optimization constrains. The errors for the FA composition were found for the optimization methodology that used the tight constraint and the values were: 0.5 % for healthy liver, negligible for steatosis and 2.9 % for steatohepatitis. In the case of the acquired data, the errors were 7.2 %, 12.6 % and 15.7 %, for the healthy liver, steatosis and steatohepatitis respectively. There is a growing trend of the error in the simulated data, which is harder to see in the acquired data. These difference errors might be for the arbitrary separation limits between metabolites (Figure 3.4), especially between methylene (1.262 ppm) and beta carboxyl (1.534 ppm).

Table 3.5 and Figure 3.6 show the estimated x for the acquired z , actual percentage and absolute error for FA in each phantom for the tight constraint. The lowest absolute error of estimation was 0.12 % for the stearic FA in the healthy liver phantom; 0.40 % for the linolenic FA in the phantom with steatosis; and 0.62 % for the linolenic FA in the phantom with steatohepatitis. The highest absolute error of estimation was 6.05 % for the linoleic FA in the healthy liver phantom; 8.03 % for the palmitic FA in the phantom with steatosis; and 9.20 % for the palmitic FA in the

phantom with steatohepatitis. Bland-Altman analysis is showed in Figure 3.7 reporting there is no dependency with the media.

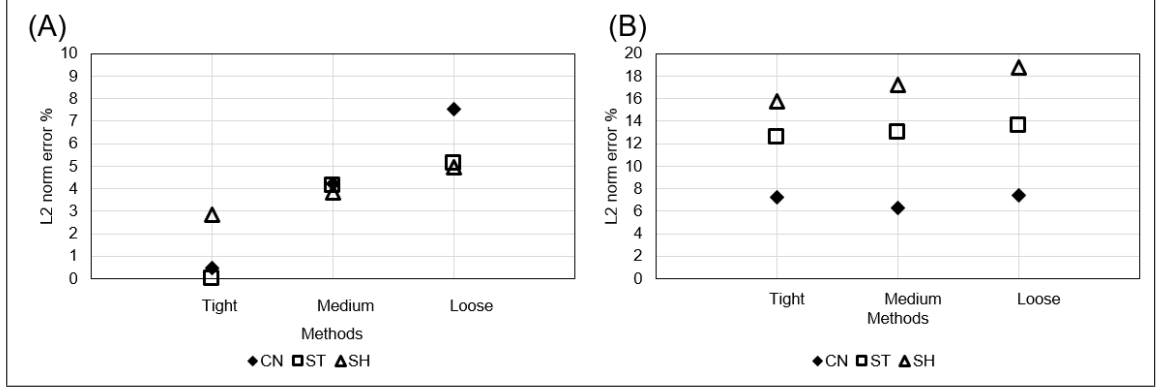


FIGURE 3.5. L2 norm of the error between the actual FA composition and the estimated by the proposed methodology for the simulated spectrum (A) and for the acquired liver spectrum (B).

TABLE 3.5. FA composition estimated by the optimization method (x_{Est}) compared with Table 3.3 data in the three fat liver phantoms: healthy (x_{CN}), with steatosis (x_{ST}), and with steatohepatitis (x_{SH}). $|E_{Abs}|$ is the absolute value of the FA estimation error.

FA	x_{CN}	x_{Est}	$ E_{Abs} $	x_{ST}	x_{Est}	$ E_{Abs} $	x_{SH}	x_{Est}	$ E_{Abs} $
Mi	23.14	23.91	0.77	7.51	14.05	6.54	9.50	18.49	8.99
MI	1.12	3.09	1.97	2.17	5.62	3.45	2.32	4.71	2.39
Pa	20.99	23.65	2.66	35.15	27.12	8.03	34.33	25.13	9.20
PI	3.26	4.52	1.26	5.61	8.65	3.04	4.91	8.01	3.10
Es	0.12	0.00	0.12	0.66	0.00	0.66	0.64	0.00	0.64
Ol	30.18	29.41	0.77	34.11	36.68	2.57	30.78	35.94	5.16
Li	20.75	14.70	6.05	14.39	11.06	3.33	16.90	12.00	4.90
Ln	0.44	1.39	0.95	0.40	0.00	0.40	0.62	0.00	0.62

Figure 3.8 shows the relation between the Gaussian noise added to the simulated MR spectrum (\vec{z}) and the L2 norm of the error between the simulated and the actual values of \vec{x} from Table 3.3. Gaussian noise yields an homogeneous distribution of the error for the three liver samples.

The distributions of the difference between the estimated FA composition (\vec{x}_{Est}) and the simulated FA composition (\vec{x}) for three ns values are shown in Figure 3.9, as an example for the myristic FA. When ns is equal to 5 % there is a higher bin in the edge that means this constraint was activated, this effect is higher when ns is 10 %.

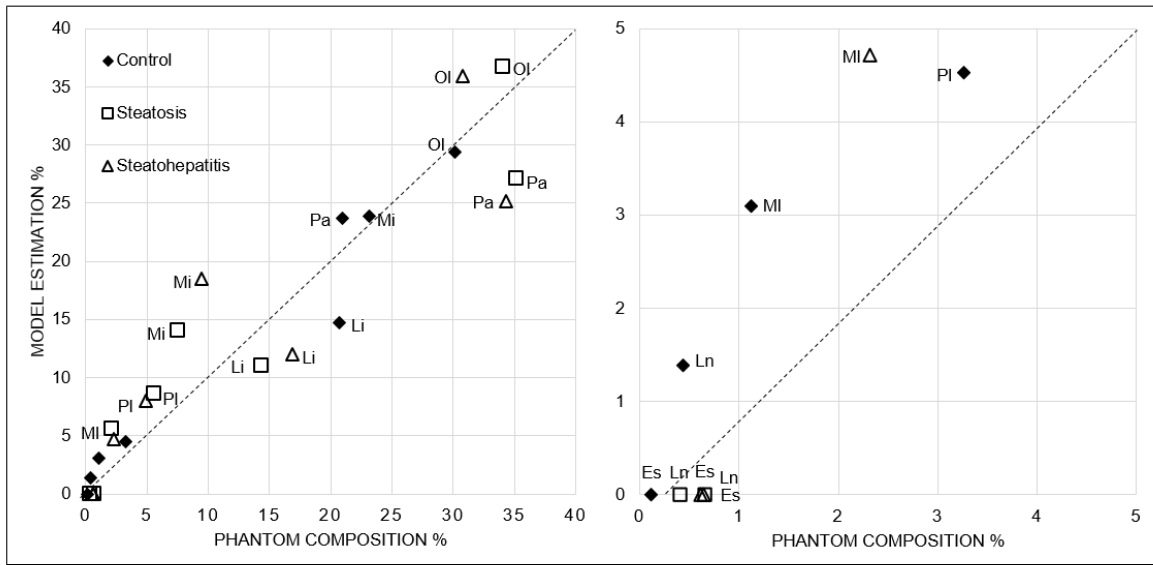


FIGURE 3.6. Relation between the actual FA composition in each phantom and the estimated composition using the proposed method.

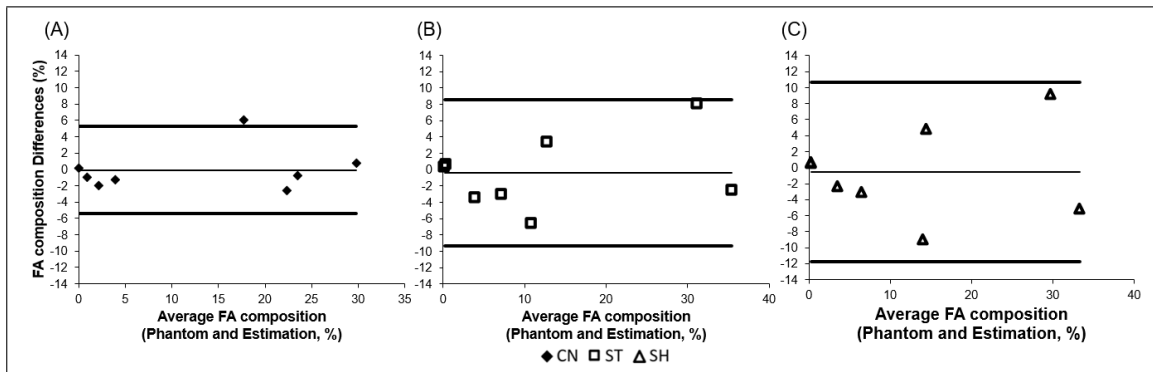


FIGURE 3.7. Bland-Altman plot for the differences between the estimated and the literature data from the three liver phantoms: (A) healthy, (B) with steatosis and (C) with steatohepatitis.

Table 3.6 and Figure 3.10 show the sensitivity and specificity of the proposed methodology for differentiating normal from diseased liver, and between steatosis without (ST) and with (SH) inflammation according with the level of added Gaussian noise (np) and the three constraints used in the optimization method. Maximum sensitivity and specificity are reached when no noise is added. When 1 % of Gaussian noise is added to the simulated MR spectrum the method has a sensitivity around 94 % and a specificity around 79 % to differentiate between healthy and diseased livers, and around 68 % and 77 % to differentiate between NAFLD and NASH.

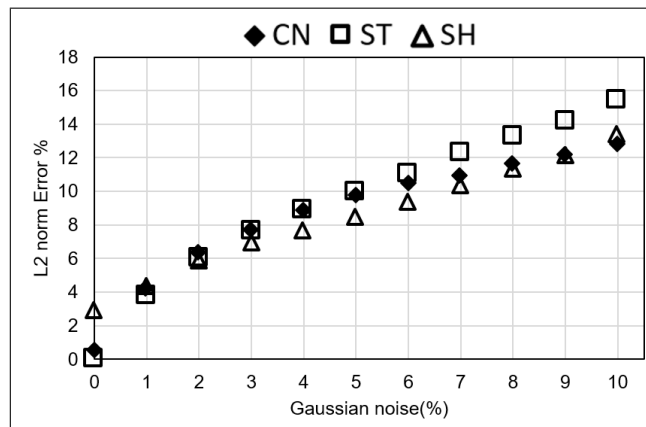


FIGURE 3.8. Relation between the magnitude of the Gaussian error added to the simulated MR spectrum (\vec{z}) and the L2 norm of the error between the simulated and the actual values of \vec{x} for the 3 clinical conditions normal (CN), steatosis (ST) and steatohepatitis (SH).

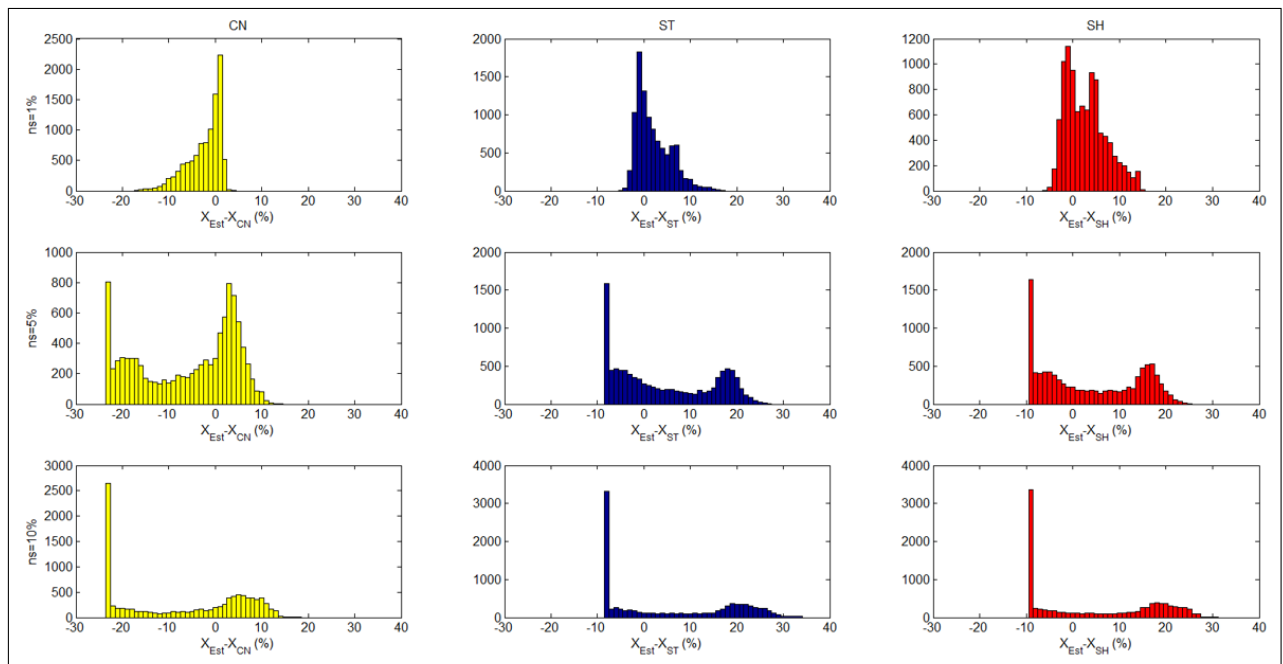


FIGURE 3.9. Distribution of the difference between the estimated FA composition (\vec{x}_{Est}) and the simulated FA composition (\vec{x}) from Table 3.3 for myristic FA. In the rows are the Gaussian error added (ns) and in the columns the liver samples: healthy (CN), with steatosis (ST) and with steatohepatitis (SH).

3.5. Conclusion

The FA composition of a fat sample cannot be directly obtained from the MR spectrum due to the protonic matrix is not invertible, and the problem has infinite solutions. In this work we demonstrated that it is possible to find an approximation of the FA compositions using an optimization

TABLE 3.6. Percentage of precision for classification in three liver groups using the three constrains. Sens: sensitivity; Spec: specificity; np : percentage Gaussian added noise

Healthy and Diseased Liver						
$np(\%)$	Tight		Medium		Loose	
	Sens	Spec	Sens	Spec	Sens	Spec
0	100.00	100.00	100.00	100.00	100.00	100.00
1	95.79	78.68	94.03	80.27	93.73	79.02
2	89.17	51.21	89.11	52.50	88.09	51.01
3	86.20	41.98	84.85	42.54	85.54	40.87
4	83.24	38.75	83.42	38.00	83.60	37.98
5	81.68	34.52	81.92	34.85	82.17	35.76
Without and With Inflammation						
$np(\%)$	Tight		Medium		Loose	
	Sens	Spec	Sens	Spec	Sens	Spec
0	99.92	100.00	97.17	100.00	85.58	100.00
1	69.49	77.23	69.93	77.01	67.61	77.70
2	59.78	63.52	60.50	63.60	61.24	63.07
3	56.38	57.71	56.16	59.05	57.45	57.42
4	55.38	57.13	55.06	56.15	54.70	57.01
5	53.53	55.67	53.41	55.58	54.47	54.94

algorithm with a priori information. The a priori information needed is: (1) know the number and type FA present in the sample, and (2) know their expected minimum and maximum concentration in the analyzed tissue. The first constraint is very important, because the MR spectrum is built by the superposition of peaks that could come from a wide source of FA. The second constraint is less strict, and we proved that our method is stable even when the searching space for each FA is wide.

We also demonstrated that our methodology is able to categorize a simulated liver fat MR spectrum as healthy, with steatosis or with steatohepatitis with a sensitivity ranging from 86 to 100 % and a specificity of 100 % in a spectrum without noise.

The present work was made using a fat phantom and a 9.4T MR Spectrometer in order to have the best spectrum with high resolution, in order to obtain a proof of concept result. The

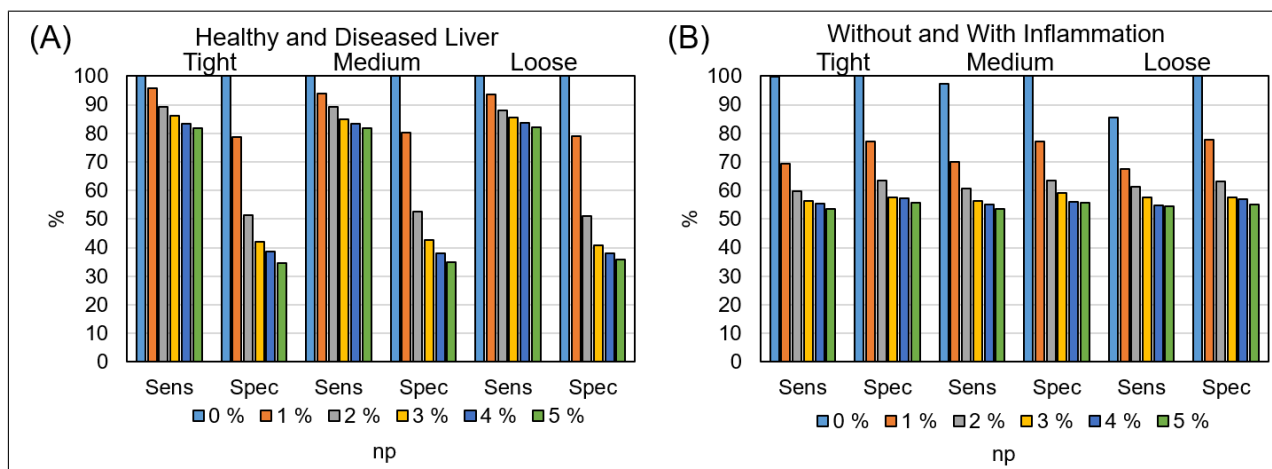


FIGURE 3.10. Sensitivity and specificity of the proposed method to differentiate between normal and diseased liver (A) and between ST and SH (B) form simulated spectrum with five different magnitude of added Gaussian noise (np). Sens: sensitivity; Spec: specificity.

sensitivity analysis showed that our algorithm is sensitive to noise; therefore, the quality of the MR spectrum is critical in order to obtain reliable results. Future works are now needed to validate our results in biological tissues and using clinical magnetic fields (1.5 or 3.0 T) in order to translate the methodology to clinical applications.

Finally, in this work we focused our methodology in the liver analysis, but it would be possible to apply our proposed algorithm in other areas where the FA estimation would be useful like edible oil research (Dais & Hatzakis, 2013), biodiesel production (Chisti, 2007) and other bulk products (Breuer et al., 2013).

3.6. Acknowledgements:

Funding grant: FONDECYT 1130379 and 1141201.

Daniel Aguirre was funded by a scholarship from the Superior Educational National Secretary in Science and Technology (SENESCYT) from the Government of Ecuador, and also by a scholarship from the National Commission for Scientific Technological Research CONICYT-PCHA/Doctorado Nacional/2015-21150021 from the Government of Chile.

Flavia Zacconi. wish to express appreciation for the support to Centro de Investigación en Nanotecnología y Materiales Avanzados "CIEN-UC", Pontificia Universidad Católica de Chile, Santiago, Chile.

3.7. Future Work:

The next step of this study is replicate our results in biological tissues at 9.4 T, and optimize our methods to be used at 3.0 T and 1.5 T.

4. METABOLIC IMAGES

This chapter explains the work to achieve the final objective of this thesis: to extend the method developed in chapter 3 in order to obtain images from the fatty acids (FA) distribution in tissue. We developed a proof-of-concept experiment using a digital phantom. In this chapter we explain the formulation and the future approach to solve this problem using liver clinical images.

4.1. Abstract

Purpose: To quantify the presence of specific fatty acids (FA) from multi-echo images. As a proof of concept we test an optimization method using a digital phantom that simulates edible oils and field inhomogeneities. **Materials and Methods:** Four oil samples (sunflower, corn, olive and soybean) were tested using Gas-Chromatography (GC) to identify their FA composition in percentages (\vec{x}). In this work we only considered FA limited by the number of carbons (CL) in its chain, and the number of double bounds (ndb), in other words, we work with FA from C16:0 until C18:3. The identified FA were used as prior information in the optimization model. Each FA identified in the GC has a chemical structure that defines the number of hydrogen (H) in each metabolite, creating the protonic matrix (A). Using $\vec{z} = A\vec{x}$, it was possible to calculate the metabolite presence (\vec{z}). We used this information to create a digital image phantom of the four oil samples. We also simulated pure water and we added linear magnetic field inhomogeneities, assuming a main field of 1.5T. We solved the inverse problem using an optimization algorithm to find the metabolite presence in each pixel. We consider eight metabolites: water and seven principal fat metabolites (not considering glycerols). Knowing this metabolic presence we used a second optimization algorithm (presented in chapter 3) to obtain an image of each FA. **Results:** From the first optimization algorithm we found the metabolite presence for the four oils and water, and for different field inhomogeneities. For an inhomogeneity field varying from -30 to 30 Hz the minimum error found was 0.026% for the water metabolite in 4.860 ppm for soybean oil. The maximum error found was 5.41% for the methylene β carboxil metabolite in 1.534 ppm for the olive oil. From the second estimation algorithm we estimated the FA percentage presence from the metabolites previously found. The minimum error was negligible for the palmitoleic FA for the corn oil. The maximum error was 13.64% for linoleic FA for the olive oil. **Conclusion:** We present

a proof of concept method to estimate the FA presence in a simulated digital image phantom, using an optimization algorithm.

Keywords: MRS, fatty acid quantification, liver fat-sample, fatty acid estimation, metabolic images.

4.2. Introduction

Fatty liver disease is characterized by excessive and abnormal fat accumulation in liver cells. Currently, the most common way to evaluate the amount of liver fat is through a biopsy. Its main problem is to be invasive sampling and monitoring problems, and therefore not a suitable diagnostic method (Kumar V. et al., 2005). Fatty liver disease is evaluated in hepatocytes using a visual scale estimation of 0 to 3, proportional to intracellular fat (Brunt et al., 1999).

Fatty liver causes excessively fat accumulation in hepatocytes. This accumulation can reach a state of cirrhosis, implying the existence of portal hypertension and liver resistance. This resistance is produced by a state of fibrosis caused by hepatocytes secreting collagen as a defense against toxins. The two techniques used in magnetic resonance to measure the fat signal are: magnetic resonance imaging (MRI) and magnetic resonance spectroscopy (MRS). MRI is a technique of non-invasive acquisition of high resolution images that does not depend on the skill of the operator, such as ultrasound, and the acquired signal can be decomposed in different chemical species such as water metabolite and the higher fat peak from the fat spectra. Also it does not use ionizing radiation such as the X-ray computed tomography (Fazel et al., 2009). MRI methods allow to measure the fat fraction signal (FF), defined as the fraction of the acquired signal attributed to the actual fat in the liver. This signal can be altered by various technical factors such as: variation in relaxation times T1 (C.-Y. Liu et al., 2007), T1 effects and noise bias (Bydder, Yokoo, et al., 2008), magnetic field inhomogeneities or T2* (Yu et al., 2007), the fat spectral complexity (Yu et al., 2008), J coupling or the intrinsic behavior from the fat spectra peaks (Hamilton et al., 2009), and Eddy currents or altered phase information (Lu et al., 2008). These factors can produce unreliable results of the lipid content. The most advanced techniques in MRI measures proton density fat fraction (PDFF), which is a fundamental property of tissue defined as the fraction of protons attributed to liver fat and a direct measure of the amount of fat in the liver (Reeder, Hu, & Sirlin, 2012).

MRS is the most straightforward method to separate the signal obtained from the liver into its components of water and fat. Spectra collection requires acquisition technique typically evaluated in a volumetric element or voxel with a size from 8 to 27 cm³. The fat liver spectrum is different from adipose tissue and water-fat emulsion, suggesting different spectral differences in fat deposits in the body (Hamilton et al., 2011). Regardless of the method, a radiofrequency pulse is always applied in the presence of a gradient. For this reason, there is often a difference of the spatial distribution due to the chemical shift in the image domain. This differences of the spatial distribution can be measured. (Reeder et al., 2011b).

The fat is characterized by a spectrum with eleven metabolites identified. A FA is composed by seven of the eleven metabolites (glycerols not included) and have different resonant frequencies. Currently, some of the methods used for water and fat separation, mainly work with the bulk methylene metabolite information, located at 1.262 ppm, compared to 4.680 ppm for water (Hamilton et al., 2011) but, there are other methods that use until six peaks information (Wang, Hernando, & Reeder, 2015). There are other methods that consider certain problems caused by the relaxation time, noise, field inhomogeneity and the fat spectral complexity considering four of these seven major metabolites (Yu et al., 2008). It is difficult to establish the presence of the seven metabolites on a 1.5T clinical scanner due to its low resolution. This metabolite presence is possible to do with 9.4T spectrometer. The disadvantage is the sample size (70 μ l) which correspond to a biopsy sample. The goal is to understand the spectral signal of fat in the spectrometer to be brought to a clinical 1.5T or 3.0T clinical scanner.

The acquisition techniques of MRI used to measure fat are two: fat suppression and chemical shift. The fat suppression technique separates the fat and water signal by comparing the magnitudes of the acquired images with and without fat saturation, and does not measure the PDFF (Yokoo et al., 2011). The chemical shift technique to separate fat and water acquires the signal with different echo times, using magnitude information or complex information to measure the PDFF. The complex mode uses the magnitude and phase from three images acquired in six echo times to deliver a response in a dynamic range of 0 to 100 %; the magnitude mode uses only the magnitude of three images acquired at different echo times where two are out of phase and one is in phase. Its main drawback is that it cannot quantify it precisely out of a dynamic range between 0 to 50 % (Reeder et al., 2011b).

PDFF is a biomarker that measure accurately the amount of fat in the liver (Reeder et al., 2012). The principal difference between the PDFF and the FF, (Reeder S. B., Hines C. D., Yu H., McKenzie C. A., & Brittain J. H., 2009), is that FF is the direct measure of the independent fat tissue relative signal sensitivity of the radiofrequency coils, while PDFF is defined in the same way, with prior correction for T1 (Bydder, Yokoo, et al., 2008), T2* (Yu et al., 2007) and the multispectral fat distribution (Yu et al., 2008).

PDFF is the result of the study of some techniques to separate water and fat. One of the main technique used to separate fat and water images is Dixon which acquire two images: the first one in phase and the second one out of phase, just changing the echo time value (Coombs et al., 1997a). The magnetic field variation can be calculated using the phase information obtained in each acquisition. Equation 4.1 shows the pixel intensity value (I_0) in image domain where there is superimposed the correspondent water-fat information:

$$I_0 = (W \cdot e^{i2\pi \cdot f_w \cdot TE_0} + F \cdot e^{i2\pi \cdot f_f \cdot TE_0}) e^{i2\pi \cdot \Delta B \cdot TE_0} \quad (4.1)$$

where W and F correspond to water and fat quantity factor in the pixel, respectively; f_w and f_f are the water-fat resonance frequency values of -300 Hz and -76 Hz, respectively (at 1.5T); TE_0 is echo time, and ΔB is the magnetic field variation in Hz.

An extension to this technique allows for more than one species, working in the image domain is the iteratively squares estimation method or IDEAL (Reeder et al., 2005b). Its main advantage is that it can separate multiple chemical species depending on the number of images acquired. The model of the acquired signal is specified in Equation 4.2 and estimate the intensity of each chemical specie ρ_j .

$$s(t) = \left(\sum_{j=0}^M \rho_j e^{i2\pi \cdot \Delta f_j \cdot t} \right) e^{i2\pi \cdot \psi \cdot B \cdot t} \quad (4.2)$$

where s is the acquired signal in an image that contain M species, each of them with a chemical displacement (Hz) $\Delta f_j (j = 1 \dots M)$ acquired at an echo time t , ρ_j is the intensity of each specie as a complex number. In addition ψ is the local magnetic shift or the magnetic field variation (Hz). In order to find ρ_j is necessary make $2M + 1$ acquisitions (Reeder et al., 2004). It is also possible

to correct for T2* with T2*-IDEAL (Yu et al., 2007), and a modeling of fat multi spectrum called MP-IDEAL (Yu et al., 2008) .

Another image separation technique that considers field inhomogeneity, R2*, and species estimation using a variable time map (FIRST) (Honorato et al., 2011). Unlike the previous methods, FIRST works in the Fourier domain taking into consideration the phase accumulation due to field inhomogeneities and the signal decay during acquisition, correcting the artifacts caused by chemical shift and field inhomogeneity. The purpose is to adjust the unknown variables of the model to the acquired signal values. Equation 4.3, shows the acquired signal $S_m(t)$ for specie m at an specific time t . The functional reconstruction is showed on Equation 4.4.

$$S_m(t) = \sum_{j=0} \rho_{m,r} e^{-i2\pi(\Delta f_m + \psi_r) \cdot t} e^{-i2\pi \cdot r \cdot k_t} \quad (4.3)$$

$$\min_{\substack{\rho_m \in C^N \\ \tilde{\psi} \in C^N}} \left\| S(t) - \sum_{m=1}^M \sum_r \rho_{m,r} \cdot e^{-i2\pi(\Delta f_m + \tilde{\psi}_r) \cdot t} \cdot e^{-i2\pi \cdot r \cdot k_t} \right\|_2 \quad (4.4)$$

where $\rho(m, r)$ is the pixel complex intensity from the specie m in a discrete position r , t represents the acquisition time, $\tilde{\psi}_r$ is the field map, k_t is the acquired k space at t time, and $\tilde{\psi}_r = \psi_r + iR_2^*(r)/2\pi$. This functional minimization gives $\rho_m(x)$, $\psi(x)$ and $R_2^*(x)$, and it requires $2M + 2$ acquisitions.

These two methods, IDEAL and FIRST, have differences with respect of the geometric position of the reconstructed signals, but they only consider one metabolite for fat in bulk methylene at 1.262 ppm.

To characterize triglycerides in fat tissue there are models that use spectroscopy and the chemical characteristics as the number of double bonds (ndb), the number of double bonds interrupted by methylene ($nmidb$), and the average chain length (CL) of the FA (Hamilton et al., 2011) as well as models using chemical shift images (Peterson & Mansson, 2013; Berglund et al., 2012) with the aim to find the unsaturated, polysaturated, monosaturated and saturated FA. There have been studies of the composition of fat in vegetable oils and their main FA: saturated, oleic, linoleic and linolenic (Guillen & Ruiz, 2003b, 2003a; Miyake, Yokomizo, & Matsuzaki, 1998b; Knothe & Kenar, 2004) and others who consider a greater amount of FA present in lower proportions than 1

% (Yeung et al., 2008; van Werven et al., 2012; Willker & Leibfritz, 1998), but they cannot specify what is the percentage presence of each FA in the sample.

In this chapter we propose a new method to estimate the percentage presence of the seven principal fat peaks and the water peak per pixel. From the metabolic presence, it is possible to estimate the FA presence using the methodology discussed in chapter 3.

4.3. Materials and methods

We applied the optimization algorithm developed in chapter 3 to estimate the FA presence per pixel in a multi-echo image. The algorithm starts by estimating the metabolite contents, including water, and the magnetic field inhomogeneity. To test this method we used a digital phantom created in k-space with realistic values of FA from four oils and water. In the next sections we explain: the simulation of the data, the metabolite estimation, and finally, the FA estimation.

4.3.1. Phantom simulation

We simulated a phantom with five vials, one with water and the others four with edible oils: sunflower, corn, olive and soybean. The contents of FA in each oil were determined by GC and they are shown in Table 4.1. The percentages of FA do not sum 100 % because there are some FA that could not be classified by GC. Here we are not going to consider myristic and myristoleic FA because there is no information from GC.

TABLE 4.1. FA percentual presence in edible oils by GC. C: carbon chain length; ndb: number of double bounds.

FA	Symbol	C:ndb	Sunflower	Corn	Olive	Soybean
Myristic	Mi	C14:0	0.00	0.00	0.00	0.00
Myristoleic	Ml	C14:1	0.00	0.00	0.00	0.00
Palmitic	Pa	C16:0	6.30	11.30	15.60	11.60
Palmitoleic	Pl	C16:1	0.00	0.00	1.10	0.12
Stearic	Es	C18:0	2.90	2.30	1.60	4.30
Oleic	Ol	C18:1	29.80	36.10	65.50	21.20
Linoleic	Li	C18:2	59.40	47.60	14.80	56.50
Linolenic	Ln	C18:3	0.00	1.70	0.52	4.10
TOTAL			98.40	99.00	99.12	97.82

Since the hydrogen presence in each FA is known, we also know the contribution that each FA gives to the metabolites or spectrum peaks (see the protonic matrix A in Table 4.2). In our case there are eight metabolites.

TABLE 4.2. Protonic matrix A

Metabolite (ppm)	Mi	MI	Pa	PI	Es	Ol	Li	Ln	Water
5.272	0	2	0	2	0	2	4	6	0
4.680	0	0	0	0	0	0	0	0	2
2.722	0	0	0	0	0	0	2	4	0
2.260	2	2	2	2	2	2	2	2	0
1.976	0	4	0	4	0	4	4	4	0
1.534	2	2	2	2	2	2	2	2	0
1.262	20	12	24	16	28	20	14	8	0
0.875	3	3	3	3	3	3	3	3	0

We used the following notation:

- (i) \vec{x} is the relative content of FA (vector of size 8, including water).
- (ii) \vec{z} is the content of metabolites in arbitrary units (vector of size 8).
- (iii) A is the protonic matrix that links the FA with the metabolites through $\vec{z} = A\vec{x}$.

We will use eight echoes acquired at times \vec{t} (vector of size 8). The digital phantom m consisted in 5 circles (or vials, l). We added linear inhomogeneity to the field $f(x, y) = \alpha x + \beta y$. The inhomogeneity field map from m can be calculated using:

$$f(m) = \frac{\phi_2(m) - \phi_1(m)}{2\pi \cdot \Delta t} \quad (4.5)$$

where Δt is the difference between $TE_{n+1} - TE_n$, ϕ_n is the phase from the image acquired at TE_n . Each vial l was acquired at echo times t_j . The assigned signal intensity p for each metabolite b and for each vial correspond to data in Table 4.3 (the over-line indicates continues functions):

$$\bar{m}_l^j(x, y) = \sum_{b=1}^8 p_{b,l} \left[\prod \left(\frac{\sqrt{(x - x_c)^2 + (y - y_c)^2}}{r_l} \right) e^{-t_j/T2_b} e^{-i2\pi t_j \sigma_b \gamma B_0} e^{-i2\pi t_j f(x,y)} \right] \quad (4.6)$$

$$\begin{aligned}
t_j &= \begin{bmatrix} 2.3 & 4.6 & 6.9 & 9.2 & 11.5 & 13.8 & 16.1 & 18.4 \end{bmatrix} \text{ ms} \\
\sigma_b &= \begin{bmatrix} 5.272 & 4.680 & 2.722 & 2.260 & 1.976 & 1.534 & 1.262 & 0.875 \end{bmatrix} \text{ ppm} \\
T2_b &= \begin{bmatrix} 46.5 & 2000 & 48.4 & 47.2 & 36.3 & 37.6 & 82.6 & 79.4 \end{bmatrix} \text{ ms}
\end{aligned} \tag{4.7}$$

$$f(x, y) = 30x + (-30)y \text{ Hz}$$

where x_c and y_c correspond to the center of each vial circle and r is its ratio, $\sigma_b \gamma B_0$ is the chemical shift in Hertz, and T2 are extracted from Peterson et al.,2013 work (Peterson & Mansson, 2013) with

$$\bar{S}^j(x, y) = \sum_{l=1}^5 \bar{m}_l^j(x, y) \tag{4.8}$$

In k space the same expression for $\bar{M}_l^j(k_x, k_y)$ is:

$$\mathcal{F} \left\{ \sum_{b=1}^8 p_{b,l} \left[\Pi \left(\frac{\sqrt{(x - x_v)^2 + (y - y_v)^2}}{r_l} \right) e^{-i2\pi t_j(\alpha x + \beta y)} \right] \right\} e^{-i2\pi t_j \left(\frac{1}{2\pi T2_b + \sigma_b \gamma B_0} \right)} \tag{4.9}$$

The simulated raw data is

$$\bar{S}^j(k_x, k_y) = \sum_{l=1}^5 \bar{M}_l^j(k_x, k_y) e^{-i2\pi t_j \left(\frac{1}{2\pi T2_b} + \sigma_b \gamma B_0 \right)} \tag{4.10}$$

and each echo will be the DFT (Discrete Fourier Transform) of the samples $S^j(k_x, k_y)$ which we will call $s^j(x, y)$.

Table 4.3 shows the final \bar{z} value normalized for each oil and water sample. Figure 4.1 shows the simulated image phantom obtained applying the inverse Fast Fourier transform in 2D, and the field variation applied. For this specific case the variation field comes from -15 Hz to 15 Hz across the y axis, being zero in the center of the image. The circles in the image represent different oils and water samples. The left upper circle represents sunflower, the right upper circle represents corn, the central circle represents water, the left down circle represents olive and the final one represents soybean:

TABLE 4.3. Phantom metabolic presence for sunflower (G), corn (C), water (W), olive (O) and soybean (S) from GC

Metabolite (ppm)	G	C	W	O	S
5.272	9.521	8.739	0	6.263	9.349
4.680	0	0	100	0	0
2.722	3.806	3.268	0	1.015	4.145
2.260	6.304	6.343	0	6.351	6.267
1.976	11.430	10.943	0	10.497	10.497
1.534	6.304	6.343	0	6.351	6.267
1.262	53.178	55.664	0	62.729	52.810
0.875	9.457	9.514	0	9.526	9.401

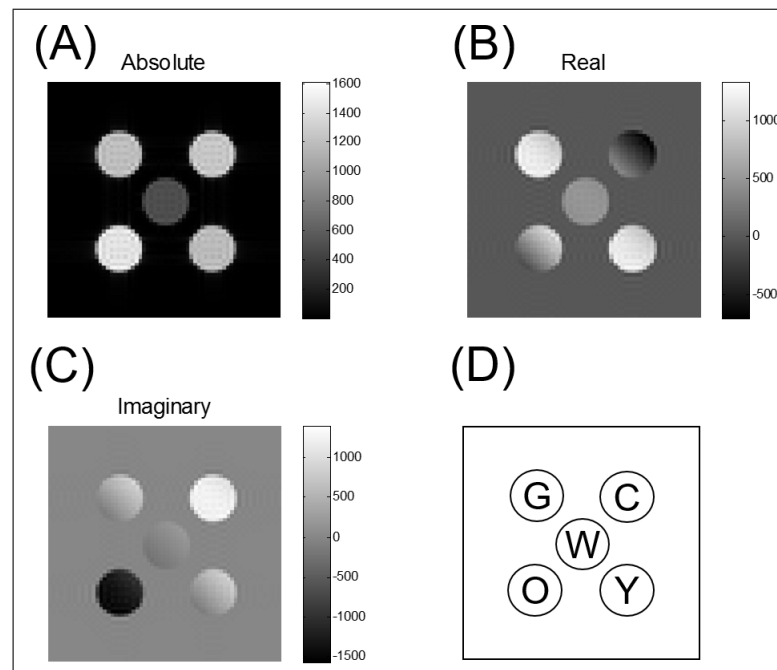


FIGURE 4.1. Simulated digital image phantom for a $TE = 18.4ms$ with magnetic field inhomogeneities $[30 -30]$ Hz. (A) Absolute value. (B) Real value. (C) Imaginary value. (D) Sample correspondence: G sunflower, C corn, W water, O olive, Y soybean

For this specific case the variation field is from -15 Hz to 15 Hz across the diagonal. In order to know how the inhomogeneities field added affect the results, we made some tests (Table 4.4) for different α and β values.

4.3.2. Metabolite estimation

To estimate the metabolite presence in each pixel we based on the formulation proposed by (Peterson & Mansson, 2013) (for simplicity of notation we dropped the arguments x and y)

TABLE 4.4. Different α and β values used

Test	α (Hz)	β (Hz)
1	0	0
2	5	-5
3	10	-10
4	15	-15
5	30	-30
6	60	-60

$$s(t) = \left(W e^{\eta_w t} + F \sum_{m=1}^M z_m e^{\eta_m t} \right) e^{\hat{\psi} t} \quad (4.11)$$

where $s(t)$ is the signal coming from the pixel at echo time t , W is the amount of water, $\eta_w = 1/T2_w$, F is the amount of fat, $\eta_m = 1/T2_m + i2\pi\sigma_m\gamma B_0$, and $\hat{\psi}$ is the magnetic field inhomogeneities: $\hat{\psi} = i2\pi\psi - R_2^*$ with $R_2^* = \frac{1}{T2^*}$ where z_m are the relative content of each metabolite.

To simplify notation we write the previous equation considering water as a metabolite (equation 4.12):

$$s(t) = \left(\sum_{m=1}^8 z_m E_m(t) \right) e^{\hat{\psi} t} \quad (4.12)$$

where $E_m(t) = e^{\eta_m t}$ and we want to solve equation 4.13 using a \vec{z} minimization showed in equation 4.14:

$$\vec{S} = \Psi(\hat{\psi}) E \hat{\vec{z}}. \quad (4.13)$$

$$\begin{aligned} \min_{\vec{z}} ||\Psi(\hat{\psi}) E \hat{\vec{z}} - \vec{S}||_2^2 \\ \text{s.t. } z_m \geq 0 \end{aligned} \quad (4.14)$$

Considering the eight echoes, the signal $s(t)$ can be represented as the vector $\vec{S}_{n \times 1}$, the intrinsic relaxation times matrix T2 as $E_{n \times 8}$, the magnetic field variation $\Psi(\hat{\psi})_{n \times n}$, and the metabolites $\hat{\vec{z}}_{8 \times 1}$:

$$\vec{S}_{n \times 1} = \begin{bmatrix} s_1 \\ \vdots \\ s_n \end{bmatrix} \quad (4.15)$$

$$\Psi(\hat{\psi})_{n \times n} = \begin{bmatrix} e^{\hat{\psi}t_1} & \dots & 0 \\ \vdots & \ddots & \vdots \\ 0 & \dots & e^{\hat{\psi}t_n} \end{bmatrix} \quad (4.16)$$

$$E_{n \times 8} = \begin{bmatrix} E_1(t_1) & E_2(t_1) & \dots & E_8(t_1) \\ \vdots & \vdots & \ddots & \vdots \\ E_1(t_n) & E_2(t_n) & \dots & E_8(t_n) \end{bmatrix} \quad (4.17)$$

$$\hat{\vec{z}}_{8 \times 1} = \begin{bmatrix} \hat{z}_1 \\ \vdots \\ \hat{z}_8 \end{bmatrix} \quad (4.18)$$

Due to the presence of magnetic field inhomogeneities we corrected the $\tilde{\psi}$ value using the iterative procedure proposed by Yu et al. (Yu et al., 2007):

- (i) We assigned an initial value for the complex magnetic field $\tilde{\psi} = \psi_0$. We used 0.
- (ii) With $\tilde{\psi}$ estimated, we computed the complex values for \hat{z}_m minimizing:

$$\begin{aligned} \min_{\hat{\vec{z}}} ||\Psi(\hat{\psi}) E \hat{\vec{z}} - \vec{S}||_2^2 \\ \text{s.t. } \hat{z}_m \geq 0 \end{aligned} \quad (4.19)$$

- (iii) We approximate equation 4.12 by Taylor expansion with only linear terms. We get equation 4.20:

$$\begin{aligned}
s_i = & \left(\sum_{m=1}^8 \hat{z}_m E_m(t_i) \right) e^{\hat{\psi} t_i} \Delta \psi + \\
& E_1(t_i) e^{\hat{\psi} t_i} \Delta z_1 + E_2(t_i) e^{\hat{\psi} t_i} \Delta z_2 + E_3(t_i) e^{\hat{\psi} t_i} \Delta z_3 + \\
& E_4(t_i) e^{\hat{\psi} t_i} \Delta z_4 + E_5(t_i) e^{\hat{\psi} t_i} \Delta z_5 + E_6(t_i) e^{\hat{\psi} t_i} \Delta z_6 + \\
& E_7(t_i) e^{\hat{\psi} t_i} \Delta z_7 + E_8(t_i) e^{\hat{\psi} t_i} \Delta z_8
\end{aligned} \tag{4.20}$$

It can be arranged as:

$$\vec{S} = \Psi(\hat{\psi}) E \hat{\vec{z}} + \Psi(\hat{\psi}) \begin{bmatrix} \sum_{m=1}^8 \hat{z}_m E_m(t_1) & E_1(t_1) & E_2(t_1) & \cdots & E_8(t_1) \\ \vdots & \vdots & \vdots & \ddots & \vdots \\ \sum_{m=1}^8 \hat{z}_m E_m(t_n) & E_1(t_n) & E_2(t_n) & \cdots & E_8(t_n) \end{bmatrix} \begin{bmatrix} \Delta \hat{\psi} \\ \Delta \hat{z}_1 \\ \vdots \\ \Delta \hat{z}_8 \end{bmatrix} \tag{4.21}$$

and the final signal (\vec{S}) can be written as:

$$\vec{S} = \Psi(\hat{\psi}) E \hat{\vec{z}} + \Psi(\hat{\psi}) B \Delta \hat{\vec{z}} \tag{4.22}$$

where

$$B = \begin{bmatrix} \sum_{m=1}^8 \hat{z}_m E_m(t_1) & E_1(t_1) & E_2(t_1) & \cdots & E_8(t_1) \\ \vdots & \vdots & \vdots & \ddots & \vdots \\ \sum_{m=1}^8 \hat{z}_m E_m(t_n) & E_1(t_n) & E_2(t_n) & \cdots & E_8(t_n) \end{bmatrix} \tag{4.23}$$

$$\Delta \hat{\vec{z}} = \begin{bmatrix} \Delta \hat{\psi} \\ \Delta \hat{z}_1 \\ \vdots \\ \Delta \hat{z}_8 \end{bmatrix} \tag{4.24}$$

Therefore, the error terms can be obtained by another least-squares inversion:

$$\Delta \hat{\vec{z}} = (B^T B)^{-1} B^T \left(\Psi(-\hat{\psi}) \vec{S} - E \hat{\vec{z}} \right) \tag{4.25}$$

or:

$$\begin{aligned} \min_{\Delta \hat{\vec{z}}} & \left\| (\Psi(\hat{\psi}) E \hat{\vec{z}} + \Psi(\hat{\psi}) B \Delta \hat{\vec{z}}) - \vec{S} \right\|_2^2 \\ \text{s.t. } & \Delta \hat{z}_m \geq 0 \end{aligned} \quad (4.26)$$

- (iv) Save the objective function from both least-squares minimization: o from $\hat{\vec{z}}$ and q from $\Delta \hat{\vec{z}}$. We also save $\Delta \hat{\vec{z}}$ and $\hat{\vec{z}}$.
- (v) We repeat the iterative process for each pixel from (ii) to (iv) until both of the following convergence criterion is achieved:

$$o < \epsilon \quad (4.27)$$

$$q < \epsilon \quad (4.28)$$

where ϵ is a small value. In this work $\epsilon = 0.1$ Hz.

If the last criterion is not achieved, a predefined maximum number of iterations (20) were used. In that case we find the minimum q , and we used its correspondent $\hat{\vec{z}}$ and $\Delta \hat{\vec{z}}$ values.

4.3.3. FA estimation

To estimate FA presence in each pixel we used the formulation of chapter 3. The upper and lower bounds are given in Table 4.5. Since the water sample has no FA it was not considered in the estimation. Two physical constraints were reached: upper bound for palmitic and palmitoleic FA for olive oil

4.4. Results

The field map correction using the first optimization is shown in Figure 4.2. We employed a mask to eliminate the data outside the vials. The initial field map was considered as zero. The eight estimated metabolites for the edible oils and water with their correspondent theoretical values are shown in Figure 4.3 (detail in Table 4.6) for test 5 (inhomogeneities field of [30 -30] Hz). The minimum error found was 0.026 % in 4.680 ppm metabolite for soybean oil. The maximum error found was 5.41 % for the methylene β carboxil in 1.534 ppm for the olive oil. Figure 4.4 shows the

TABLE 4.5. Constraints used for the FA estimation with one standard deviation. LB: lower bound. UB: upper bound

FA	LB	UB
Pa	2.49	19.41
Pl	0.00	1.64
Es	0.45	5.45
Ol	1.97	84.73
Li	0.00	79.88
Ln	0.00	5.93

metabolites image estimation results from the simulated digital phantom without and with phase correction.

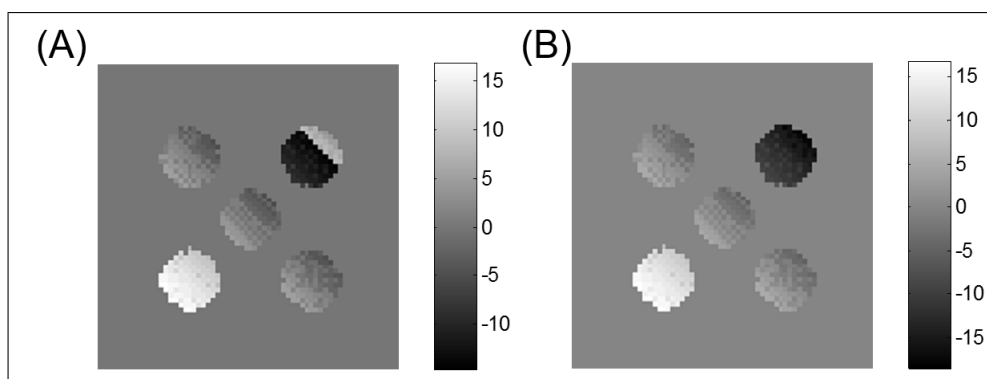


FIGURE 4.2. (A) Field inhomogeneity estimated from digital phantom created with an inhomogeneity field of [30 -30] Hz without phase correction, and (B) with phase correction

The estimated FA from the metabolites previously calculated from the edible oils with their original percentage GC value is shown in Figure 4.5 (detail in Table 4.7). There are no myristic and myristyoleic FA estimation because they are not present in the original GC (Table 4.1). The minimum error found was 0.38% for the palmitoleic FA for the olive oil. The maximum error found was 13.64 % for oleic FA for the olive oil. Figure 4.6 shows the results of the FA estimation in the simulated phantom from the metabolite data.

The metabolite and FA estimation from the tests 1, 5 and 6 (Table 4.4) are shown in Figure 4.7 and Figure 4.8, respectively. It shows the absolute error between the theoretical values (for metabolites and FA) and the estimated values.

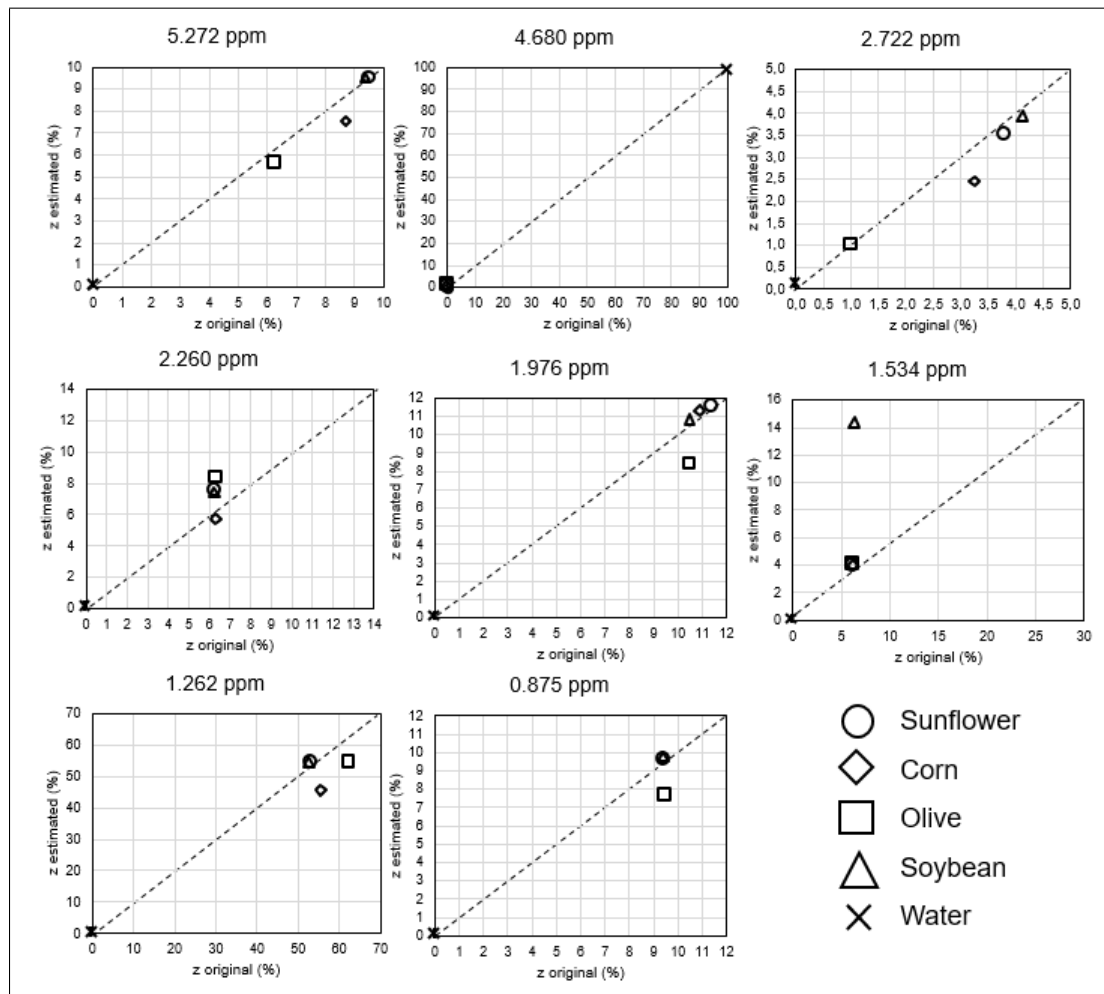


FIGURE 4.3. Comparison between the metabolic estimation and original values for each oil and water sample (test 5 with an inhomogeneity field of [30 -30] Hz).

4.5. Discussion

The proposed method achieves good estimations for the metabolites. The biggest errors are due to an inaccurate estimation of the field inhomogeneities. Without field inhomogeneities, the results have minimum errors (less than 2 %, Figure 4.7A). Our field map estimation (Figure 4.2) has wraparound when the inhomogeneities field is [30 -30] Hz. The same case can be seen when the field inhomogeneities is [60 -60] Hz (Figure 4.7). In these two cases there is a growing estimation error: around 12 % with 30 Hz field, and around 50 % with 60 Hz field in 0.875 ppm metabolite, for corn oil; and around 9 % with 30 and 60 Hz field, in 1.534 ppm metabolite, for olive oil. These two oils have wraparound problems which suggests there must be a correction after the field estimation, in order to have a better metabolite estimation, below 1.6 ppm. If the

TABLE 4.6. Metabolic percentage estimation (test 5 with an inhomogeneity field of [30 -30] Hz corrected). Est: estimated. Eabs: absolute error from the theoretical values

Metabolite (ppm)	Sunflower		Corn		Water		Olive		Soybean	
	Est.	Eabs	Est.	Eabs	Est.	Eabs	Est.	Eabs	Est.	Eabs
5.328	9.479	0.041	8.561	0.178	0.400	0.400	6.193	0.071	9.470	0.076
4.680	0.031	0.031	0.048	0.048	96.794	3.206	0.069	0.069	0.026	0.026
2.722	3.537	0.269	2.859	0.409	0.474	0.474	0.977	0.038	3.940	0.205
2.260	7.386	1.064	8.097	1.754	0.572	0.575	6.162	0.188	7.352	1.085
1.976	11.680	0.250	9.903	1.040	0.394	0.394	11.844	1.346	10.844	0.347
1.534	3.746	2.559	6.468	0.125	0.622	0.622	0.941	5.410	3.950	2.317
1.262	54.230	1.051	55.540	0.169	0.251	0.251	62.377	0.353	54.464	1.653
0.875	9.897	0.440	8.486	1.029	0.294	0.294	11.406	1.880	9.920	0.519

TABLE 4.7. FA percentage estimation from corrected phase. Est: estimated. Eabs: absolute error.

	Sunflower		Corn		Olive		Soybean	
	Est.	Eabs	Est.	Eabs	Est.	Eabs	Est.	Eabs
FA								
Pa	9.02	2.72	15.12	3.82	4.46	11.14	9.90	1.70
Pl	0.71	0.71	1.17	1.17	0.72	0.38	0.65	0.55
Es	0.75	2.15	2.47	0.17	4.35	2.75	4.07	0.23
Ol	34.43	4.63	30.92	5.18	79.14	13.64	27.08	5.88
Li	48.76	10.64	41.72	5.88	9.08	5.72	50.18	6.32
Ln	2.75	2.75	3.36	1.66	0.37	0.13	4.07	0.03

metabolite estimation have errors larger than 2 %, our FA estimation will have errors larger than 12 %. The FA estimation from the edible oils is possible using an optimization algorithm with known constraints for the minimum and maximum expected percentages. These constraints are important due to the existence of many local minimum. We defined them based on known information from GC. If there is no information to establish the boundaries, the optimization algorithm will not find the expected solution. The field inhomogeneities added to the phantom makes a harder metabolic estimation, and consequently, the FA estimation. With a homogeneous field the proposed algorithm can find a FA estimation with an error less than 13 % (Figure 4.8A).

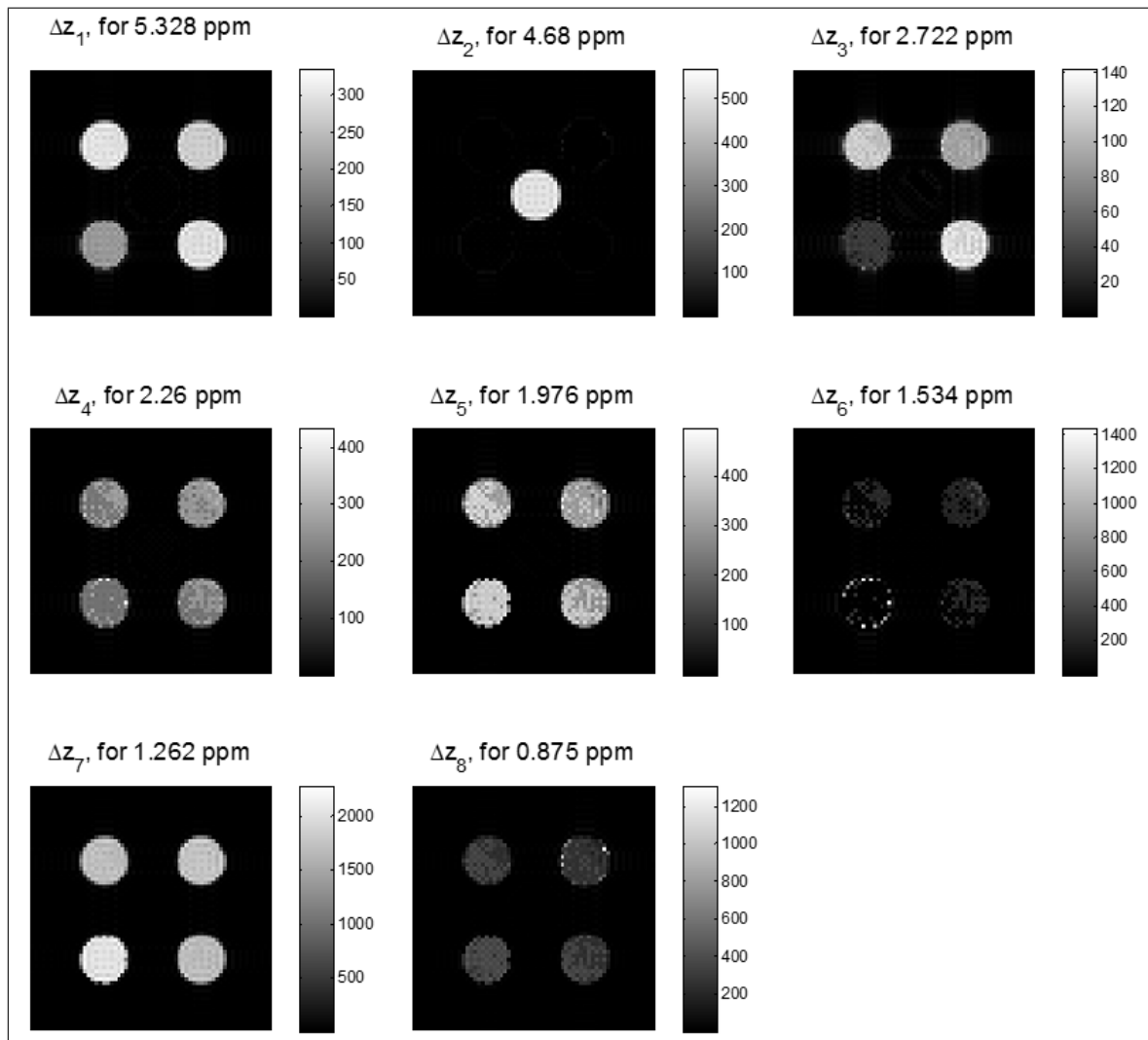


FIGURE 4.4. Metabolites estimation for each oil and water sample (test 5 with an inhomogeneity field of [30 -30] Hz corrected). The gray scale shows the percentage of presence.

4.6. Conclusion

The proposed optimization algorithm allows estimating the metabolite in a digital image phantom using GC as a priori information. The estimation error when there are no field inhomogeneities has excellent results (lower than 2 %) comparing with GC original data. This method can predict the metabolite presence as an MR image, which gives the spatial location of them, in a faster way than multiple voxels acquired with MRS. This is useful to estimate not only the presence of FA in liver, but to analyze different metabolites presence in brain, where some metabolite markers are used, to analyze for example: multiple sclerosis, epilepsy, among others ((Stagg & Rothman,

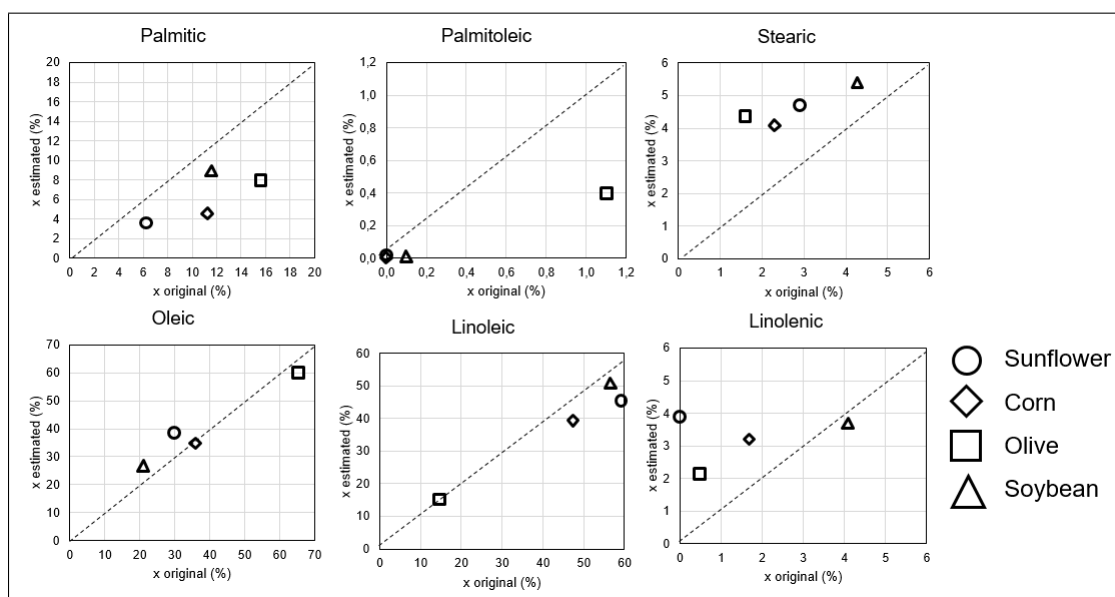


FIGURE 4.5. Comparison between FA estimation and original values for each oil (test 5 with an inhomogeneity field of [30 -30] Hz)

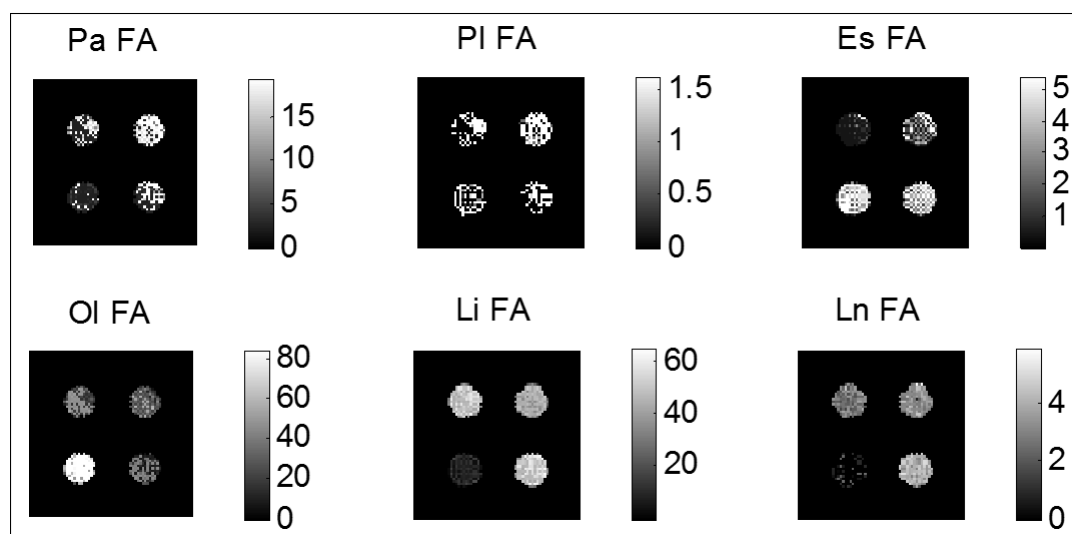


FIGURE 4.6. FA estimation from the simulated phantom for the edible oils corrected. The gray scale means the percentage presence.

2013)). From the metabolite information we can estimate the FA presence in each pixel. We postulate that this FA estimation method is important because it allows to study the time evolution and characteristics of the fat distribution. We demonstrated its feasibility using a simulated digital phantom with the FA composition from four edible oils and water.

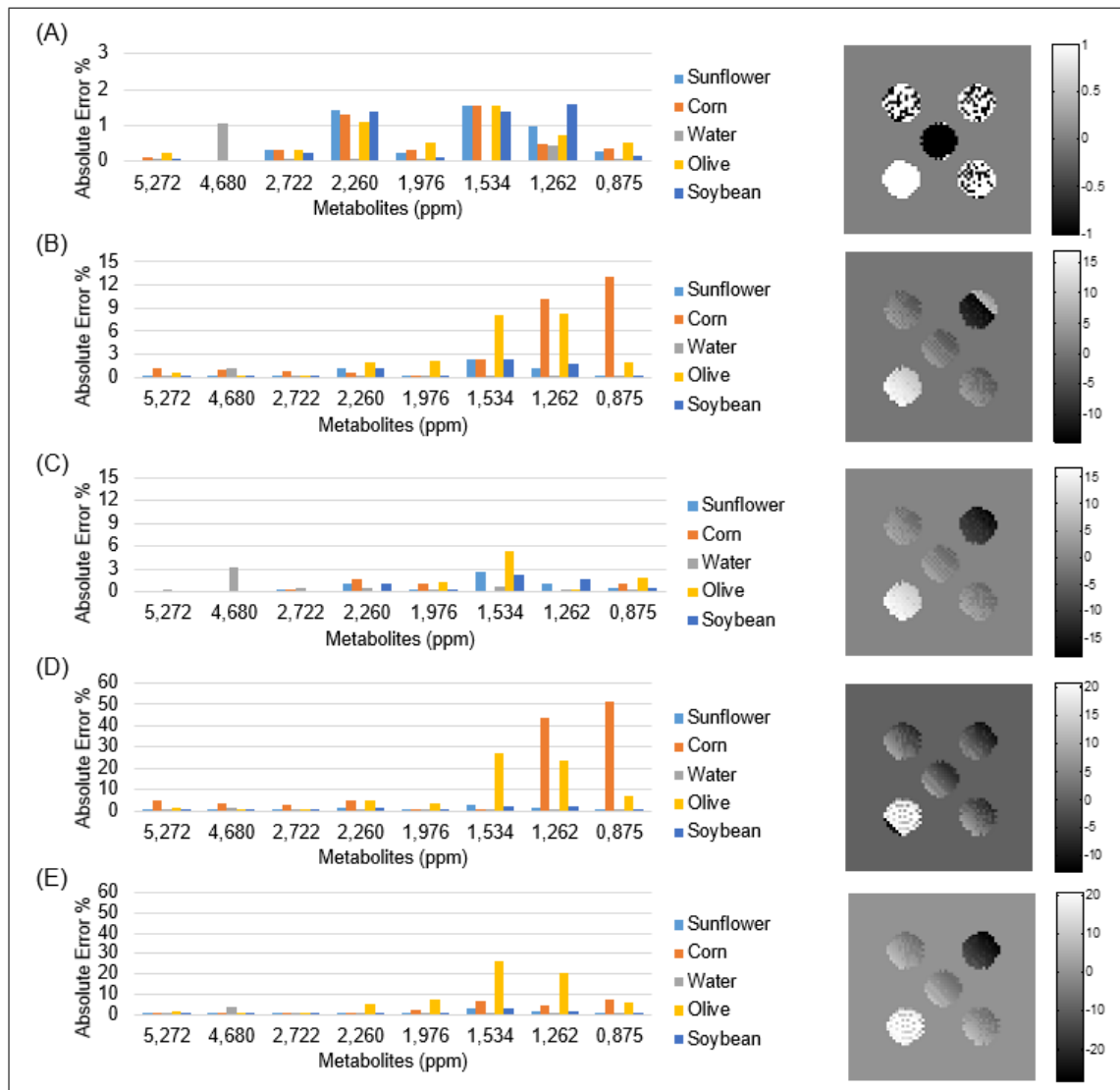


FIGURE 4.7. Absolute errors between original and estimated data for metabolites. In the right is the estimated field map correction of the simulated phantom which shows the inhomogeneity field added to vertical and horizontal axis. (A) [0 0] Hz. (B) [30 -30] Hz. (C) corrected [30 -30] Hz. (D) [60 -60] Hz. (E) corrected [60 -60] Hz.

4.7. Acknowledgements:

Funding grant: FONDECYT 1130379 and 1141201.

Daniel Aguirre was funded by a scholarship from the Superior Educational National Secretary in Science and Technology (SENESCYT) from the Government of Ecuador, and also by a scholarship from the National Commission for Scientific Technological Research CONICYT-PCHA/Doctorado Nacional/2015-21150021 from the Government of Chile.

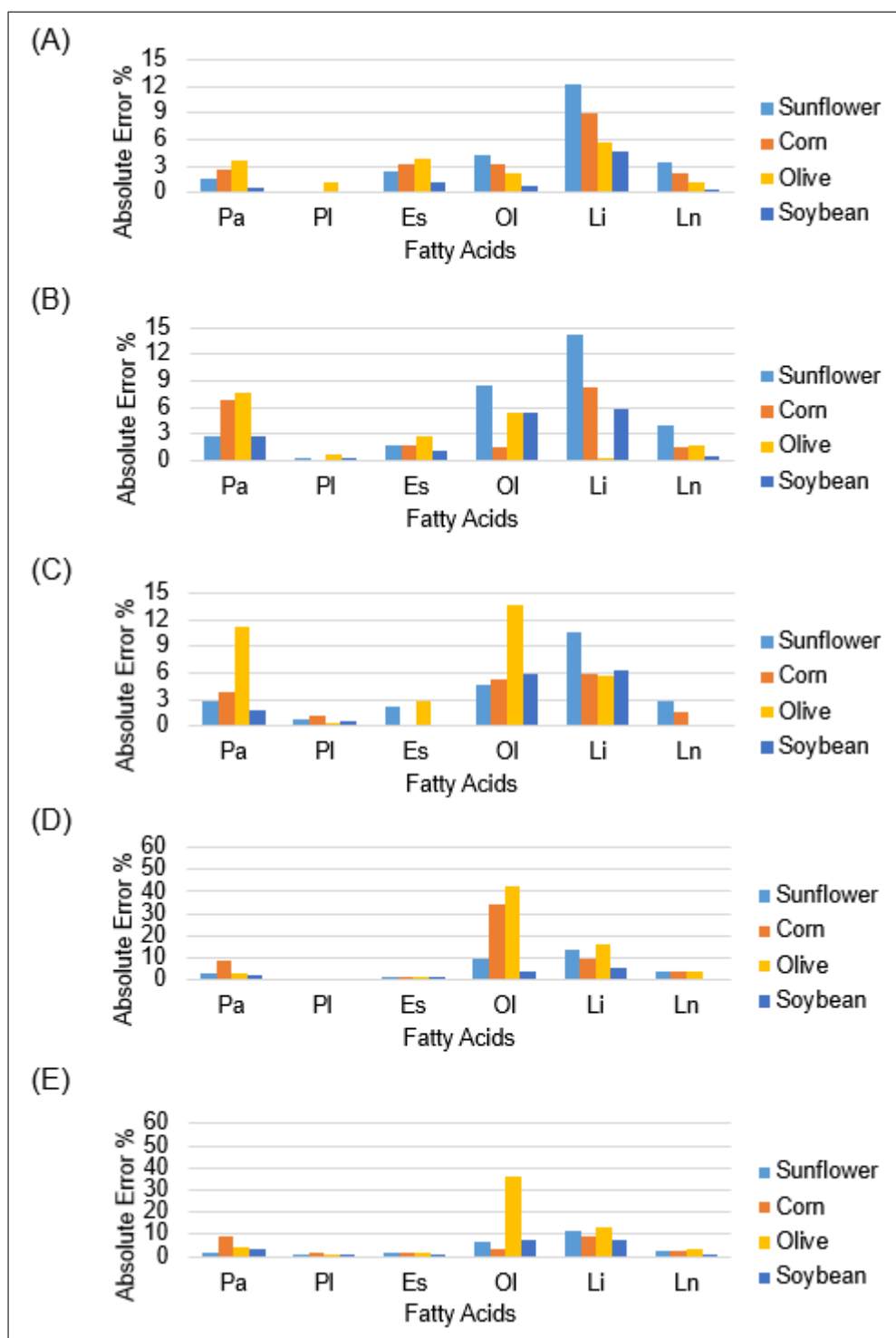


FIGURE 4.8. Absolute errors between original and estimated data for FA. (A) [0 0] Hz. (B) [30 -30] Hz. (C) corrected [30 -30] Hz. (D) [60 -60] Hz. (E) corrected [60 -60] Hz.

4.8. Future work:

Once we have successfully estimated the percentage presence of the FA in a digital image phantom with magnetic field inhomogeneities, the next step is adding noise to the simulated phantom. After that we can try with real images from the 1.5T and 3.0T MR equipment with some edible oils.

5. FINAL CONCLUSION

In this work we develop and validate an MRI technique to improve the early diagnosis of PH which would be useful to evaluate the hepatic steatosis, measuring in an indirect way how ill is the liver due to an resistance increase. This technique needs to be characterized, measuring precision, reproducibility and accuracy in a larger cohort. Beside that, is also necessary to work on reducing acquisition time.

We develop a new methodology to characterize the hepatic fat in a liver voxel using MRS, our next step is work on biological tissue to test this methodology. Also is necessary to measure precision, reproducibility and accuracy in a larger cohort, and compare it with its gold standard (GC). After that it could be used to evaluate the ill progression in time.

Finally, we develop a probe of concept technique to obtain metabolic quantitative images. These images can quantify and characterize the FA from a simulated digital phantom with edible oils and water information but, without field inhomogeneities. We need to solve the phase problem to have better results, and then measure the precision, reproducibility and accuracy comparing with other proposed algorithms.

References

- Abraldes, J. G., Tarantino, I., Turnes, J., Garcia-Pagan, J. C., Rodes, J., & Bosch, J. (2003, April). Hemodynamic response to pharmacological treatment of portal hypertension and long-term prognosis of cirrhosis. *Hepatology*, 37(4), 902–908. doi: 10.1053/jhep.2003.50133
- Adams, L. A., Angulo, P., & Lindor, K. D. (2005, March). Nonalcoholic fatty liver disease. *CMAJ*, 172(7), 899–905. doi: 10.1503/cmaj.045232
- Akhter, N. M., & Haskal, Z. J. (2012, December). Diagnosis and management of ectopic varices. *Gastrointestinal Intervention*, 1(1), 3–10. doi: 10.1016/j.gii.2012.08.001
- Almadi M. A., Almessabi A., Wong P., Ghali P., & Barkun A. (2011). Ectopic varices. *Gastrointestinal Endoscopy*, 74(2), 380–388.
- Andia, M. E., & Botnar, R. M. (2012, February). Arterial spin labeling angiography using a triple inversion recovery prepulse. *Magn Reson Med*, 67(2), 477–483. doi: 10.1002/mrm.23028
- Angulo, P., & Lindor, K. D. (2002, February). Non-alcoholic fatty liver disease. *J. Gastroenterol. Hepatol.*, 17 Suppl, S186–190.
- Annet, L., Materne, R., Danse, E., Jamart, J., Horsmans, Y., & Van Beers, B. E. (2003, November). Hepatic flow parameters measured with MR imaging and Doppler US: correlations with degree of cirrhosis and portal hypertension. *Radiology*, 229(2), 409–414. doi: 10.1148/radiol.2292021128
- Araya, J., Rodrigo, R., Videla, L., Thielemann, L., Orellana, M., Pettinelli, P., & Poniachik, J. (2004a, June). Increase in long-chain polyunsaturated fatty acid n - 6/n - 3 ratio in relation to hepatic steatosis in patients with non-alcoholic fatty liver disease. *Clin. Sci.*, 106(6), 635–643. doi: 10.1042/CS20030326

- Araya, J., Rodrigo, R., Videla, L. A., Thielemann, L., Orellana, M., Pettinelli, P., & Ponichik, J. (2004b, June). Increase in long-chain polyunsaturated fatty acid n - 6/n - 3 ratio in relation to hepatic steatosis in patients with non-alcoholic fatty liver disease. *Clin. Sci.*, *106*(6), 635–643. doi: 10.1042/CS20030326
- Armonis, A., Patch, D., & Burroughs, A. (1997, January). Hepatic venous pressure measurement: an old test as a new prognostic marker in cirrhosis? *Hepatology*, *25*(1), 245–248. doi: 10.1053/jhep.1997.v25.ajhep0250245
- Bahl, G., Cruite, I., Wolfson, T., Gamst, A. C., Collins, J. M., Chavez, A. D., . . . Sirlin, C. B. (2012, November). Noninvasive classification of hepatic fibrosis based on texture parameters from double contrast-enhanced magnetic resonance images. *J Magn Reson Imaging*, *36*(5), 1154–1161. doi: 10.1002/jmri.23759
- Bataller, R., & Brenner, D. A. (2005, February). Liver fibrosis. *J Clin Invest*, *115*(2), 209–218. doi: 10.1172/JCI200524282
- Berglund, J., Ahlström, H., & Kullberg, J. (2012, December). Model-based mapping of fat unsaturation and chain length by chemical shift imaging—phantom validation and in vivo feasibility. *Magn Reson Med*, *68*(6), 1815–1827. doi: 10.1002/mrm.24196
- Bernstein, M. A., King, K. F., & Zhou, X. J. (2004). *Handbook of MRI Pulse Sequences*. Elsevier.
- Berzigotti, A., Seijo, S., Reverter, E., & Bosch, J. (2013, February). Assessing portal hypertension in liver diseases. *Expert Rev Gastroenterol Hepatol*, *7*(2), 141–155. doi: 10.1586/egh.12.83
- Bosch, J., Abraldes, J. G., Berzigotti, A., & Garcia-Pagan, J. C. (2009, October). The clinical use of HVPG measurements in chronic liver disease. *Nat Rev Gastroenterol Hepatol*, *6*(10), 573–582. doi: 10.1038/nrgastro.2009.149
- Bosch, J., & Garcia-Pagan, J. C. (2000). Complications of cirrhosis. I. Portal hypertension. *Journal of Hepatology*, *32*, Supplement 1, 141–156. doi: 10.1016/S0168-8278(00)80422-5

- Bottomley, P. A. (1987). Spatial localization in NMR spectroscopy in vivo. *Ann. N. Y. Acad. Sci.*, 508, 333–348.
- Branch, M. A., Coleman, T. F., & Li, Y. (1999, August). A Subspace, Interior, and Conjugate Gradient Method for Large-Scale Bound-Constrained Minimization Problems. *SIAM J. Sci. Comput.*, 21(1), 1–23. doi: 10.1137/S1064827595289108
- Bray, G. A., Lovejoy, J. C., Smith, S. R., DeLany, J. P., Lefevre, M., Hwang, D., . . . York, D. A. (2002, September). The influence of different fats and fatty acids on obesity, insulin resistance and inflammation. *J. Nutr.*, 132(9), 2488–2491.
- Breuer, G., Evers, W. A. C., de Vree, J. H., Kleinegris, D. M. M., Martens, D. E., Wijffels, R. H., & Lamers, P. P. (2013). Analysis of fatty acid content and composition in microalgae. *J Vis Exp*(80). doi: 10.3791/50628
- Brown, M. A., & Semelka, R. C. (1999, December). MR imaging abbreviations, definitions, and descriptions: A review. *Radiology*, 213(3), 647–662.
- Brunt, E. M., Janney, C. G., Di Bisceglie, A. M., Neuschwander-Tetri, B. A., & Bacon, B. R. (1999, September). Nonalcoholic steatohepatitis: a proposal for grading and staging the histological lesions. *Am. J. Gastroenterol.*, 94(9), 2467–2474. doi: 10.1111/j.1572-0241.1999.01377.x
- Burkart, D. J., Johnson, C. D., Morton, M. J., Wolf, R. L., & Ehman, R. L. (1993, May). Volumetric flow rates in the portal venous system: measurement with cine phase-contrast MR imaging. *AJR Am J Roentgenol*, 160(5), 1113–1118. doi: 10.2214/ajr.160.5.8470589
- Bydder, M., Hamilton, G., Yokoo, T., & Sirlin, C. B. (2008, July). Optimal phased-array combination for spectroscopy. *Magnetic Resonance Imaging*, 26(6), 847–850. doi: 10.1016/j.mri.2008.01.050
- Bydder, M., Yokoo, T., Hamilton, G., Middleton, M. S., Chavez, A. D., Schwimmer, J. B., . . . Sirlin, C. B. (2008, April). Relaxation effects in the quantification of fat using gradient echo imaging. *Magn Reson Imaging*, 26(3), 347–359. doi: 10.1016/j.mri.2007.08.012

- Cao, Y., Wang, H., Johnson, T. D., Pan, C., Hussain, H., Balter, J. M., ... Feng, M. (2013, January). Prediction of liver function by using magnetic resonance-based portal venous perfusion imaging. *Int. J. Radiat. Oncol. Biol. Phys.*, 85(1), 258–263. doi: 10.1016/j.ijrobp.2012.02.037
- Cassidy, F. H., Yokoo, T., Aganovic, L., Hanna, R. F., Bydder, M., Middleton, M. S., ... Sirlin, C. B. (2009, February). Fatty liver disease: MR imaging techniques for the detection and quantification of liver steatosis. *Radiographics*, 29(1), 231–260. doi: 10.1148/rg.291075123
- Chalasani, N., Younossi, Z., Lavine, J. E., Diehl, A. M., Brunt, E. M., Cusi, K., ... Sanyal, A. J. (2012, June). The diagnosis and management of non-alcoholic fatty liver disease: practice Guideline by the American Association for the Study of Liver Diseases, American College of Gastroenterology, and the American Gastroenterological Association. *Hepatology*, 55(6), 2005–2023. doi: 10.1002/hep.25762
- Chelliah, S. T., Keshava, S. N., Moses, V., Surendrababu, N. R., Zachariah, U. G., & Eapen, C. (2011, October). Measurement of hepatic venous pressure gradient revisited: Catheter wedge vs balloon wedge techniques. *Indian J Radiol Imaging*, 21(4), 291–293. doi: 10.4103/0971-3026.90693
- Cheshkov, S., Dimitrov, I., Moreno, K., & Malloy, C. (2014). Fat Composition Determination via Combined ¹³C and ¹H MRS at Ultra High Field. In (Vol. 22, p. 0538). Milan.
- Cheung, J. S., Fan, S. J., Gao, D. S., Chow, A. M., Yang, J., Man, K., & Wu, E. X. (2011, March). In vivo lipid profiling using proton magnetic resonance spectroscopy in an experimental liver fibrosis model. *Acad Radiol*, 18(3), 377–383. doi: 10.1016/j.acra.2010.10.012
- Chisti, Y. (2007, June). Biodiesel from microalgae. *Biotechnol. Adv.*, 25(3), 294–306. doi: 10.1016/j.biotechadv.2007.02.001
- Clarke, S. D., Gasperikova, D., Nelson, C., Lapillonne, A., & Heird, W. C. (2002, June). Fatty acid regulation of gene expression: a genomic explanation for the benefits of the mediterranean diet. *Ann. N. Y. Acad. Sci.*, 967, 283–298.

- Cobbold, J. F. L., Patel, D., & Taylor-Robinson, S. D. (2012, August). Assessment of inflammation and fibrosis in non-alcoholic fatty liver disease by imaging-based techniques. *J. Gastroenterol. Hepatol.*, 27(8), 1281–1292. doi: 10.1111/j.1440-1746.2012.07127.x
- Cohen, J. C., Horton, J. D., & Hobbs, H. H. (2011, June). Human fatty liver disease: old questions and new insights. *Science*, 332(6037), 1519–1523. doi: 10.1126/science.1204265
- Coombs, B. D., Szumowski, J., & Coshov, W. (1997a). Two-point Dixon technique for water-fat signal decomposition with B0 inhomogeneity correction. *Magnetic Resonance in Medicine*, 38(6), 884–889. doi: 10.1002/mrm.1910380606
- Coombs, B. D., Szumowski, J., & Coshov, W. (1997b, December). Two-point Dixon technique for water-fat signal decomposition with B0 inhomogeneity correction. *Magn Reson Med*, 38(6), 884–889.
- Corbin, I. R., Furth, E. E., Pickup, S., Siegelman, E. S., & Delikatny, E. J. (2009, August). In vivo assessment of hepatic triglycerides in murine non-alcoholic fatty liver disease using magnetic resonance spectroscopy. *Biochim. Biophys. Acta*, 1791(8), 757–763. doi: 10.1016/j.bbali.2009.02.014
- Cowin, G. J., Jonsson, J. R., Bauer, J. D., Ash, S., Ali, A., Osland, E. J., ... Galloway, G. J. (2008, October). Magnetic resonance imaging and spectroscopy for monitoring liver steatosis. *J Magn Reson Imaging*, 28(4), 937–945. doi: 10.1002/jmri.21542
- Dais, P., & Hatzakis, E. (2013, February). Quality assessment and authentication of virgin olive oil by NMR spectroscopy: A critical review. *Analytica Chimica Acta*, 765, 1–27. doi: 10.1016/j.aca.2012.12.003
- De Graaf R. A. (2007). *In vivo NMR Spectroscopy Principles and Techniques* (2nd ed.). Connecticut: Wiley.
- de Graaf, R. A. (2007). Front Matter. In *In Vivo NMR Spectroscopy* (pp. i–xxi). John Wiley & Sons, Ltd.

- Delas, I., Popovic, M., Petrovic, T., Delas, F., & Ivankovic, D. (2008). Changes in the Fatty Acid Composition of Brain and Liver Phospholipids from Rats Fed Fat-Free Diet. *Food Technol. Biotechnol.*, 46(3), 278–285.
- Dixon, J. B., Bhathal, P. S., Hughes, N. R., & O'Brien, P. E. (2004, June). Nonalcoholic fatty liver disease: Improvement in liver histological analysis with weight loss. *Hepatology*, 39(6), 1647–1654. doi: 10.1002/hep.20251
- Dixon, W. T. (1984, October). Simple proton spectroscopic imaging. *Radiology*, 153(1), 189–194.
- Duarte, J. M. N., Lei, H., Mlynrik, V., & Gruetter, R. (2012, June). The neurochemical profile quantified by in vivo 1h NMR spectroscopy. *Neuroimage*, 61(2), 342–362. doi: 10.1016/j.neuroimage.2011.12.038
- Elsharkawy, W. B., & Elshemey, W. M. (2013, November). Quantitative characterization of fatty liver disease using x-ray scattering. *Radiation Physics and Chemistry*, 92, 14–21. doi: 10.1016/j.radphyschem.2013.07.010
- Ernst, T., & Hennig, J. (1991, September). Coupling effects in volume selective 1h spectroscopy of major brain metabolites. *Magn Reson Med*, 21(1), 82–96.
- Faria, S. C., Ganesan, K., Mwangi, I., Shieh morteza, M., Viamonte, B., Mazhar, S., . . . Sirlin, C. B. (2009, October). MR imaging of liver fibrosis: current state of the art. *Radiographics*, 29(6), 1615–1635. doi: 10.1148/rg.296095512
- Farrell, G. C., & Larter, C. Z. (2006, February). Nonalcoholic fatty liver disease: from steatosis to cirrhosis. *Hepatology*, 43(2 Suppl 1), S99–S112. doi: 10.1002/hep.20973
- Fazel, R., Krumholz, H. M., Wang, Y., Ross, J. S., Chen, J., Ting, H. H., . . . Nallamothu, B. K. (2009, August). Exposure to low-dose ionizing radiation from medical imaging procedures. *N. Engl. J. Med.*, 361(9), 849–857. doi: 10.1056/NEJMoa0901249
- Fischer, M. A., Raptis, D. A., Montani, M., Graf, R., Clavien, P.-A., Nanz, D., . . . Scheffel, H. (2012, October). Liver Fat Quantification by Dual-echo MR Imaging Outperforms

Traditional Histopathological Analysis. *Academic Radiology*, 19(10), 1208–1214. doi: 10.1016/j.acra.2012.05.009

Gach H. M., Li T., Lopez-Talavera J. C., & Kam A. W. (2002). Liver Perfusion MRI using Arterial Spin Labeling..

Glover, G. H. (1991, September). Multipoint dixon technique for water and fat proton and susceptibility imaging. *J. Magn. Reson. Imaging*, 1(5), 521–530. doi: 10.1002/jmri.1880010504

Graaf, R. A. d. (2007). *In Vivo NMR Spectroscopy: Principles and Techniques* (2nd ed.). Wiley-Interscience.

Guillen, M. D., & Ruiz, A. (2003a, September). 1h nuclear magnetic resonance as a fast tool for determining the composition of acyl chains in acylglycerol mixtures. *Eur. J. Lipid Sci. Technol.*, 105(9), 502–507. doi: 10.1002/ejlt.200300799

Guillen, M. D., & Ruiz, A. (2003b, November). Rapid simultaneous determination by proton NMR of unsaturation and composition of acyl groups in vegetable oils. *Eur. J. Lipid Sci. Technol.*, 105(11), 688–696. doi: 10.1002/ejlt.200300866

Guiu, B., Petit, J.-M., Loffroy, R., Ben Salem, D., Aho, S., Masson, D., ... Cercueil, J.-P. (2009, January). Quantification of liver fat content: comparison of triple-echo chemical shift gradient-echo imaging and in vivo proton MR spectroscopy. *Radiology*, 250(1), 95–102. doi: 10.1148/radiol.2493080217

Gujar, S. K., Maheshwari, S., Bjrkmann-Burtscher, I., & Sundgren, P. C. (2005, September). Magnetic resonance spectroscopy. *J Neuroophthalmol*, 25(3), 217–226.

Haacke, E. M., Brown, R. W., Thompson, M. R., & Venkatesan, R. (1999). *Magnetic Resonance Imaging: Physical Principles and Sequence Design*. Wiley.

Haacke RV., Mark E., Brown RM., & Thompson MR. (1999). *Magnetic Resonance Imaging Physical Principles and Sequence Design*. New York: John Wiley & Sons.

- Hamilton, G., Middleton, M. S., Bydder, M., Yokoo, T., Schwimmer, J. B., Kono, Y., ... Sirlin, C. B. (2009, July). Effect of PRESS and STEAM sequences on magnetic resonance spectroscopic liver fat quantification. *J Magn Reson Imaging*, 30(1), 145–152. doi: 10.1002/jmri.21809
- Hamilton, G., Yokoo, T., Bydder, M., Cruite, I., Schroeder, M. E., Sirlin, C. B., & Middleton, M. S. (2011, August). In vivo characterization of the liver fat H MR spectrum. *NMR Biomed*, 24(7), 784–790. doi: 10.1002/nbm.1622
- Hoad C., Costigan C., Marciani L., Kaye P., Spiller R., Gowland P., ... Francis S. (2011). Quantifying Blood Flow and Perfusion in Liver Tissue using Phase Contrast Angiography and Arterial Spin Labelling..
- Honorato, J. L., Parot, V., Tejos, C., Uribe, S., & Irarrazaval, P. (2011). Chemical species separation with simultaneous estimation of field map and T 2* using a k-space formulation. *Magnetic Resonance in Medicine*, 68(2), 400–408. doi: 10.1002/mrm.23237
- Horng, D. E., Hernando, D., Hines, C. D. G., & Reeder, S. B. (2013, February). Comparison of R2* correction methods for accurate fat quantification in fatty liver. *J Magn Reson Imaging*, 37(2), 414–422. doi: 10.1002/jmri.23835
- Johnson, N. A., Walton, D. W., Sachinwalla, T., Thompson, C. H., Smith, K., Ruell, P. A., ... George, J. (2008, May). Noninvasive assessment of hepatic lipid composition: Advancing understanding and management of fatty liver disorders. *Hepatology*, 47(5), 1513–1523. doi: 10.1002/hep.22220
- Kanematsu, M., Goshima, S., Watanabe, H., Kondo, H., Kawada, H., Noda, Y., & Moriyama, N. (2012). Diffusion/perfusion MR imaging of the liver: practice, challenges, and future. *Magn Reson Med Sci*, 11(3), 151–161.
- Kang, S. E., Lee, J. M., Klotz, E., Kim, K. W., Kim, J. H., Han, J. K., & Choi, B. I. (2011, October). Quantitative color mapping of the arterial enhancement fraction in patients with diffuse liver disease. *AJR Am J Roentgenol*, 197(4), 876–883. doi: 10.2214/AJR.10.5943

- Kapoor, D., & Sarin, S. (2002, December). Pathophysiology of portal hypertension. *Journal of Gastroenterology and Hepatology*, 17, S482–S487. doi: 10.1046/j.1440-1746.17.s4.14.x
- Karmarkar N. (1984). A new polynomial-time algorithm for linear programming. In (pp. 302–311). New York, NY, USA. doi: 10.1145/800057.808695
- Katada, Y., Shukuya, T., Kawashima, M., Nozaki, M., Imai, H., Natori, T., & Tamano, M. (2012, December). A comparative study between arterial spin labeling and CT perfusion methods on hepatic portal venous flow. *Jpn J Radiol*, 30(10), 863–869. doi: 10.1007/s11604-012-0127-y
- Keeler, J. (2010, May). Fourier transformation and data processing. In *Understanding NMR Spectroscopy* (Second ed., p. 526). Wiley.
- Kim, K. W., Lee, J. M., Klotz, E., Park, H. S., Lee, D. H., Kim, J. Y., ... Choi, B. I. (2009, February). Quantitative CT color mapping of the arterial enhancement fraction of the liver to detect hepatocellular carcinoma. *Radiology*, 250(2), 425–434. doi: 10.1148/radiol.2501072196
- Kleiner, D. E., & Brunt, E. M. (2012, February). Nonalcoholic fatty liver disease: pathologic patterns and biopsy evaluation in clinical research. *Semin. Liver Dis.*, 32(1), 3–13. doi: 10.1055/s-0032-1306421
- Knothe, G., & Kenar, J. A. (2004, February). Determination of the fatty acid profile by 1h-NMR spectroscopy. *Eur. J. Lipid Sci. Technol.*, 106(2), 88–96. doi: 10.1002/ejlt.200300880
- Kumar V., Abbas K., & Fausto N. (2005). *Robbins y Cotran: Patologa estructural y funcional*. (7a ed.). Espaa: Elsevier.
- Landgraf, B. R., Johnson, K. M., Roldan-Alzate, A., Francois, C. J., Wieben, O., & Reeder, S. B. (2014, April). Effect of temporal resolution on 4d flow MRI in the portal circulation. *J Magn Reson Imaging*, 39(4), 819–826. doi: 10.1002/jmri.24233

- Larque, E., Garcia-Ruiz, P.-A., Perez-Llamas, F., Zamora, S., & Gil, A. (2003, August). Dietary trans fatty acids alter the compositions of microsomes and mitochondria and the activities of microsome delta6-fatty acid desaturase and glucose-6-phosphatase in livers of pregnant rats. *J. Nutr.*, *133*(8), 2526–2531.
- Lee, N. K., Kim, S., Kim, G. H., Heo, J., Seo, H. I., Kim, T. U., & Kang, D. H. (2012, September). Significance of the "delayed hyperintense portal vein sign" in the hepatobiliary phase MRI obtained with Gd-EOB-DTPA. *J Magn Reson Imaging*, *36*(3), 678–685. doi: 10.1002/jmri.23700
- Lee, Y., Jee, H.-J., Noh, H., Kang, G.-H., Park, J., Cho, J., ... Kim, H. (2013, September). In vivo 1h-MRS hepatic lipid profiling in nonalcoholic fatty liver disease: An animal study at 9.4 T. *Magn. Reson. Med.*, *70*(3), 620–629. doi: 10.1002/mrm.24510
- Leito, H. S., Paulino, C., Rodrigues, D., Goncalves, S. I., Marques, C., Carneiro, M., ... Caseiro-Alves, F. (2013, August). MR fat fraction mapping: a simple biomarker for liver steatosis quantification in nonalcoholic fatty liver disease patients. *Acad Radiol*, *20*(8), 957–961. doi: 10.1016/j.acra.2013.05.004
- Liu, C.-Y., McKenzie, C. A., Yu, H., Brittain, J. H., & Reeder, S. B. (2007, August). Fat quantification with IDEAL gradient echo imaging: correction of bias from T(1) and noise. *Magn Reson Med*, *58*(2), 354–364. doi: 10.1002/mrm.21301
- Liu, P., Li, P., He, W., & Zhao, L.-Q. (2009, July). Liver and spleen volume variations in patients with hepatic fibrosis. *World J Gastroenterol*, *15*(26), 3298–3302. doi: 10.3748/wjg.15.3298
- Longo, R., Pollesello, P., Ricci, C., Masutti, F., Kvam, B. J., Bercich, L., ... de Bernard, B. (1995, June). Proton MR spectroscopy in quantitative in vivo determination of fat content in human liver steatosis. *J Magn Reson Imaging*, *5*(3), 281–285.
- Lu, W., Yu, H., Shimakawa, A., Alley, M., Reeder, S. B., & Hargreaves, B. A. (2008, July). Water-fat separation with bipolar multiecho sequences. *Magn Reson Med*, *60*(1), 198–209. doi: 10.1002/mrm.21583

- Lundbom, J., Hakkarainen, A., Fielding, B., Sderlund, S., Westerbacka, J., Taskinen, M.-R., & Lundbom, N. (2010, June). Characterizing human adipose tissue lipids by long echo time 1h-MRS in vivo at 1.5 Tesla: validation by gas chromatography. *NMR Biomed*, 23(5), 466–472. doi: 10.1002/nbm.1483
- Mann, L. W., Higgins, D. M., Peters, C. N., Cassidy, S., Hodson, K. K., Coombs, A., ... Hollingsworth, K. G. (2015, July). Accelerating MR Imaging Liver Steatosis Measurement Using Combined Compressed Sensing and Parallel Imaging: A Quantitative Evaluation. *Radiology*, 150320. doi: 10.1148/radiol.2015150320
- McPherson, S., Jonsson, J. R., Cowin, G. J., O'Rourke, P., Clouston, A. D., Volp, A., ... Powell, E. E. (2009, August). Magnetic resonance imaging and spectroscopy accurately estimate the severity of steatosis provided the stage of fibrosis is considered. *J. Hepatol.*, 51(2), 389–397. doi: 10.1016/j.jhep.2009.04.012
- Meisamy, S., Hines, C. D. G., Hamilton, G., Sirlin, C. B., McKenzie, C. A., Yu, H., ... Reeder, S. B. (2011a, March). Quantification of hepatic steatosis with T1-independent, T2-corrected MR imaging with spectral modeling of fat: blinded comparison with MR spectroscopy. *Radiology*, 258(3), 767–775. doi: 10.1148/radiol.10100708
- Meisamy, S., Hines, C. D. G., Hamilton, G., Sirlin, C. B., McKenzie, C. A., Yu, H., ... Reeder, S. B. (2011b, March). Quantification of hepatic steatosis with T1-independent, T2-corrected MR imaging with spectral modeling of fat: blinded comparison with MR spectroscopy. *Radiology*, 258(3), 767–775. doi: 10.1148/radiol.10100708
- Merkel, C., & Montagnese, S. (2011, October). Hepatic venous pressure gradient measurement in clinical hepatology. *Dig Liver Dis*, 43(10), 762–767. doi: 10.1016/j.dld.2011.03.002
- Miyake, Y., Yokomizo, K., & Matsuzaki, N. (1998a, September). Determination of unsaturated fatty acid composition by high-resolution nuclear magnetic resonance spectroscopy. *J Amer Oil Chem Soc*, 75(9), 1091–1094. doi: 10.1007/s11746-998-0118-4

- Miyake, Y., Yokomizo, K., & Matsuzaki, N. (1998b, January). Rapid determination of iodine value by ¹H nuclear magnetic resonance spectroscopy. *J Amer Oil Chem Soc*, 75(1), 15–19. doi: 10.1007/s11746-998-0003-1
- Motosugi, U., Hernando, D., Bannas, P., Holmes, J. H., Wang, K., Shimakawa, A., ... Reeder, S. B. (2015, November). Quantification of liver fat with respiratory-gated quantitative chemical shift encoded MRI. *J Magn Reson Imaging*, 42(5), 1241–1248. doi: 10.1002/jmri.24896
- Murata, Y., Abe, M., Hiasa, Y., Azemoto, N., Kumagi, T., Furukawa, S., ... Onji, M. (2008). Liver/spleen volume ratio as a predictor of prognosis in primary biliary cirrhosis. *J Gastroenterol.*, 43(8), 632–636. doi: 10.1007/s00535-008-2202-9
- Naressi, A., Couturier, C., Castang, I., de Beer, R., & Graveron-Demilly, D. (2001, July). Java-based graphical user interface for MRUI, a software package for quantitation of in vivo/medical magnetic resonance spectroscopy signals. *Comput. Biol. Med.*, 31(4), 269–286.
- Neuman, M. G., Cohen, L. B., & Nanau, R. M. (2014, December). Biomarkers in nonalcoholic fatty liver disease. *Can. J. Gastroenterol. Hepatol.*, 28(11), 607–618. (WOS:000346646900010)
- Noureddin, M., Lam, J., Peterson, M. R., Middleton, M., Hamilton, G., Le, T.-A., ... Loomba, R. (2013, December). Utility of magnetic resonance imaging versus histology for quantifying changes in liver fat in nonalcoholic fatty liver disease trials. *Hepatology*, 58(6), 1930–1940. doi: 10.1002/hep.26455
- Oostendorp, M., Engelke, U. F. H., Willemsen, M. A. A. P., & Wevers, R. A. (2006, July). Diagnosing inborn errors of lipid metabolism with proton nuclear magnetic resonance spectroscopy. *Clin. Chem.*, 52(7), 1395–1405. doi: 10.1373/clinchem.2006.069112
- Otsu N. (1979, January). A Threshold Selection Method from Gray-Level Histograms. *IEEE Transactions on Systems, Man and Cybernetics*, 9(1), 62–66. doi: 10.1109/TSMC.1979.4310076

- Ou, H.-Y., Bonekamp, S., Bonekamp, D., Corona-Villalobos, C. P., Torbenson, M. S., Geiger, B., & Kamel, I. R. (2013, October). MRI arterial enhancement fraction in hepatic fibrosis and cirrhosis. *AJR Am J Roentgenol*, *201*(4), W596–602. doi: 10.2214/AJR.12.10048
- Ouwerkerk, R., Pettigrew, R. I., & Gharib, A. M. (2012, November). Liver Metabolite Concentrations Measured with H-1 MR Spectroscopy. *Radiology*, *265*(2), 565–575. doi: 10.1148/radiol.12112344
- Paradis, V., Zalinski, S., Chelbi, E., Guedj, N., Degos, F., Vilgrain, V., ... Belghiti, J. (2009, March). Hepatocellular carcinomas in patients with metabolic syndrome often develop without significant liver fibrosis: a pathological analysis. *Hepatology*, *49*(3), 851–859. doi: 10.1002/hep.22734
- Peeters, F., Annet, L., Hermoye, L., & Van Beers, B. E. (2004, April). Inflow correction of hepatic perfusion measurements using T1-weighted, fast gradient-echo, contrast-enhanced MRI. *Magn Reson Med*, *51*(4), 710–717. doi: 10.1002/mrm.20032
- Peterson, P., & Mansson, S. (2013, March). Simultaneous quantification of fat content and fatty acid composition using MR imaging. *Magn Reson Med*, *69*(3), 688–697. doi: 10.1002/mrm.24297
- Pfleiderer, B., Campbell, T., Hulka, C. A., Kopans, D. B., Lean, C. L., Ackerman, J. L., ... Garrido, L. (1996, December). Silicone gel-filled breast implants in women: findings at H-1 MR spectroscopy. *Radiology*, *201*(3), 777–783.
- Pineda, N., Sharma, P., Xu, Q., Hu, X., Vos, M., & Martin, D. R. (2009, August). Measurement of hepatic lipid: high-speed T2-corrected multiecho acquisition at 1h MR spectroscopy—a rapid and accurate technique. *Radiology*, *252*(2), 568–576. doi: 10.1148/radiol.2523082084
- Pollesello, P., Masutti, F., Croc, L. S., Toffanin, R., Eriksson, O., Paoletti, S., ... Tiribelli, C. (1993, May). 1h NMR spectroscopic studies of lipid extracts from human fatty liver. *Biochem. Biophys. Res. Commun.*, *192*(3), 1217–1222. doi: 10.1006/bbrc.1993.1546

Popovic, T., Ranic, M., Bulajic, P., Milicevic, M., Arsic, A., Vucic, V., & Glibetic, M. (2009, November). Effects of n-3 Fatty Acids Supplementation on Plasma Phospholipids Fatty Acid Composition in Patients with Obstructive Jaundice- a Pilot Study. *J Clin Biochem Nutr*, 45(3), 370–375. doi: 10.3164/jcbtn.09-54

Pouillet, J.-B., Sima, D. M., & Van Huffel, S. (2008, December). MRS signal quantitation: a review of time- and frequency-domain methods. *J. Magn. Reson.*, 195(2), 134–144. doi: 10.1016/j.jmr.2008.09.005

Provencher, S. W. (1993, December). Estimation of metabolite concentrations from localized in vivo proton NMR spectra. *Magn Reson Med*, 30(6), 672–679.

Puri, P., Baillie, R. A., Wiest, M. M., Mirshahi, F., Choudhury, J., Cheung, O., ... Sanyal, A. J. (2007, October). A lipidomic analysis of nonalcoholic fatty liver disease. *Hepatology*, 46(4), 1081–1090. doi: 10.1002/hep.21763

Qayyum, A. (2009, October). MR spectroscopy of the liver: principles and clinical applications. *Radiographics*, 29(6), 1653–1664. doi: 10.1148/rg.296095520

Ramamonjisoa, N., Ratiney, H., Mutel, E., Guillou, H., Mithieux, G., Pilleul, F., ... Cavasila, S. (2013, July). In vivo hepatic lipid quantification using MRS at 7 Tesla in a mouse model of glycogen storage disease type 1a. *J. Lipid Res.*, 54(7), 2010–2022. doi: 10.1194/jlr.D033399

Ratzliff, V., Charlotte, F., Heurtier, A., Gombert, S., Giral, P., Bruckert, E., ... LIDO Study Group (2005, June). Sampling variability of liver biopsy in nonalcoholic fatty liver disease. *Gastroenterology*, 128(7), 1898–1906.

Reeder, S. B., Cruite, I., Hamilton, G., & Sirlin, C. B. (2011a). Quantitative Assessment of Liver Fat with Magnetic Resonance Imaging and Spectroscopy. *J. Magn. Reson. Imaging*, 34(4), 729 – 749. doi: 10.1002/jmri.22580

Reeder, S. B., Cruite, I., Hamilton, G., & Sirlin, C. B. (2011b, October). Quantitative Assessment of Liver Fat with Magnetic Resonance Imaging and Spectroscopy. *J Magn Reson Imaging*, 34(4), spcone. doi: 10.1002/jmri.22775

- Reeder, S. B., Hu, H. H., & Sirlin, C. B. (2012, November). Proton density fat-fraction: A standardized mr-based biomarker of tissue fat concentration. *J. Magn. Reson. Imaging*, 36(5), 1011–1014. doi: 10.1002/jmri.23741
- Reeder, S. B., Pineda, A. R., Wen, Z., Shimakawa, A., Yu, H., Brittain, J. H., ... Pelc, N. J. (2005a). Iterative decomposition of water and fat with echo asymmetry and least-squares estimation (IDEAL): Application with fast spin-echo imaging. *Magnetic Resonance in Medicine*, 54(3), 636–644. doi: 10.1002/mrm.20624
- Reeder, S. B., Pineda, A. R., Wen, Z., Shimakawa, A., Yu, H., Brittain, J. H., ... Pelc, N. J. (2005b, September). Iterative decomposition of water and fat with echo asymmetry and least-squares estimation (IDEAL): application with fast spin-echo imaging. *Magn Reson Med*, 54(3), 636–644. doi: 10.1002/mrm.20624
- Reeder, S. B., Wen, Z., Yu, H., Pineda, A. R., Gold, G. E., Markl, M., & Pelc, N. J. (2004, January). Multicoil Dixon chemical species separation with an iterative least-squares estimation method. *Magn Reson Med*, 51(1), 35–45. doi: 10.1002/mrm.10675
- Reeder S. B., Hines C. D., Yu H., McKenzie C. A., & Brittain J. H. (2009). On The Definition of Fat-Fraction for In Vivo Fat Quantification with Magnetic Resonance Imaging. 17.
- Ren, J., Dimitrov, I., Sherry, A. D., & Malloy, C. R. (2008, September). Composition of adipose tissue and marrow fat in humans by 1h NMR at 7 Tesla. *J Lipid Res*, 49(9), 2055–2062. doi: 10.1194/jlr.D800010-JLR200
- Roldan-Alzate, A., Frydrychowicz, A., Niespodzany, E., Landgraf, B. R., Johnson, K. M., Wieben, O., & Reeder, S. B. (2013, May). In vivo validation of 4d flow MRI for assessing the hemodynamics of portal hypertension. *J Magn Reson Imaging*, 37(5), 1100–1108. doi: 10.1002/jmri.23906
- Sass, D. A., Chang, P., & Chopra, K. B. (2005, January). Nonalcoholic fatty liver disease: a clinical review. *Dig. Dis. Sci.*, 50(1), 171–180.
- Schwenzer, N. F., Springer, F., Schraml, C., Stefan, N., Machann, J., & Schick, F. (2009, September). Non-invasive assessment and quantification of liver steatosis by ultrasound,

computed tomography and magnetic resonance. *J. Hepatol.*, 51(3), 433–445. doi: 10.1016/j.jhep.2009.05.023

Shiao, T.-Y., & Shiao, M.-S. (1989). Determination of fatty acid compositions of triacylglycerols by high resolution NMR spectroscopy. *Bot. Bull. Academia Sinica*, 30, 191–199.

Sijens, P. E. (2009, November). Parametric exploration of the liver by magnetic resonance methods. *Eur. Radiol.*, 19(11), 2594–2607. doi: 10.1007/s00330-009-1470-y

Skoch, A., Jr, F., Dezortov, M., Krusinov, E., Kratochvlov, S., Peliknov, T., ... Hjek, M. (2006, May). Intramyocellular lipid quantification from 1h long echo time spectra at 1.5 and 3 T by means of the LCModel technique. *J Magn Reson Imaging*, 23(5), 728–735. doi: 10.1002/jmri.20574

Smith, T. P., Kim, C. Y., Smith, A. D., Janas, G., Miller, M. J., Sopko, D. R., & Suhocki, P. V. (2012, February). Hepatic Venous Pressure Measurements: Comparison of End-Hole and Balloon Catheter Methods. *Journal of Vascular and Interventional Radiology*, 23(2), 219–226.e6. doi: 10.1016/j.jvir.2011.09.025

Smits, L. P., Coolen, B. F., Panno, M. D., Runge, J. H., Nijhof, W. H., Verheij, J., ... Stroes, E. S. (2015, September). Noninvasive Differentiation between Hepatic Steatosis and Steatohepatitis with MR Imaging Enhanced with USPIOs in Patients with Nonalcoholic Fatty Liver Disease: A Proof-of-Concept Study. *Radiology*, 150952. doi: 10.1148/radiol.2015150952

Stagg, C., & Rothman, D. (2013). *Magnetic Resonance Spectroscopy: Tools for Neuroscience Research and Emerging Clinical Applications* (1edition ed.). Amsterdam: Academic Press.

Stankovic, Z., Jung, B., Collins, J., Russe, M. F., Carr, J., Euringer, W., ... Markl, M. (2014, August). Reproducibility study of four-dimensional flow MRI of arterial and portal venous liver hemodynamics: influence of spatio-temporal resolution. *Magn Reson Med*, 72(2), 477–484. doi: 10.1002/mrm.24939

Stefan, D., Cesare, F. D., Andrasescu, A., Popa, E., Lazariev, A., Vescovo, E., ... Graveron-Demilly, D. (2009, October). Quantitation of magnetic resonance spectroscopy signals: the

- jMRUI software package. *Measurement Science and Technology*, 20(10), 104035. doi: 10.1088/0957-0233/20/10/104035
- Strobel, K., van den Hoff, J., & Pietzsch, J. (2008, February). Localized proton magnetic resonance spectroscopy of lipids in adipose tissue at high spatial resolution in mice in vivo. *J. Lipid Res.*, 49(2), 473–480. doi: 10.1194/jlr.D700024-JLR200
- Szczepaniak, L. S., Nurenberg, P., Leonard, D., Browning, J. D., Reingold, J. S., Grundy, S., ... Dobbins, R. L. (2005, February). Magnetic resonance spectroscopy to measure hepatic triglyceride content: prevalence of hepatic steatosis in the general population. *Am. J. Physiol. Endocrinol. Metab.*, 288(2), E462–468. doi: 10.1152/ajpendo.00064.2004
- Tang, A., Tan, J., Sun, M., Hamilton, G., Bydder, M., Wolfson, T., ... Sirlin, C. B. (2013, May). Nonalcoholic fatty liver disease: MR imaging of liver proton density fat fraction to assess hepatic steatosis. *Radiology*, 267(2), 422–431. doi: 10.1148/radiol.12120896
- Taouli, B., Ehman, R. L., & Reeder, S. B. (2009a, July). Advanced MRI methods for assessment of chronic liver disease. *AJR Am J Roentgenol*, 193(1), 14–27. doi: 10.2214/AJR.09.2601
- Taouli, B., Ehman, R. L., & Reeder, S. B. (2009b, July). Advanced MRI Methods for Assessment of Chronic Liver Disease. *Am. J. Roentgenol.*, 193(1), 14–27. doi: 10.2214/AJR.09.2601
- Taylor, C. R., & McCauley, T. R. (1992, April). Magnetic resonance imaging in the evaluation of the portal venous system. *J. Clin. Gastroenterol.*, 14(3), 268–273.
- Thabut, D., Moreau, R., & Lebrech, D. (2011, February). Noninvasive assessment of portal hypertension in patients with cirrhosis. *Hepatology*, 53(2), 683–694. doi: 10.1002/hep.24129
- Thomsen, C., Becker, U., Winkler, K., Christoffersen, P., Jensen, M., & Henriksen, O. (1994). Quantification of liver fat using magnetic resonance spectroscopy. *Magn Reson Imaging*, 12(3), 487–495.

- Tilg, H., & Moschen, A. R. (2010, November). Evolution of inflammation in nonalcoholic fatty liver disease: the multiple parallel hits hypothesis. *Hepatology*, 52(5), 1836–1846. doi: 10.1002/hep.24001
- Valls, C., Iannaccone, R., Alba, E., Murakami, T., Hori, M., Passariello, R., & Vilgrain, V. (2006, October). Fat in the liver: diagnosis and characterization. *Eur Radiol*, 16(10), 2292–2308. doi: 10.1007/s00330-006-0146-0
- Vanhamme, van den Boogaart A, & S, V. H. (1997, November). Improved method for accurate and efficient quantification of MRS data with use of prior knowledge. *J. Magn. Reson.*, 129(1), 35–43.
- Vanhamme, L., van den Boogaart A, A., & Van Huffel S, S. (1997, November). Improved method for accurate and efficient quantification of MRS data with use of prior knowledge. *J. Magn. Reson.*, 129(1), 35–43.
- van Werven, J. R., Marsman, H. A., Nederveen, A. J., ten Kate, F. J., van Gulik, T. M., & Stoker, J. (2012, January). Hepatic lipid composition analysis using 3.0-T MR spectroscopy in a steatotic rat model. *Magn Reson Imaging*, 30(1), 112–121. doi: 10.1016/j.mri.2011.07.028
- van Werven, J. R., Schreuder, T. C. M. A., Nederveen, A. J., Lavini, C., Jansen, P. L. M., & Stoker, J. (2010, August). Hepatic unsaturated fatty acids in patients with non-alcoholic fatty liver disease assessed by 3.0t MR spectroscopy. *Eur J Radiol*, 75(2), e102–107. doi: 10.1016/j.ejrad.2009.12.033
- Vermeulen, M. A. R., Ligthart-Melis, G. C., Buijsman, R., Siroen, M. P. C., van de Poll, M. C. G., Boelens, P. G., ... van Leeuwen, P. A. M. (2012, September). Accurate perioperative flow measurement of the portal vein and hepatic and renal artery: a role for preoperative MRI? *Eur J Radiol*, 81(9), 2042–2048. doi: 10.1016/j.ejrad.2011.06.023
- Vinaixa, M., Rodriguez, M. A., Rull, A., Beltran, R., Blade, C., Brezmes, J., ... Cor-reig, X. (2010, May). Metabolomic assessment of the effect of dietary cholesterol in the

progressive development of fatty liver disease. *J. Proteome Res.*, 9(5), 2527–2538. doi: 10.1021/pr901203w

Vlahov, G. (1999a). Application of NMR to the study of olive oils. *Progress in Nuclear Magnetic Resonance Spectroscopy*, 35, 341–357.

Vlahov, G. (1999b, December). Application of NMR to the study of olive oils. *Progress in Nuclear Magnetic Resonance Spectroscopy*, 35(4), 341–357. doi: 10.1016/S0079-6565(99)00015-1

Wang, X., Cao, Y., Fu, Y., Guo, G., & Zhang, X. (2011). Liver fatty acid composition in mice with or without nonalcoholic fatty liver disease. *Lipids Health Dis*, 10, 234. doi: 10.1186/1476-511X-10-234

Wang, X., Hernando, D., & Reeder, S. B. (2015, April). Sensitivity of chemical shift-encoded fat quantification to calibration of fat MR spectrum. *Magn Reson Med*. doi: 10.1002/mrm.25681

Willker, W., & Leibfritz, D. (1998, June). Assignment of mono- and polyunsaturated fatty acids in lipids of tissues and body fluids. *Magn. Reson. Chem.*, 36(S1), S79–S84. doi: 10.1002/(SICI)1097-458X(199806)36:133.0.CO;2-Z

Xiao, L., & Wu, E. X. (2011, October). Diffusion-weighted magnetic resonance spectroscopy: a novel approach to investigate intramyocellular lipids. *Magn Reson Med*, 66(4), 937–944. doi: 10.1002/mrm.23121

Yeung, D. K. W., Lam, S. L., Griffith, J. F., Chan, A. B. W., Chen, Z., Tsang, P. H., & Leung, P. C. (2008, February). Analysis of bone marrow fatty acid composition using high-resolution proton NMR spectroscopy. *Chem. Phys. Lipids*, 151(2), 103–109. doi: 10.1016/j.chemphyslip.2007.10.006

Yokoo, T., Shieh-morteza, M., Hamilton, G., Wolfson, T., Schroeder, M. E., Middleton, M. S., ... Sirlin, C. B. (2011, March). Estimation of Hepatic Proton-Density Fat Fraction by Using MR Imaging at 3.0 T. *Radiology*, 258(3), 749–759. doi: 10.1148/radiol.10100659

- Yu, H., McKenzie, C. A., Shimakawa, A., Vu, A. T., Brau, A. C. S., Beatty, P. J., ... Reeder, S. B. (2007, October). Multiecho reconstruction for simultaneous water-fat decomposition and $T2^*$ estimation. *J Magn Reson Imaging*, 26(4), 1153–1161. doi: 10.1002/jmri.21090
- Yu, H., Shimakawa, A., McKenzie, C. A., Brodsky, E., Brittain, J. H., & Reeder, S. B. (2008, November). Multiecho water-fat separation and simultaneous $R2^*$ estimation with multifrequency fat spectrum modeling. *Magn Reson Med*, 60(5), 1122–1134. doi: 10.1002/mrm.21737
- Yzet, T., Bouzerar, R., Allart, J.-D., Demuynck, F., Legallais, C., Robert, B., ... Baledent, O. (2010, March). Hepatic vascular flow measurements by phase contrast MRI and doppler echography: a comparative and reproducibility study. *J Magn Reson Imaging*, 31(3), 579–588. doi: 10.1002/jmri.22079
- Yzet, T., Bouzerar, R., Baledent, O., Renard, C., Lumbala, D. M., Nguyen-Khac, E., ... Meyer, M.-E. (2010, January). Dynamic measurements of total hepatic blood flow with Phase Contrast MRI. *European Journal of Radiology*, 73(1), 119–124. doi: 10.1016/j.ejrad.2008.09.032
- Zand, K. A., Shah, A., Heba, E., Wolfson, T., Hamilton, G., Lam, J., ... Sirlin, C. B. (2015, November). Accuracy of multiecho magnitude-based MRI (M-MRI) for estimation of hepatic proton density fat fraction (PDFF) in children. *J Magn Reson Imaging*, 42(5), 1223–1232. doi: 10.1002/jmri.24888